Study of the interaction between the solar wind and the Earth magnetosphere: Theoretical model and application on the data of the Halloween event of October 2003

Suleiman Baraka

UNIVERSITE PIERRE & MARIE CURIE
Faculté des Sciences de Paris

THESE DE DOCTORAT DE L'UNIVERSITE PARIS 6

Spécialité

Astrophysique

Présentée par

M Suleiman M. BARAKA

Pour obtenir le grade de
DOCTEUR de l'UNIVERSITE Paris -6

Sujet de la thèse :

Etude de l'interaction entre le vent solaire et la magnétosphère de la Terre : Modèle théorique et Application sur l'analyse de données de l'événement du Halloween d'octobre. 2003

Soutenue le 21.03.2007

Devant le jury composé de :

Dr Hab Barbara Popielawska	Rapporteur
Dr. Philippe Louarn	Rapporteur
Dr. Michel Blanc	Président de jury
Pr. Laurence Rezeau	Membre de jury
Dr. Lotfi Ben Jaffel	Directeur de thèse

Paris, 2007

Abstract

A new approach, using a 3D electromagnetic particle-in-cell (PIC) code, is presented to study the sensitivity of the Earth's magnetosphere to the variability of the solar wind bulk velocity. Starting with a solar wind impinging upon a magnetized Earth, time was let to the system so a steady state structure of the magnetosphere was attained. Then an impulsive disturbance was applied to the system by changing the bulk velocity of the solar wind to simulate a depression in the solar wind dynamic pressure, for zero, southward and northward interplanetary magnetic field (IMF). As a result of the applied disturbance, an air pocket effect that could be described as a ~15 Re wide gap is formed for all cases of IMF condition. As soon as the gap hit the initial bow shock of the steady magnetosphere, a reconnection between the Earth's magnetic field and the southward IMF was noticed at the dayside magnetopause (MP). During the expansion phase of the system, the outer boundary of the dayside magnetopause broke up in the absence of the IMF, yet it sustained its bullet shape when a southward and a northern IMF were included. The time relaxation of the MP for the three IMF cases was studied. The code is then applied to study the Halloween event of October 2003. Our simulation produced a new kind of air pocket, a rarefied space that was generated following a strong gradient in the impinging IMF. Such a feature is quite similar to observed hot flow anomalies and may have the same origin.

Table of Contents

List of Figures

Dedications

To the memory of my father with love

Epigraph

'Dieu ne joue pas aux dès', A. Einstein.
'Qui êtes-vous Einstein ; pour dire à Dieu ce qu'il doit faire ?',N. Bohr

I fled being trapped in Gaza, and found myself trapped in Sun-Earth Connection in France; where to go then?

Suleiman Baraka
Paris, 2007

Acknowledgements

First, I would like to thank Dr Lotfi Ben Jaffel, my thesis advisor, for his great intellect, outstanding knowledge in our field and for his constant and endless help, encouragement, and insightful guidance. Any time, during the last three years, I knocked at his door for any question I took back an answer with enthusiasm. Working with Dr Ben Jaffel taught me devotion, task orientation and to acquire extraordinary power to switch off distractions of what so ever type. I have been extremely fortunate to carry out my research under his supervision.

I would like to thank the jury of my thesis, Dr Michel Blanc (President) from CESR-Toulouse-France, Dr Philippe Louarn from CESR Toulouse-France, Dr Barbara Poplielawska from SRC Warsaw-Poland, Dr Laurence Rezeau from CETP/IPSL Velizy-France

My gratitude goes to the French government represented by the ministry of foreign affairs through the consulate general of France in Jerusalem for financially supporting my PhD thesis in France. My thanks go to CROUS de Paris for their support especially Mme Jeanne Marie Rousseaud.

Institut d'Astrophysique de Paris (IAP) an affiliate institute to the university of Pierre and Marie Curie University-Paris VI, was the place where I carried out my research for my PhD. I convey my sincere thanks to the administration of the IAP. I name here Dr Laurent Vigroux the director of IAP, Valerie Bona, Nicole Blondin and Nabila Hamdaoui for their continuous help and who made things easy when needed. I want to thank also the people who were around me all my stay in the laboratory, Prof Alfred Vidal-Madjar, Dr Roger Ferlet, Dr Alain lecavlier, Dr Guillame Hebrard.

I would like to thank the staff of Space Research Center-SRC in Warsaw-Poland to receive me three times to carry out my research at their center. I received warm welcome. I name here Dr Barbara Popielawska for her comments and invaluable advices in my work. I thank Jola Grygorczuk for her help in IDL graphics. I would like also to thank the director of the SRC and the staff for their eagerness

to help to establish the future space project in Palestine, especially Dr Iwona Stanislawska for her ionosphere data stories.

I would also like to especially thank Dr Floyd Herbert and Dr Gilda Ballester from LPL, university of Arizona –USA for their support, courage and for revising my first paper. I really very much enjoyed the company of Dr Herbert and the discussion I had with him in space physics during his stay in France.

My deep thanks to Dr Walter Harris from university of Washington Seattle for his support and the very excited discussion in science and politics, with a very high spirit of sense of humor. I also thank my colleague Olivia Dawson from JPL.

I am greatly indebted to the memory of my father, who devotedly spent his entire life to motivate his children to go for higher education, which he couldn't be enrolled in himself for some reasons. Twelve brothers and sisters have a university degree and five of them have a graduate degree. Thanks to Sayed and Iman. I thank all my brothers and sisters to make the dream of our beloved deceased father come true. I thank my mother for keeping me in her prayers day and night during my research.

I would like to thank my wife, Eiman for having an extraordinary responsibility to deal with four children (Mohammed, Ibrahim, Waad and Daoud) during the span of three years, that I haven't seen them except for few days. I thank my children for their patience on my absence.

I also would like to thank the Palestinian National Authority and the Palestinian General Council of Personnel for giving me a paid leave to acquire my PhD in France.

My friends JC Mauduit, Michal Maciejewski and François Ricquebourg deserve brotherly thanks. I would like also to thank, Prof Mohammed Shabat, Dr Kamal Rashid, Dr Fateen Haddad,

Dr Hassan Shaaban, Dr Awad Hijazi, Mr Tayser Khatib, and all my friends for there support and courage.

During my thesis work the scientific visits, conferences, summer school, software and other logistics were supported by Centre National d'Etudes spatiales –CNES, project INSPIRE , ISYA and the IAP.

Chapter One

Introduction

1.1 Prelude

We live in the heliosphere, the outer atmosphere of the Sun. The space beyond Earth's protective atmospheric cocoon is highly variable and far from benign. It is the one part of the cosmos accessible to direct scientific investigation, our only hands-on astrophysical laboratory. A host of interconnected physical processes, strongly influenced by solar variability, affect the state and structure of the Earth's atmosphere despite the shield offered by the magnetosphere from external ionized particles.

Indeed, as soon as the solar wind flow reaches the Earth's orbit, the geomagnetic field opposes the impinging particles and IMF producing a barrier, the magnetopause that should deflect the flow around. The inter-relation between fields and particles will induce a complex network of electric currents in the system that will shape the steady state structure of the magnetosphere, with its known features such as the magnetosheat, the cusps, the lobes, etc. It took to the scientific community more than 40 years to discover all theses intrinsic properties thanks to several space and ground missions (SPUTNIK'S, EXPLORER'S, VOYAGER'S, GEO'S, INTERBALL'S, SOHO, etc). All these discoveries represent a tremendous advancement in our knowledge of the geo-space, a picture that was soon greatly distorted by the complex and quite unknown solar wind element.

Geomagnetic activity can be divided into two main categories, storms and substorms. According to Gonzales et al. (1994), a storm is an interval of time when a sufficiently intense and long-lasting interplanetary convection electric field leads, through a substantial energization in the magnetosphere-ionosphere system, to an intensified ring current strong enough to exceed some key threshold of the quantifying storm time Dst index. The electric field mentioned is composed of solar

wind velocity and southward IMF (Bz). Of these, the magnetic field is found to be more important; indicating that the mechanism for the energy transfer includes magnetic field merging. The largest storms are often related to coronal mass ejections from the Sun (e.g., Gosling et al., 1991). In these cases, the related enhancements of solar wind velocity accompanied by southward IMF direction result into Sudden Storm Commencements (SSC). These storms are typically non-recurrent or transient. The more moderate storms are often recurrent with the solar rotation period.

According to the classical substorm injection hypothesis, ring current is enhanced via energization and injections of plasma sheet particles from the tail towards the inner magnetosphere during substorms, which are typical for storm times. However, this view has been under attack for some time now and according to the recent works by Iyemori and Rao (1996) and Siscoe and Petschek (1997) the substorm expansion phases act as energy dissipation term and the southward IMF as an input term in the energy balance equation; more can also be found in the work of McPherron (1987).

Beyond storm and sub-storms, other key processes are induced in the Earth's magnetosphere by the solar activity. Two of the main topics that have been extensively studied in the past, and are of interest in this thesis, are the motion of the magnetopause boundary and the occurrence of reconnection in different regions of the magnetosphere. Chapman and Ferraro (1931, 1932) were first to discuss the existence of a boundary to the Earth's magnetic field. During 1950's, as the concept of continuous solar wind emerged, it was obvious that such a feature should be a permanent feature of the magnetosphere. In the early 1960's, Explorer 10 and 12 provided the first measurements of this boundary (Cahill and Amazeen, 1963) that was to be called magnetopause. It plays an important role in space physics, since the coupling between the solar wind and magnetosphere occurs through it. Outside magnetopause, we find the shocked solar wind region, magnetosheath, and just inside are the magnetospheric boundary layers. In the first approximation, the magnetopause is formed at a distance where the solar wind

dynamic pressure equals the magnetic pressure of Earth's field. At this location, typically around 8 - 11 Re away on the Earth - Sun line, a large scale duskward (Chapman-Ferraro) current develops in the dayside magnetopause to cancel the Earth's field outside. At the same time, the dipole field inside is increased, being now about the two times the nominal dipole value.

Since the first spacecraft observations of the noon magnetopause position near 10 Re, it has been clear that the magnetopause boundary is frequently in motion under fluctuating pressure of the Solar Wind (Sonnet et al., 1960; Cahill and Amazeen, 1963; Cahill and Patel, 1967; Kaufmann and Konradi, 1969; Aubrey et al., 1971). The standoff distance of the magnetopause can be determined from pressure balance between the planetary magnetic field pressures—the particles make only a negligible contribution—and the dynamic pressure of the solar wind (neglecting the small contribution of the interplanetary magnetic field (IMF)). It is clear that when the parameters defining the pressure balance change, the position of the magnetopause will also vary (Semenov et al., 2002). From this it follows that the primary source of the magnetopause motion is the change in the dynamic pressure of the solar wind. However, there is another source that makes magnetopause moves earthward even when the dynamic pressure is constant: it is when the magnetic field lines at the magnetopause are bent back toward the tail. This will intensify the magnetic field lines flux in the nightside. This phenomenon is called “erosion” and was identified in the 1970s when magnetopause crossings made by OGO 5 spacecraft were investigated (Aubrey et al., 1970; Fairfield, 1971). There are recent observational signatures of the erosion process in the inner magnetosphere reported by Sibeck (1994) and Tsyganenko and Sibeck (1994). Results of the observations of the macrostructure of the magnetosphere revealed occasional positions of the magnetopause at distances much closer than 10 Re, usually associated with magnetic storms (Cummings and Coleman, 1968; Lezniak and Winckler, 1968; Skillman and Sugiuram, 1971). The interplanetary magnetic field (IMF) was and is still a key player in

the interrelated interactions, enhancement, and modification of the macrostructure of the Earth magnetosphere. The effect of the IMF component on the magnetospheric activity has been extensively documented. It minimizes under the northward IMF ($B_z \geq 0$), while it increases with increasing magnitude of southward IMF ($B_z \leq 0$), as evidenced, for example, by both the A_E index (Akasofu, 1980) and the cross-polar cap potential (Cowley, 1984; Rich and Hairston, 1994; Boyle et al., 1997). On the other hand, much less attention has been given before these studies to the impact of the Solar Wind dynamic pressure variability on the magnetospheric activity. It is only recently that several studies tried to assess the link between observed changes in the magnetosphere and the Solar Wind dynamic pressure variability (Boudouridis et al., 2003; Lee and Lyons, 2004). A notable feature in many of these studies is the pressure-induced magnetospheric response to the preexisting IMF orientation (Zesta et al., 2000; Shue and Kamide, 2001). A SW pressure enhancement occurring under a steady southward IMF condition produces a prominent and easily observable response as all current systems exhibit an increase in magnitude and a strong correlation with the Solar Wind density. In contrast, under northward IMF, a similar change in the dynamic pressure would induce a weaker response in the magnetosphere (Boudouridis et al., 2003). Note also that the geosynchronous magnetic field also exhibits different behavior for the different IMF orientation after a Solar Wind pressure front impact (Lee and Lyons, 2004).

Magnetic reconnection is an important process for transferring Solar Wind plasma into the Earth magnetosphere because it may modify the magnetosphere configuration. Evidence of this process is found at the Earth magnetopause and in the cusps. At the magnetopause, the evidence typically consists of one or more of the following: a nonzero normal component of the magnetic field (Sonnerup et al., 1981), flow velocities of ions or (electrons) that satisfy certain jump conditions across the boundary (Sonnerup et al., 1981; Paschmann et al., 1986), ion and electron distribution functions that are

consistent with transmission and reflection of Solar Wind, and magnetospheric ion and electron population across an open "magnetopause boundary" (Sonnerup et al., 1981; Fuselier, 1991, 1995). In the cusps, the evidence consists of dispersive ion and electron signatures consistent with entry and acceleration of magnetosheath plasma across an open magnetopause (Lockwood and Smith, 1996).

The magnetic field topology arising from the occurrence of magnetic reconnection at the Earth's magnetopause results in the presence of a boundary layer inside the magnetopause and contains mixture of magnetosheath and inner magnetospheric plasmas (Eastman and Hones, 1979; Ogilvie et al., 1984; Mitchell et al., 1987; Hall et al., 1991). Field lines in the latter region are magnetically connected to the open magnetopause; typical signatures in this layer are the presence of leaking magnetospheric particles as well as heated magnetosheath plasma, interpreted as having twice passed through the reconnected magnetopause (Fuselier et al., 1997). All these results have been obtained for a southward steady IMF, but many other studies also covered the northward IMF impact on magnetospheric topology (Gosling, 1996). Indeed, under the northward IMF, high latitude reconnection occurs between the magnetosheath and the lobe magnetic field lines (Gosling et al., 1991; Kessel et al., 1996). Because this process may occur at both the northern and southern hemispheres, Song and Russell (1992) proposed the creation of newly closed magnetospheric field lines at the dayside magnetopause when the IMF is strongly oriented northward. This prediction was later supported by case studies (Le et al., 1996; Onsager et al., 2001). Another type of internal reconnection has been recently postulated by Watanabe et al. (2004), who interpreted simulation results by Tanaka (1999) for northward IMF with a clock angle of 45 degrees (no dipole tilt) in terms of sequential reconnection that causes polar cap bifurcation in the polar ionosphere.

It follows from above that all indications tend to support that the general problem of the impact of the solar wind activity on the Earth magnetosphere is a wide and quite rich topic that require more than one

study to approach a comprehensive understanding of its action. Before going into the detail of our proposed strategy to handle this complex problem, a brief description of the structure of the Earth magnetosphere and its regions will be presented, based on extracts from M. Kivelson and Russell book *Introduction to space physics (1997).* This brief description will be quite useful all along the draft. Next, the motivation of this thesis will come forth, and at the end of this chapter, an outline of the thesis will be presented to briefly introduce each chapter's topics.

1.2 Spot Lights on the Earth Magnetospheric Structure and the Associated Dynamical Process

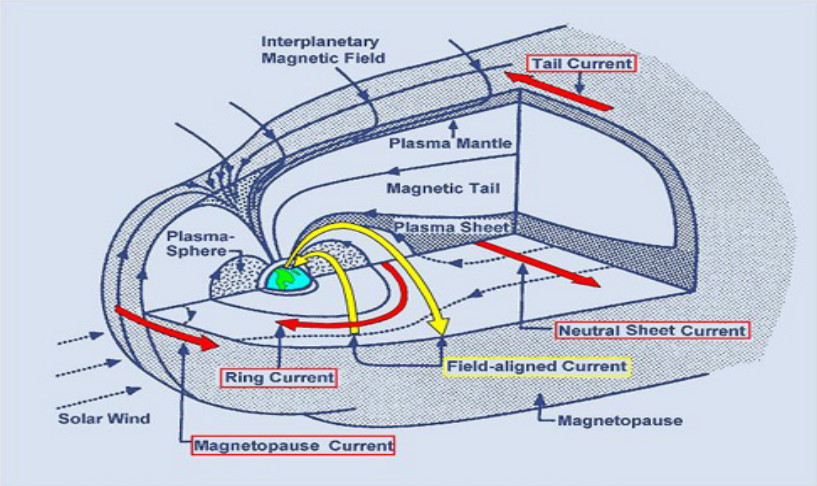

Figure 1.1 Earth magnetospheric structures (modified from Kivelson and Russell, 1997)

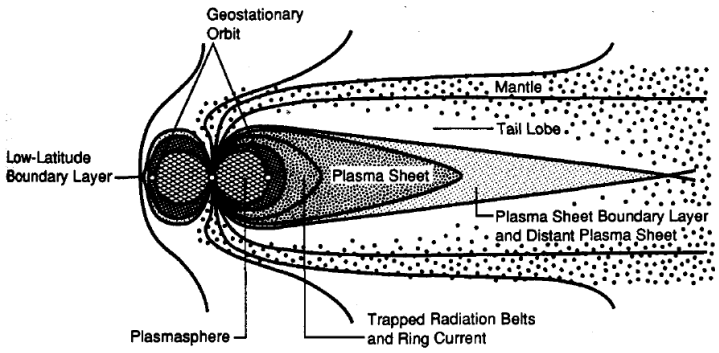

Figure 1.2 schematic diagram of plasma regions of the Earth magnetosphere (Kivelson and Russell, 1997)

In the light of what has been presented in section 1.1 of this chapter, and in addition to the material described within the context of the thesis, the definition of terms and references to them is a must. Therefore, we briefly come across the description of the Earth's magnetosphere regions. Accordingly, the Earth's magnetosphere consists of several regions that are created by the field topology (Figures 1.1 and 1.2). The magnetopause can be considered as a boundary separating a vacuum magnetic field from plasma. The location of this boundary can be reliably calculated by requiring the total pressure on the two sides of the boundary to be equal. As a good approximation, the pressure in the magnetosphere, which is mainly magnetic pressure, must match the pressure in the magnetosheath, which is a combination of thermal plus magnetic pressures

The magnetotail is formed by tail lobes and the plasmasheet. In the inner magnetosphere we have the plasmasphere mapping to mid- and low-latitudes. Overlapping both plasmasphere and inner plasmasheet are radiation belts and ring current. Regions closest to the magnetopause are called boundary layers. Furthermore, another principal region is the plasmasheet, often referred to as the "central plasma sheet" to emphasize its distinctness from the plasmasheet boundary layer, consists of hot (kilovolt) particles that have nearly symmetric velocity distributions. Number densities typically are 0.1-1 cm^{-3}, a little bit higher than those of the plasma-sheet boundary layer. Flow velocities typically are very small compared with the ion thermal velocity. The ion temperature in the plasmasheet is almost invariably about seven times the electron temperature (Baumjohann, Paschmann, and Cattell, 1989).

More over, the magnetic field lines of the Earth can be divided into two parts according to their location on the sunward or tailward side of the planet. Between these two parts on both hemispheres are funnel-shaped areas with near zero magnetic field magnitude called the polar cusps. They provide a direct entry for the magnetosheath plasma into the magnetosphere (e.g., Reiff et al., 1977; Marklund et al., 1990; Yamauchi et al., 1996). In this thesis work, ionosphere, Earth tilts and rotations are not taken

into account, as the study profoundly seeks to discuss the basic controlling elements of the interaction between the Earth's magnetosphere and the solar wind dynamic pressure.

1.3 Motivation of the Thesis

The general problem of the response of the Earth's magnetosphere to solar wind variability in terms of the system topology and dynamics on large scales was and still is a key research topic for magnetospheric and space plasma physicists. This is a quite complex problem that no single study could handle in a satisfactory way.

Our study will thus focus primarily on the dayside magnetopause of the Earth's magnetosphere for which available *in situ* observations are quite abundant. This region was also selected because fields and plasmas in the dayside magnetosphere tend to be more ordered and thereby make field lines mapping more tractable, and also because dayside dynamics tend to be directly driven by solar wind forcing (Murr, 2004)

The scientific literature in this regard is rich with observations **(**i.e., Hasegawa, et al.,2004; Haaland et al, 2004; Balogh et al, 2001; Bauer et al, 2000) as well as MHD calculation (i.e. Guzdar,et al.,2001; Reiff et al, 1985; Lyon et al, 1998 **)**, pertaining to the aforementioned problem, yet these approaches are not comprehensive enough to provide an understanding of the full nature of the solar wind-Earth magnetospheric interaction, particularly at the dayside magnetopause. In the MHD models, only ensemble-averaged parameters are available, with an assumed distribution of the particles velocity as best described by a collection of several Maxwellian functions in the most evolved version of the multi-fluid approximation (Winglee et al., 2005). These calculations do not determine the plasma microphysics that is specifically under the influence of the magnetic field where velocity distributions along and across the field lines are generally different. In addition, on the observational side, and for

those regions near the Earth accessible to satellites, there are more limitations than the only difficulty of coverage of a large space simultaneously.

A difficult time-space problem is faced, because when satellites are moving, temporal changes cannot be distinguished from spatial variations. Further complications arise from the fact that no satellite can provide a global image of the interaction process of the solar wind with the Earth magnetosphere because in the real world, the magnetospheric macrostructure is already set when observed; therefore, we cannot identify the specific interaction that shaped that structure (Baraka and Ben-Jaffel, 2007). Moreover, *in situ* measurements can generally characterize the plasma only on scales smaller than the Debye length. With the launch of the NASA IMAGE satellite in March 2000, the promise of magnetospheric imaging began to materialize. IMAGE provides nearly-continuous imaging of the inner magnetosphere on a nominal timescale of 2 minutes (Burch, 2005). Simultaneous measurements of both temporal and spatial scales are rare, making it difficult to interpret the interrelationship of the two. CLUSTER, a set of satellites launched in 2000, are intended to fill the gap between small- and large-scale properties with simultaneous *in situ* observations obtained by the satellites in different regions of the magnetosphere, thereby providing a 3D map (in terms of density and field configuration) of the magnetosphere. The CLUSTER II spacecraft have state-of-the-art plasma instrumentation to measure electric and magnetic fields, from quasi-static up to high frequency, as well as electron and ion distribution functions from around zero to a few MeV in energy (Escoubet et al., 2000). In addition, large-scale space events of interest are infrequent and unique, and hence they do not lend themselves to general models of space plasma dynamics. Recently, the violent solar eruptions of the October-November 1003 are one of the best observed outbreaks of intense solar activity to date. Gopalswamy et al, (2005) summarized a total of 74 papers that dealt with the said event, and published in the *Journal of the Geophysical research, Geophysical Research Letters, and*

Space Weather, none of which used a particle code to simulate the effect of this unusual event on the macrostructure of the Earth's magnetosphere, and to study the microphysics of each region separately.

Such considerations highlight the importance of computer simulation by Particle-In-Cell (PIC) electromagnetic (EM) particle codes. This approach provides a tool that spans all boundary conditions instantaneously and globally while keeping track of the plasma physics locally on a selected scale (here, the planet radius). Because at each unit time of the code the microphysics of the plasma is accessed at the considered length scale, this method reveals details of the magnetosphere well beyond the limitations of the existing 3D MHD methods and the local imaging by orbiting satellites of certain areas of the magnetosphere.

In the past, several codes have been developed that were successful in recovering the main features of the Earth's magnetosphere or localized regions of it (Nishikawa et al., 1997; Wodnicka, 2001; Cai et al., 2006; Pritchett, 2005). In this study, an updated version of the so-called TRISTAN code (Buneman, 1993, Ben-Jaffel et al., 2006) will be used and that will be carefully introduced in chapter 2. With the PIC code in hands, our strategy in this thesis is to try to create a methodology, by which a quantitative evaluation of the sensitivity of the Earth's magnetosphere to the solar wind activity is obtained. This strategy will be presented in chapters 3 to 6. Moreover, once this strategy is built up, the interrelated impacts of the different parameters that affect the Earth's magnetosphere are then extracted accordingly (chapters 7-8).

1.4 Thesis outline

In this thesis I use a PIC EM fully relativistic code to study the interaction between the Earth magnetosphere and solar wind. Each chapter contents was introduced individually and summed up in concluding remarks.

Chapter 2 the PIC code is described.

Chapter 3 establishes the code validity on slow, moderate and strong solar wind as it reacts with the Earth magnetosphere. The successful simulations of the different dynamic pressure of solar wind practically introduce the idea of creating depression in the solar wind flow.

Chapter 4 presents the simulation of the response of the Earth's magnetosphere to a depression in the solar wind dynamic pressure after the simulation box was updated in terms of its size and the number of electrons-ions pairs that filling it, during the absence of the IMF.

Chapter 5 presents the simulation of the Earth's magnetosphere to the same depression in the solar wind dynamic pressure but during a southward IMF

.

Chapter 6 presents the simulation of the Earth's magnetosphere to the same depression in the solar wind dynamic pressure but during a northward IMF

Chapter 7 presents the application of the PIC code to simulate the unusual solar activity of the Halloween 2003 event.

Chapter 8 summarizes the thesis work and set some future work and plans.

Chapter 2

Simulation Model (Modified Tristan Code)

2.1 Introduction

The technical tool of this work is a particle-in-cell (PIC) code, first developed by Buneman (1993). This code is a fully 3D electromagnetic and relativistic code. In our model, the magnetosphere is sketched as an ensemble of macro-particles, the macro-ions and the macro-electrons. Motions of these macro-particles are simulated in 3D under the influence of electric and magnetic fields through the Lorentz law. The Earths' dipole field strength was determined in the code by generating a ring current. The ring current was made to evolve from zero to its full value within the first 64 time steps smoothly and gently, to avoid large transients. The position of the current loop is located at the center of the Earth position.

The fields themselves are described by the Maxwell equations. By its construction, the code offers the advantage to contain the complete physics of the problem. However, a price has to be paid to re-scale some of the plasma parameters in order to perform the simulations in realistic CPU time. The complexity and the limitation of the code, as it was initially written, made it difficult to be accessed, thusly limiting its applications to few cases. In other words, the difficulty is in establishing good resolutions in time and space and limitation with smaller m_e/m_i mass ratio. However, this method is superior to MHD simulations in some issues such as including kinetic processes and separating electrons and ions dynamics [Nishikawa, 1997; Wodnicka, 2001; Cai et al., 2006]. We are using a modified version of the code in terms of numerical stability, computer CPU, and consistency with the

real world—a version developed in collaboration between the Institut d'Astrophysique de Paris and the Space Research Center of Poland [Ben-Jaffel et al., in preparation, 2007]. In our simulation, we applied radiating boundary conditions for the fields as proposed by Lindman [1975]. At the boundary, macro-particles are annihilated. Ions and electrons are computed, solving the Lorentz equation of motion, Boris [1970]. Fields are updated using Maxwell equations. A charge conservation argument is applied following formulas of Villasenor and Buneman [1992]. The plasma was initially neutral and characterized as isotropic Maxwellian velocity distribution. The solar wind drift velocity and the electron to proton mass ratio are the basic controlling parameters in the code. These two parameters are scaled so that the main features of the Earth's magnetosphere, such as the magnetopause standoff distance, are recovered for a reference solar activity. This scaling offers the benefit to significantly reduce the computer CPU time while keeping track of the main physical processes, such as separating the dynamics of electrons and ions instantaneously (Buneman, 1993; Nishikawa et al., 1995).

In the following, the code structure and the way the fields and the particles are updated are presented. Scaling of code and plasma parameters is very crucial in building up an idea about the link between simulations and the real world. As we use an updated copy of TRISTAN (TRIdimentional STANford) code, most of the materials of the code description in this chapter are based on a reference paper by Cai et al. (2003). To start this description, the Courant condition will first be derived to show how time is scaled.

2.2 Courant Condition

Courant Condition states that, in any time-dependent computer simulation, the time step must be kept small enough so that information has enough time to propagate through the space discretization. To

derive that condition, let's consider a physical quantity A(**r**,t) in three dimensions that has a wave structure with a wave number k and frequency ω

$$A(r,t) = A_0 \exp(ik.r - i\omega t) \tag{2.1}$$

We compute the derivative by a centered-difference equation as

$$\begin{aligned} \frac{\Delta A}{\Delta r} &= \frac{A(r_0 + \Delta r/2, t) - A(r_0 - \Delta r/2, t)}{\Delta r} \\ &= \frac{\exp(ik\,\Delta r/2) - \exp(-ik\,\Delta r/2)}{\Delta r} A(r_0, t) \\ &= i\frac{\sin(k\,\Delta r/2)}{(\Delta r/2)} A(r_0, t) \end{aligned} \tag{2.2}$$

Now take the spatial derivative $\partial A/\partial r$:

$$\frac{\partial A}{\partial r} = ikA(r_0, t) \tag{2.3}$$

Comparing the $\Delta A/\Delta r$ with the spatial derivative $\partial A/\partial r$, we find that:

$$K = \frac{\sin(k\,\Delta r/2)}{(\Delta r/2)},\ \kappa \text{ here is replaced by K} \tag{2.4}$$

by the same way if we calculate from eq. (2.1) $\frac{\Delta A}{\Delta t}$ and $\partial A/\partial t$, then we find:

$$\Omega = \frac{\sin(\omega \Delta t/2)}{\Delta t/2},\ \omega \text{ is replaced by } \Omega \tag{2.5}$$

The dispersion relation is obtained by neglecting the current density j; noting that Tristan does not employ charge density but rather charge fluxes i.e. amount of charge flowing through the faces of a cubic mesh. Assuming the electromagnetic wave with a frequency ω and a wave number κ with maximum wave number $K_{max} = \pi/\Delta r$,

$$\sin^2(\omega\Delta t/2) = \left(\frac{c\Delta t}{\Delta x}\right)^2 \tag{2.6}$$

$$\Delta r = \sqrt{(\Delta x)^2 + (\Delta y)^2 + (\Delta z)^2} \;\Rightarrow \Delta x = \frac{\Delta r}{\sqrt{3}} \tag{2.7}$$

Use (2.7) and compare (2.4) and (2.5) and use $\Omega^2 = c^2 K^2$,

Then equation (2.6) becomes:

$$\sin^2(\omega\Delta t/2) = \left(\frac{c\Delta t\sqrt{3}}{\Delta r}\right)^2 \tag{2.8}$$

if $c\Delta t\sqrt{3}/\Delta r > 1$, then ω becomes complex, giving rise to a numerical instability. If $c\Delta t/\Delta x < 1$, then the system is marginally stable, therefore, we have the Courant Condition in 3-D:

$$\frac{\Delta r}{\sqrt{3}} \geq c\Delta t \tag{2.9}$$

Now to calculate the value of Δt, we first require the numerical stability of the code by using the Courant condition. From Eq. 2.9, taking the upper limit of Δr as 1Re, we derive:

$$\Delta t = \frac{\Delta r}{2\sqrt{3}\times v_{sw}} \cong \frac{6335}{2\sqrt{3}\times 500} = \frac{6.335}{\sqrt{3}}\,\text{sec} \tag{2.10}$$

In real plasma data, the 'Δr' corresponds to 1 Re=6335 km and the 'V_{sw} 'corresponds to 500 km/s . This value of the units of time is of few seconds and the corresponding length scale is of 1 Re will help to make the connection between our simulations and the real plasma world.

2.3 Basics of Tristan Code

The control equations of TRISTAN code are Maxwell and Newton-Lorentz equation. Effects of Earth rotation and thermal expansion of solar wind are not included in the simulation process.

In TRISTAN code, only two curls of Maxwell equations are solved:

Faraday's Law

$$\frac{\partial \vec{B}}{\partial t} = -\vec{\nabla} \times \vec{E} \tag{2.11}$$

Ampere's Law,

$$\vec{\nabla} \times \vec{B} = \mu_0 \vec{j} + \frac{\partial \vec{E}}{\partial t} \tag{2.12}$$

where $\vec{j} = \sum (n_i q_i \vec{v}_i - n_e q_e \vec{v}_e)$

TRISTAN code scales such that $\varepsilon_0 = 1$ and hence $\mu_0 = 1/c^2$. This also means $E = D$. Instead of recording components of B or H, TRISTAN records Bx, By, Bz of c**B** (alias **H**/c). This makes symmetry for electric field and magnetic field $(E \leftrightarrow B)$ in Maxwell equations. The light speed c=0.5 in the code.

Throughout, TRISTAN uses a rectangular cubic grid with $\Delta x = \Delta y = \Delta z = 1$ and time discretisation with $\Delta t = 1$. Before and after moving (or pushing) the particles, B is updated in two half steps so that it is available at the same time as E for the particle update. The velocity of the solar winds was selected such that it is smaller than c but strong enough to reflect its strength compared to other velocities Vsw=0.5 c (c=0.5).

Before going into the details of the both fields and particles updates, we introduce two charts to show how the fields, position, charge density and time steps are advanced in the code.

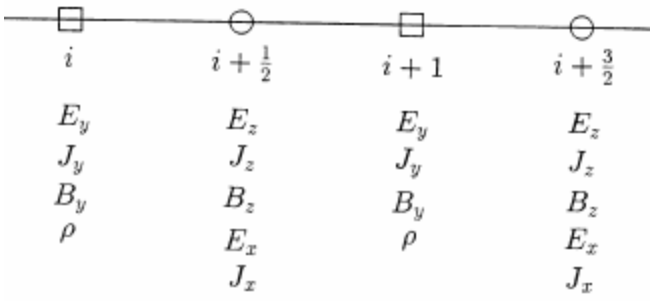

Figure 2.1 grid assignment

Figure 2.1 shows the full-integer grids at $i\Delta x$ (i = 1,2,3, ..., N,) and half-integer grids at(i + 1/2) Δx. The E_y, B_y, J_y and ρ are defined at the full-integer grids, and E_x, E_z, B_z, J_x, J_z at the half-inter grids as shown in Figure 2.1. This assignment of the electric and magnetic fields **E** and **B** realizes centered difference forms for the spatial derivatives in Maxwell's equations. The components J_x, J_y, J_z of the current density must be assigned to the same grids of E_x, E_y, E_z respectively, because J contributes directly to the time integration of E.

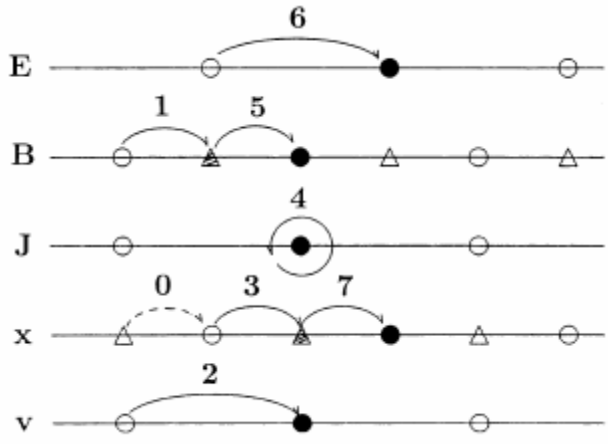

Figure 2.2 Time step chart

The quantities of the field and particles are advanced in time based on the sequence shown in Figure 2.2. We define a full-integer time $n\Delta t$ and a half integer time $(n + 1/2)\Delta t$ with a time step Δt. Basically, the electric field E at the full-integer time and the magnetic field B at the half-integer time are integrated in time by the leap-frog method. However, the magnetic field B is advanced twice by a half time step $\Delta t/2$ to obtain intermediate values for the particle pushing fields at the full-integer time. The particle positions x at the full-integer time and velocities v at the half-integer time are also advanced by the leap-frog method. The positions are advanced twice with a half time step $\Delta t/2$ to obtain intermediate values for computation of the current density J at the half-integer time. The current density J is computed from the positions and velocities of particles.

2.4 Magnetic Field Update

The staggered grid mesh system, known in the computational electromagnetic community as Yee lattice (Yee, 1966), is shown in Fig.2.3. It ensures that the change of B flux through a cell surface equals the negative circulation of E around that surface and the change of E flux through a cell surface equals the circulation of B around that surface minus the current through it. Here B and E are in a symmetry form except subtracting the charge flux J in Ampere equation. Charge flux J is calculated and subtracted after the particles are moved later in the program. Thus magnetic fields are updated as follows:

The change of B flux can be expressed as:

$$\frac{\partial B}{\partial t} = -c\begin{pmatrix} i & j & j \\ \frac{\partial}{\partial x} & \frac{\partial}{\partial y} & \frac{\partial}{\partial z} \\ E_x & E_y & E_z \end{pmatrix} = -c[i(\frac{\partial E_z}{\partial y} - \frac{\partial E_y}{\partial z}) \\ +\mathrm{j}(\frac{\partial E_z}{\partial x} - \frac{\partial E_x}{\partial z}) + k(\frac{\partial E_x}{\partial y} - \frac{\partial E_y}{\partial x})], \tag{2.13}$$

In Yee lattice, Ex, Ey, Ez, Bx, By, and Bz are, respectively, staggered and shifted on 0.5 from (i; j; k) and located at the positions as follows:

$$\begin{aligned} &E_x(i,j,k) \to E_x(i+.5,j,k) \\ &E_y(i,j,k) \to E_y(i,j+.5,k) \\ &E_z(i,j,k) \to E_z(i,j,k+.5) \end{aligned} \tag{2.14}$$

$$\begin{aligned} &B_x(i,j,k) \to B_x(i,j+.5,k+.5) \\ &B_y(i,j,k) \to B_y(i+.5,j,k+.5) \\ &B_z(i,j,k) \to B_z(i+.5,j+.5,k) \end{aligned} \tag{2.15}$$

In our simulation, we use integer grids. In both Eq. (2.4) and (2.5), i, j, k in the right-hand sides correspond to Fortran array indices notations and i, j, k in the left hand sides correspond to the real positions in the simulation domains as shown in Fig. 2.2. In this report, if the values "0.5" are added to either i, j, k in the array indices, then the array indices correspond to the real positions in the simulation domains.

2.5 Speed Limits

One sequence of using the Courant Condition is the control of the speed limit on particles. With c already set to 0.5, considerations of stability implies that the particles need not outrun the fields. If

electromagnetic effects are expected to be important, the Courant limit on $c\delta t$ will result in time scales such that the non- relativistic particles crawl through the mesh very slowly.

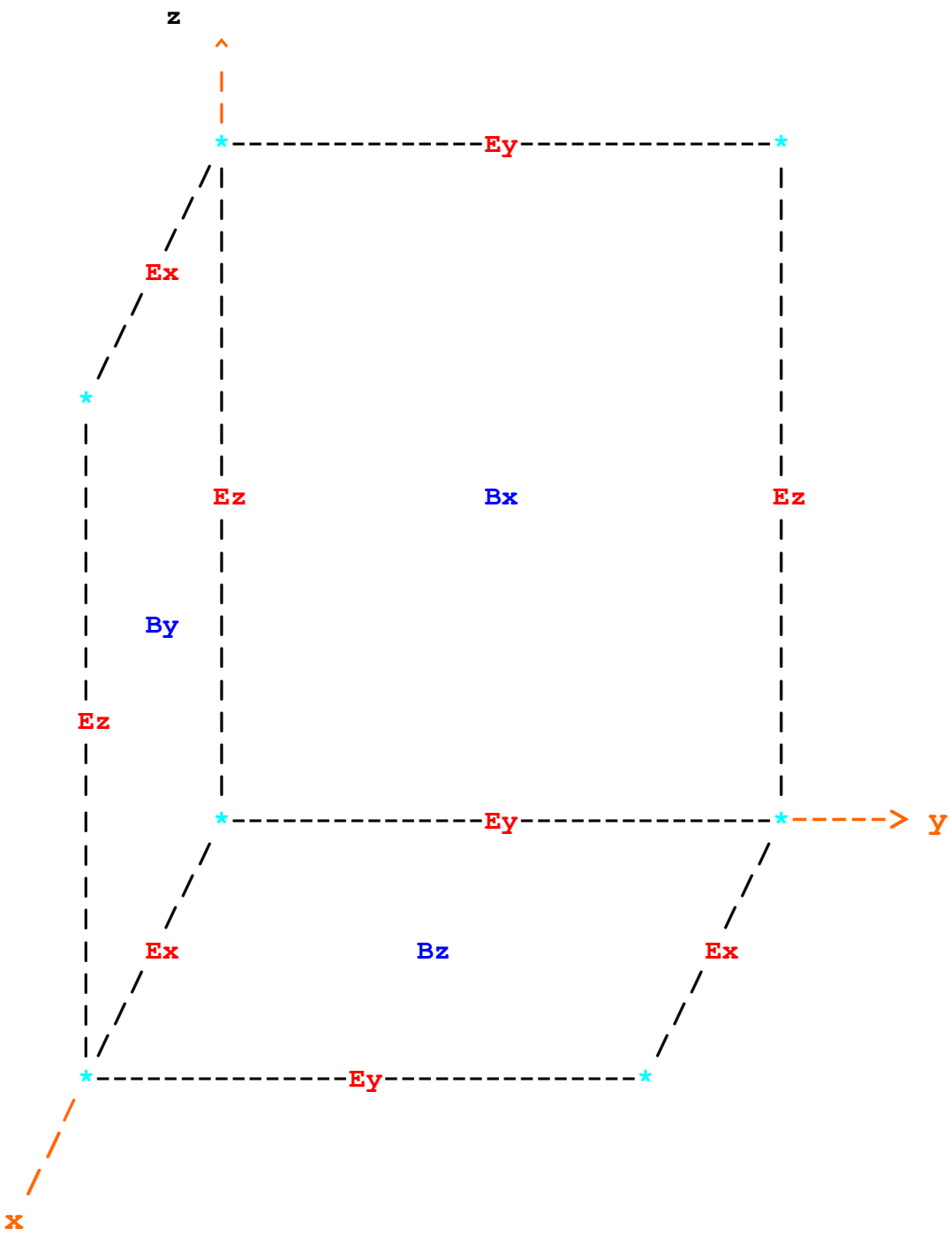

Figure 2.3 the position of field components in Yee lattice

Thus the magnetic field components Bx, By, Bz are, respectively, updated by the negative circulation of E around Yee lattice surface as follows:

$$\begin{aligned}\frac{\partial B_x}{\partial t} &= \left(B_x^{new}(i, j+.5, k+.5\right) - B_x^{old}(i, j+.5, k+.5))/\delta t \\ &= c[(E_y(i, j+.5, k+1) - E_y(i, j+.5, k))/\delta z \\ &\quad -(E_z(i, j+1, k+.5) - E_z(i, j, k+.5))/\delta y],\end{aligned} \tag{2.16}$$

Here $\Delta t = \Delta x = \Delta y = \Delta z = 1$. Thus we get the update form:

$$\begin{aligned}B_x^{new}(i, j, k) &= B_x^{old}(i, j, k) + \\ &\quad c[B_y(i, j, k+1) - B_y(i, j, k) - B_z(i, j+1, k) + B_z(i, j, k)],\end{aligned} \tag{2.17}$$

To get the update form of by, and Bz, the same procedures are as followed:

$$\begin{aligned}\frac{\partial B_y}{\partial t} &= \left(B_y^{new}(i+.5, j, k+.5\right) - B_y^{old}(i+.5, j, k+.5))/\delta t \\ &= c[(E_z(i+1, j, k+.5) - E_z(i, j, k+.5))/\delta x \\ &\quad -(E_x(i+.5, j, k+1) - E_x(i+.5, j, k))/\delta z],\end{aligned} \tag{2.18}$$

Same way when b in the z direction is concerned

$$\begin{aligned}\frac{\partial B_z}{\partial t} &= \left(B_z^{new}(i+.5, j+.5, k\right) - B_z^{old}(i+.5, j+.5, k))/\delta t \\ &= c[(E_x(i+.5, j+1, k) - E_x(i+.5, j, k))/\delta y \\ &\quad -(E_x(i+1, j+.5, k) - E_x(i, j+.5, k))/\delta x],\end{aligned} \tag{2.19}$$

$$\begin{aligned}B_y^{new}(i, j, k) &= B_y^{old}(i, j, k) + \\ &\quad c[E_z(i+1, j, k) - E_z(i, j, k) - E_x(i, j, k+1) + E_x(i, j, k)],\end{aligned} \tag{2.20}$$

$$B_z^{new}(i,j,k) = B_z^{old}(i,j,k) + c[E_x(i,j+1,k) - E_x(i,j,k) - E_y(i+1,j,k) + E_y(i,j,k)] \tag{2.21}$$

2.6 Electric Field Update

In Yee lattice, ex, ey, and ez are, respectively, staggered and shifted 0.5 from (i; j; k) and located at the positions as shown in Fig. 2.2

The change of E flux through a cell surface equals the circulation of B around that surface minus the current through it. First, the electric field is updated by the circulation of B around Yee lattice surface as follows:

$$\frac{\partial E}{\partial t} = c\begin{pmatrix} i & j & j \\ \frac{\partial}{\partial x} & \frac{\partial}{\partial y} & \frac{\partial}{\partial z} \\ B_x & B_y & B_z \end{pmatrix} = c[i(\frac{\partial B_z}{\partial y} - \frac{\partial B_y}{\partial z}) + \mathrm{j}(\frac{\partial B_z}{\partial x} - \frac{\partial B_x}{\partial z}) + k(\frac{\partial B_x}{\partial y} - \frac{\partial B_y}{\partial x})] \tag{2.22}$$

Thus the electric field components Ex, Ey, Ez are, respectively, updated by the circulation of B around Yee lattice surface as follows [3]:

$$\begin{aligned} \frac{\partial eE_x}{\partial t} &= \left(E_x^{new}(i+.5,j,k\right) - E_x^{old}(i+.5,j,k))/\delta t \\ &= c[(B_z(i+.5,j+.5,k) - B_z(i+.5,j-.5,k))/\delta y \\ &\quad -(B_y(i+.5,j,k+.5) - B_y(i,j+.5,k-.5))/\delta z], \end{aligned} \tag{2.23}$$

$$\begin{aligned} \frac{\partial E_y}{\partial t} &= \left(E_y^{new}(i,j+.5,k\right) - E_y^{old}(i,j+.5,k))/\delta t \\ &= c[(B_x(i,j+.5,k+.5) - B_x(i,j+.5,k-.5))/\delta z \\ &\quad -(B_z(i+.5,j+.5,k) - B_z(i-.5,j+.5,k))/\delta x], \end{aligned} \tag{2.24}$$

$$\begin{aligned} \frac{\partial E_z}{\partial t} &= \left(E_z^{new}(i,j,k+.5\right) - E_z^{old}(i,j,k+.5))/\delta t \\ &= c[(B_y(i+.5,j,k+.5) - B_y(i-.5,j,k+.5))/\delta x \\ &\quad -(B_x(i,j+.5,k+.5) - B_x(i,j-.5,k+.5))/\delta y], \end{aligned} \tag{2.25}$$

$$E_x^{new}(i,j,k) = E_x^{old}(i,j,k) + c[B_y(i,j,k-1) - B_y(i,j,k) - B_z(i,j-1,k) + B_z(i,j,k)] \quad (2.26)$$

$$E_y^{new}(i,j,k) = E_y^{old}(i,j,k) + c[B_z(i-1,j,k) - B_z(i,j,k) - B_x(i,j,k-1) + B_x(i,j,k)] \quad (2.27)$$

$$E_z^{new}(i,j,k) = E_z^{old}(i,j,k) + c[B_x(i,j-1,k) - B_x(i,j,k) - B_y(i-1,j,k) + B_y(i,j,k)] \quad (2.28)$$

After updating the electric field by the circulation of the magnetic field around that Yee lattice surface, charge flux J are calculated and subtracted after the particles are moved later in the program.

2.7 Particle Update

Newton-Lorentz equations are already in typical "update" form. The time centered finite difference version of the Newton-Lorentz particle update is:

$$v^{new} - v^{old} = \frac{qE\delta t}{m}\left\langle E + \frac{1}{2}\left(v^{new} + v^{old}\right) \times B \right\rangle \quad (2.29)$$

$$r^{next} - r^{present} = \delta t v^{new} \quad (2.30)$$

This shows that position must be leap-frogged over velocities. Hatree and Boris (Buneman, 1993) found a good physical interpretation of the steps in this explicit procedure:

1- Half an electric acceleration:

$$v_0 \leftarrow v^{old} \quad (2.31)$$

or

$$v_0 = v^{old} + qE\delta t/2m \quad (2.32)$$

2- Pure magnetic rotations:

$$v_1 \leftarrow v_0 \tag{2.33}$$

or

$$v_1 - v_0 = v_1 + v_0 \times qB\delta t/2m \tag{2.34}$$

3- Another half electric acceleration:

$$v^{new} \leftarrow v_1 \tag{2.35}$$

or,

$$v^{new} = v_1 + qE\delta t/2m \tag{2.36}$$

The Eq. (2.34) determining v_1 from v_0 is still implicit but its explicit form follows from: (1) dotting with $v_1 + v_0$ to check that the magnetic field does not work and that the magnitudes of v_1 and v_0 are the same, (2) dotting with B to check that components along B are the same, (3) crossing with $qB\delta t/2m$ and substituting back, then to give

$$v_1 = v_0 + 2 \times \frac{v_0 + v_0 \times b_0}{1 + b_0^2} \times b_0 \tag{2.37}$$

2.8 Relativistic generalization

In the code, the particle trajectory is integrated using a time-centered leap-frog scheme. Let

$$u = v, \qquad \gamma^2 = \left(1 - \frac{u^2}{c^2}\right)^{-1} \tag{2.38}$$

Here γ is denoted by relativistic factor. Newton-Lorentz Eq. (2.29) gives:

$$u^{n+\frac{1}{2}} - u^{n-\frac{1}{2}} = \frac{q\delta t}{m}\left[E^n + \frac{1}{2\gamma^n}\left(u^{n+\frac{1}{2}} + u^{n-\frac{1}{2}}\right) \times B^n\right] \tag{2.39}$$

$$r^{n+1} = r^n + v^{n+\frac{1}{2}}\delta t = r^n + \frac{u^{n+\frac{1}{2}}\delta t}{\gamma^{n+\frac{1}{2}}} \tag{2.40}$$

Where

$$(\gamma^{n+\frac{1}{2}})^2 = 1 + (\frac{(\gamma^{n+\frac{1}{2}})}{c}) \tag{2.40}$$

2.9 Conclusion and remarks

In our work, the grid size is $\Delta = \Delta x = \Delta y = \Delta z$, where $\Delta = 1$ Re and $\Delta t = 1$. Our simulation box size is (x, y, z) = (155Δ, 105Δ, 105Δ), loaded by $2x10^6$ electron-ions pairs, and the Earth position is located at (x, y, z) = (60Δ, 52Δ, 53Δ). The plasma parameters in our code are summarized as follows: the solar wind drift velocity was set to 0.5 c, applied along the x-direction. The code was initially run up to 900 Δt to build up the classical structure of the Earth's magnetosphere before applying any gap's effect on the system. Within the time range of 900<t<1000, the gap was created while the case study time range is 1001<t<1250 Δt. It is worth to note that the solar wind number density input is held constant during the different phases of the study. Our real time has been re-scaled in the code, based on Courant Condition (section 2.2)

In practice rescaling of Δt to real world time is quite complicated. In summary, scaling was done to bring the simulated system to about the expected structure of the Earth Magnetosphere (size, topology, etc). The injected solar wind density is *0.8* electron-proton pairs per cell ($0.8/\Delta^3$), and the mass ratio is *me/mi = 1./16.* After scaling, the thermal velocity is $vth_{e,i}$ *= (0.1, 0.025),* the plasma frequency is $\omega_{e,i}$ *= (0.89, 0.22),* and the Debye length $\lambda_{De,i}$ = (0.1, 0.1), where e, and i denote electron and ion respectively. It may be worth to remark that the way the PIC code was built is to have the fields evaluated over the grid nodes, while particles can have any position within the box. Kinetic effects of particles are then included, thought fields are averaged over a cell's scale (1 Re here) and the particles mass ratio, mi/me, is large but far from its real value. It follows that our PIC code is well designed for the study of the macro-structure of a magnetosphere but requires a denser grid and a better particle statistics for smaller scales (Cai et al., 2006).

Chapter 3

Code Test and Validation

3.1 Introduction

To study the sensitivity of the Earth's magnetosphere to the variability of solar wind bulk velocity, the first step is to build a steady state magnetosphere. In this chapter, the PIC electromagnetic code described in the previous chapter will be first tested on a smaller simulation box loaded with a small number of solar wind particles pairs. The size of the simulation box was chosen to be (105, 55, 55) Re, loaded with solar wind macro-electron--macro-ion pairs $5x10^5$. The aim of this test is to check the validity of the code and to build reference models to analyze more complicated cases with a variable incident solar wind. For that purpose, three simple test cases of slow, moderate, and fast solar wind velocities were studied and are presented respectively in section 3.2, 3.3 and 3.4. In Section 3.5, the code was effectively used to simulate the variability of the solar wind dynamic pressure, where a gap (air pocket effect) was generated in a planar manner along the streaming of the incident solar wind. Such pressure variations (depression) have never been considered in previous studies, though the occurrence of such events in nature should be common, such as hot flow anomalies (Sibeck et al., 1999). The plots in all sections in this chapter focus on x-z plane at y=27 Re, with more examples presented on the other x-y plane taken at z=28 Re and y-z plane taken at x=40 Re. The outcome of 3D modelling of simple test cases will enhance our understanding of the general problem of the Earth magnetosphere response to disturbances in the incident solar wind.

3.2 Application of a weak Solar wind drift velocity

3.2.1 Study in noon-midnight plane

We start with the first case where a zero dynamic pressure (i.e., Vsw =0.0) of the incident solar wind flow is applied. Initially, the geomagnetic field is set to zero and the box is filled with pairs of macro-ions/macro-electrons so that a plasma density of $0.8/\Delta^3$ is obtained. Inside the box, the particles have a bulk velocity of *0.25* in addition to the thermal component that corresponds to each species. As the incident solar wind bulk flow is set to zero outside the box, obviously no more particles feed the simulation box unless by thermal motion. The Earth's magnetosphere in the noon-midnight plane (x-z plane at y = 27 Δ) is shown in Figure 1. The plasma density is given in panels A and B, and their corresponding fields in panels C and D, respectively, at 100 Δt and 1000 Δt. The initial density of $0.8/\Delta^3$ is a statistical average which is consistent with larger peak density values as indicated by the color bar. First, we note the symmetry between day- and night-sides in the plasma density configuration around the planet. It is significant that the code recovers the dipole nature of the planetary field with little effect from the initial plasma dynamic pressure inside the simulation box (Figure 1(C)). In Figure 1(B), taken at 1000 Δt, the magnetosphere structure clearly appears despite the absence of external plasma sources and the continuing loss of particles from the box. For the sake of clarity, we recall that our initial conditions are such that the simulation box was initially filled with pairs of electron-ions that have a bulk velocity of 0.25, but no new incident solar wind particles are injected in the box. As a consequence, the system is loosing particles with time and this explains the magnetospheric structure obtained in Figure 1B. In addition, we notice a clear entering of plasma from the polar cusp and repopulation of the equatorial plasmasheet at the night side.

In Figure 1(C), we notice the symmetry of the field lines around the planet, though the system is still in an evolution phase. Figure 1(D) shows that the field lines are slightly elongated tailward and

mimic the plasma distribution shown in Figure 1(B). The topology of these field lines resembles a dipole-like shape, though a bit squeezed on the dayside and elongated at the nightside. To some extent, the results so far obtained with this first test confirm the power of the PIC code and legitimize the use of the macro-particle model to describe the magnetospheric structure on large scales.

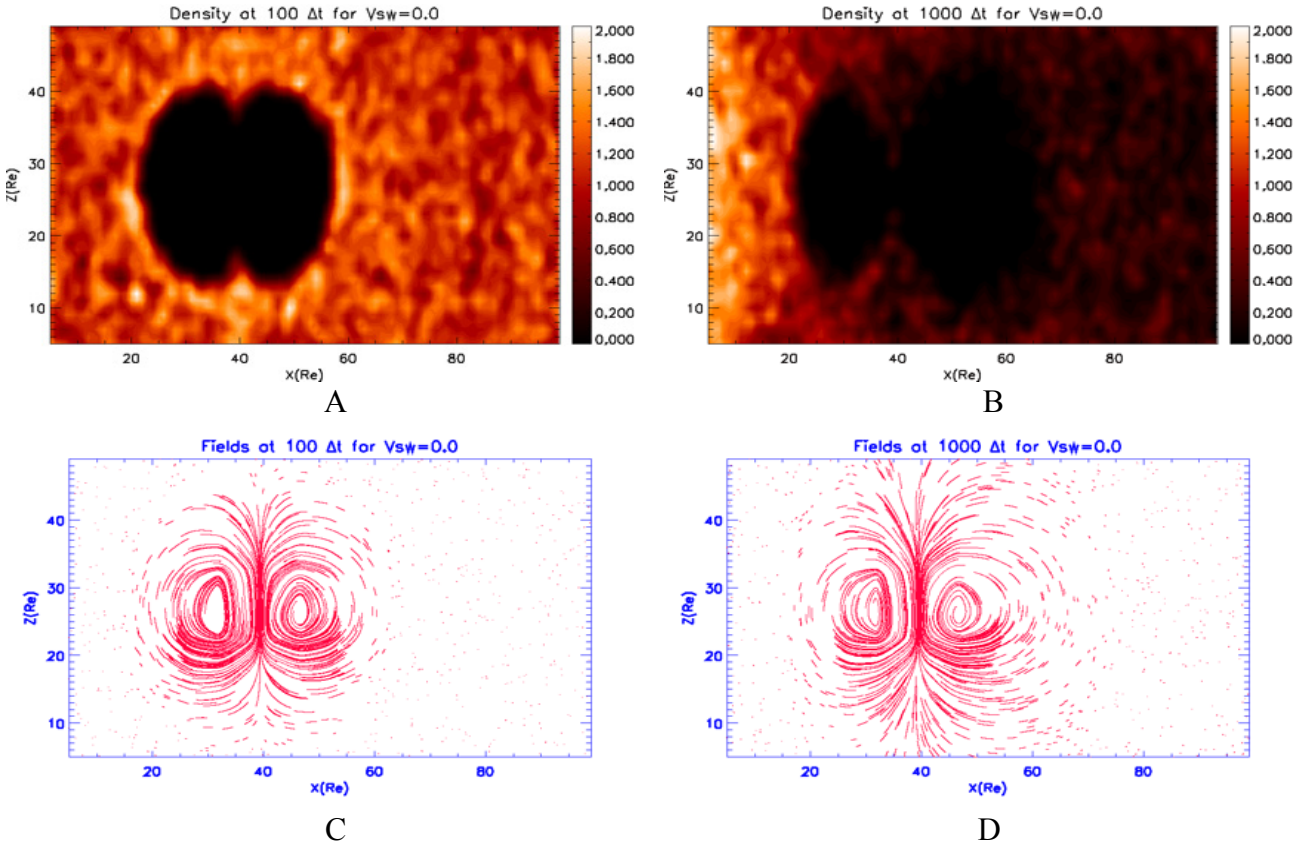

Figure 3.1. Earth's magnetosphere formation inside a box filled by e-ion pairs that have a bulk velocity of 0.25. Solar Wind particles incident on the left side of the box have their bulk velocity Vsw=0.0. The above plots are in the X-Z plane located at Y= 27 Re. Plasma distribution is shown in panels A and B, taken at 100 and 1000 Δt, respectively. The corresponding field topology is shown in panels C and D, taken at 100 and 1000 Δt, respectively

3.2.2 Other examples in dawn-dusk and south-north directions

To extend checking the ability of the code to simulate 3D plasma distribution and fields' topology, we present other examples on dawn-dusk and south-north directions. In dawn-dusk directions (x-y plane at z=28Re), our results are shown in figure 3.2. Plasma densities are presented in panels A and B, their fields' topologies are presented in panels C and D respectively, at 100 and 1000 Δt. The symmetry obtained in figure 3.1(A) is now seen as a circular shape in figure 3.2(A) for the dawn-dusk direction at 100 Δt. In figure 3.2(B) taken at 1000 Δt, we see the magnetospheric structure is established, despite the continuing escape of particles and the absence of the external source of the plasma injection. In figure 3.2(C) the planetary field lines are almost symmetric, though the system is still in evolution state. Figure 3.2(D), the field lines are seen slightly compressed at the dayside, whilst elongated at the nightside.

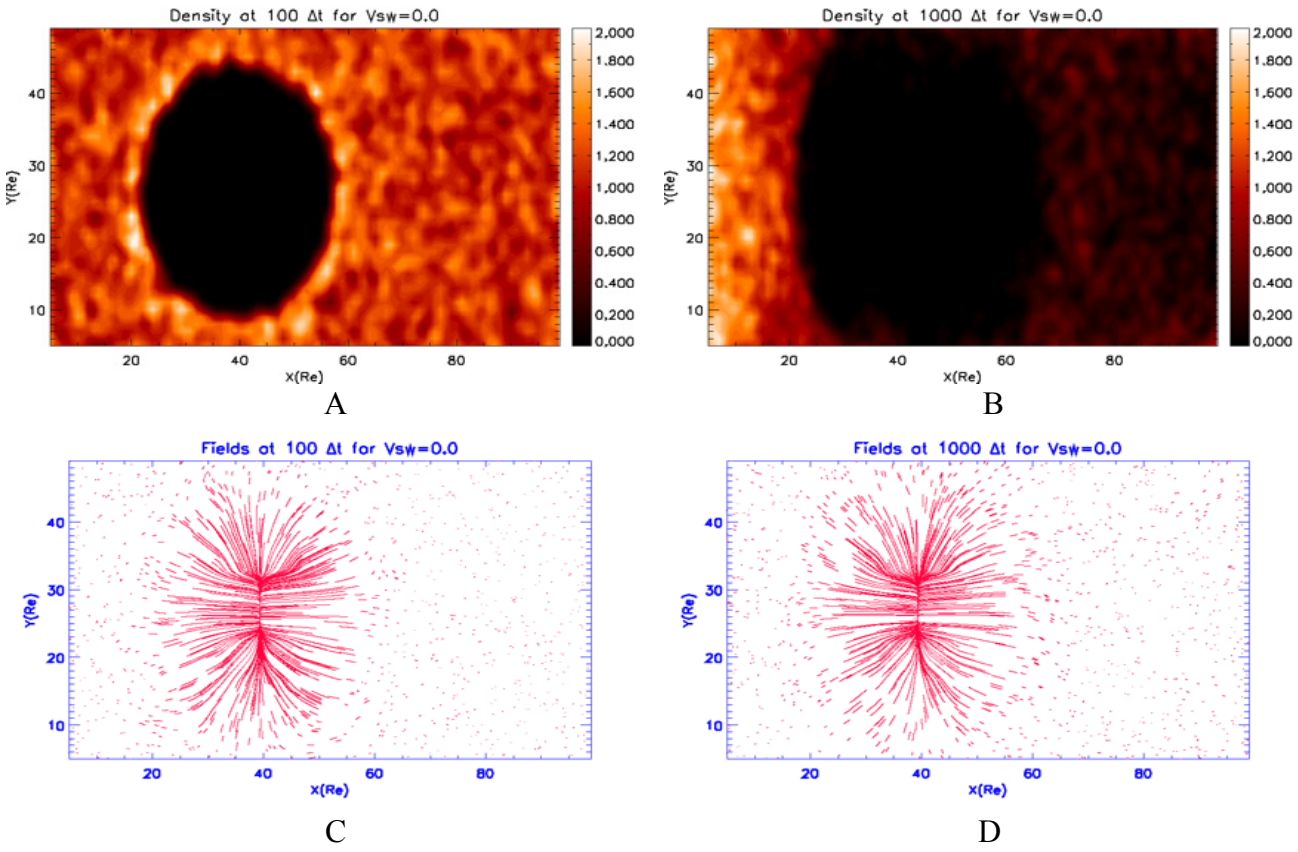

Figure 3.2. Earth's magnetosphere formation inside a box filled by e-ion pairs that have a bulk velocity of 0.25. Solar Wind particles incident on the left side of the box have their bulk velocity Vsw=0.0. The above plots are in the X-Y plane located at Z= 28 Re. Plasma distribution is shown in panels A and B, taken at 100 and 1000 Δt, respectively. The corresponding field topology is shown in panels C and D, taken at 100 and 1000 Δt, respectively

In figure 3.3, the plasma and fields' are shown in y-z plane at x=40Re. In figure 3.3(A) the plasma density is seen distributed symmetrically around the planet at both dawn and dusk direction. Both cusps are seen at z=19 and 36 Re below and above the planet position. The dipole magnetic pressure at this early stage pushes the plasma away around the planet, which by turn can be observed denser around the boundary of the magnetospheric cavity. The corresponding field topology is shown in figure 3.3(C). In figure 3.3(B) taken at 1000 Δt, there is a clear asymmetry which resemble that of the figure 3.1(B), which is due to the thermal motion of the existing particles, in addition there is solar wind escape

without any new injection. In figure 3.3(D), the field lines flare out more in the positive y direction. This flare out of the field denotes the asymmetry of the plasma shown in figure 3.3(B).

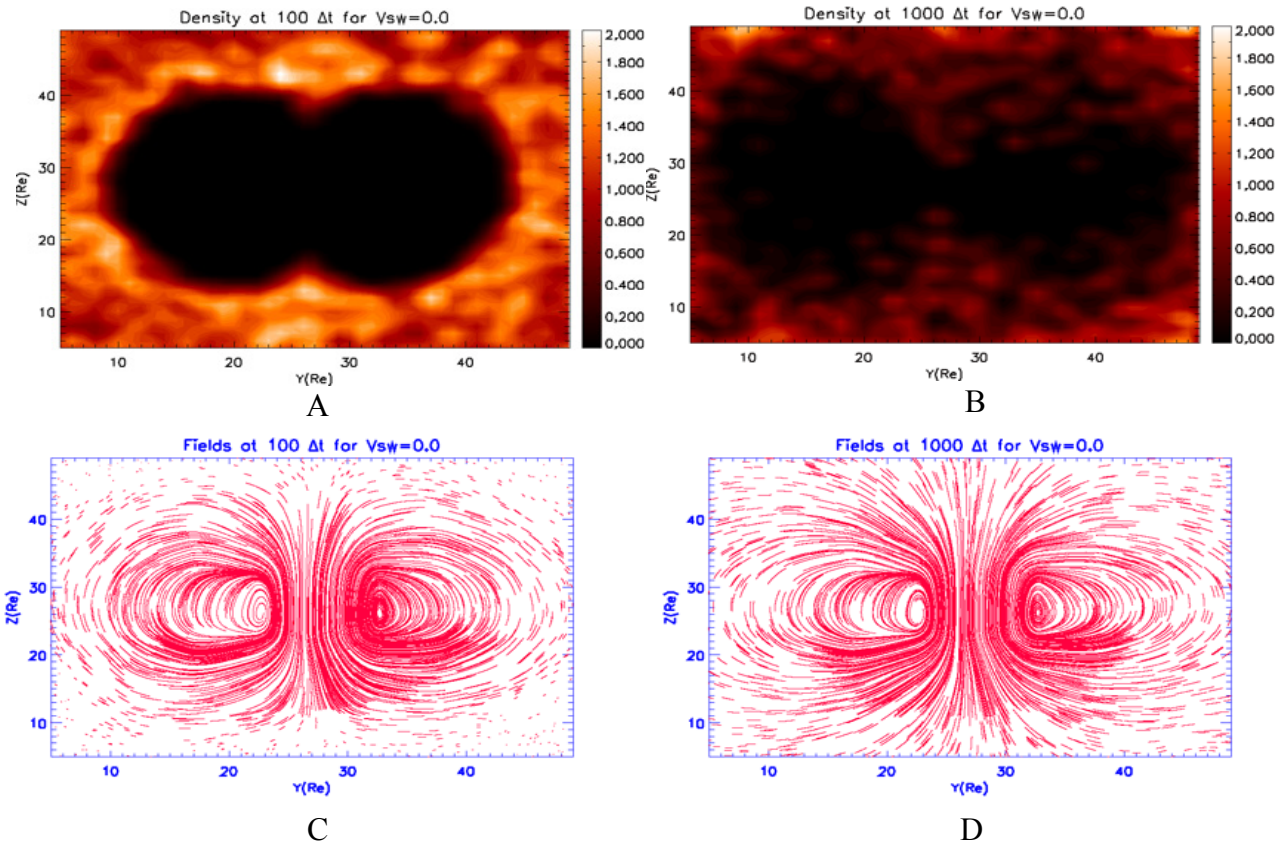

Figure 3.3. Earth's magnetosphere formation inside a box filled by e-ion pairs that have a bulk velocity of 0.25. Solar Wind particles incident on the left side of the box have their bulk velocity Vsw=0.0. The above plots are in the Y-Z plane located at X= 40 Re. Plasma distribution is shown in panels A and B, taken at 100 and 1000 Δt, respectively. The corresponding field topology is shown in panels C and D, taken at 100 and 1000 Δt, respectively

3.3 Application of moderate Solar wind drift velocity

3.3.1 Study in noon-midnight direction

In the following step, the incident solar wind drift velocity (Vsw) is increased to a moderate value of 0.1, while keeping the box initially filled with particles that have a bulk velocity of 0.25. Figure 3.4 contains four panels: A and B show the density distribution at 100 and 1000 Δt, respectively, and panels C and D show the fields at the same time periods. In Figure 3.4(A), at an early stage of the interaction taken at 100 Δt, a clear modification has taken place in the configuration of the magnetosphere symmetry as compared to the results obtained in the previous step with Vsw =0.0. The compression of the magnetopause at the dayside is accompanied by a relaxation on the nightside.

Figure 3.4(B) clearly reveals a significantly compressed magnetopause nose, with the cusps—two thick, finger-like plasma—entering into the Earth's magnetosphere from both poles. The nightside plasma configuration is quite stretched and elongated. From 80 to 100 Re along the x-axis, the formation of blobs of plasma in the equatorial plane (at z = 53 Re) and along the neutral line is clearly seen. In Figure 3.4(C), taken at 100 Δt, the field lines show the modification of the system due to the increased ram pressure of the incident solar wind, particularly on the dayside. Figure 3.4(D), taken at 1000 Δt shows how the dayside field lines are compressed inward, whilst on the nightside, the field lines are stretched away and straightened tailward, much like the plasma distribution. Field lines clearly flare out at the early nightside, and the cusps are clearly seen in the field topology.

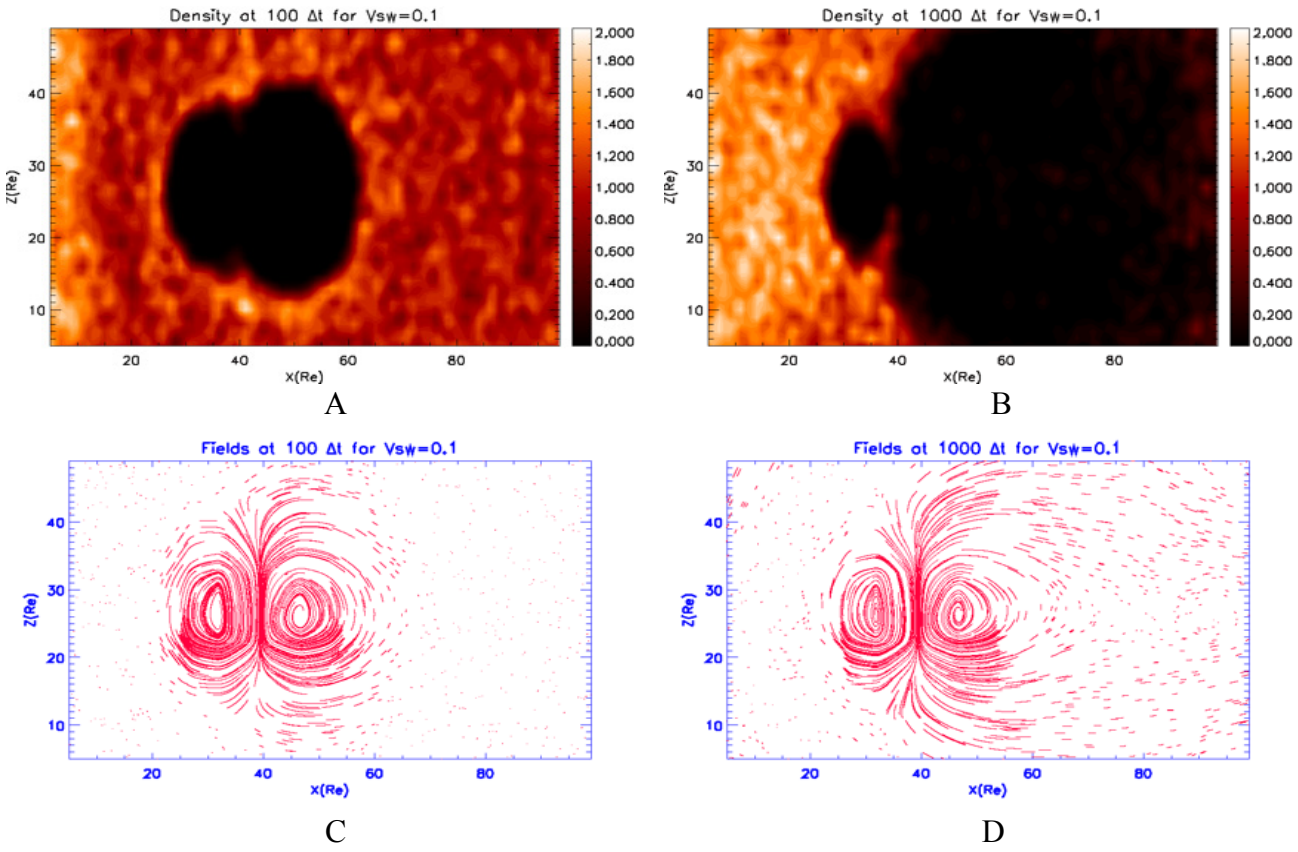

Figure 3.4. Earth's magnetosphere formation inside a box filled by e-ion pairs that have a bulk velocity of 0.25. Solar Wind particles incident on the left side of the box have their bulk velocity Vsw=0.1. The above plots are in the x-z plane located at y= 27 Re. Plasma distribution is shown in panels A and B, taken at 100 and 1000 Δt, respectively. The corresponding field topology is shown in panels C and D, taken at 100 and 1000 Δt, respectively

3.3.1 Other examples in dawn-dusk and south-north directions

Now we continue with the second case where the dynamic pressure is increased to a moderate value (Vsw=0.1) to study the Earth's magnetosphere in the equatorial plane (x-y plane at y = 28 Δ) as shown in Figure 3.5. In figure 3.5(A) the plasma density distribution in the equatorial plane has a circular shape at this early time of 100 Δt, and the field topology of this configuration is shown in figure 3.5(C). In figure 3.5(B), the plasma distribution in the dayside is seen as a large arc boundary along y-direction, whilst at the night side random blobs of plasma are seen in the magnetospheric cavity,

extending along the x-direction out to 99 Re. It seems the configuration of the magnetopause is in favor of the dipole field against the relatively week dynamic pressure, therefore this unbalanced shield out plasma in the dayside and push away the plasma in the nightside. In figure 3.5(D) the field topology is seen stretched out slightly nightward and compressed at the dayside.

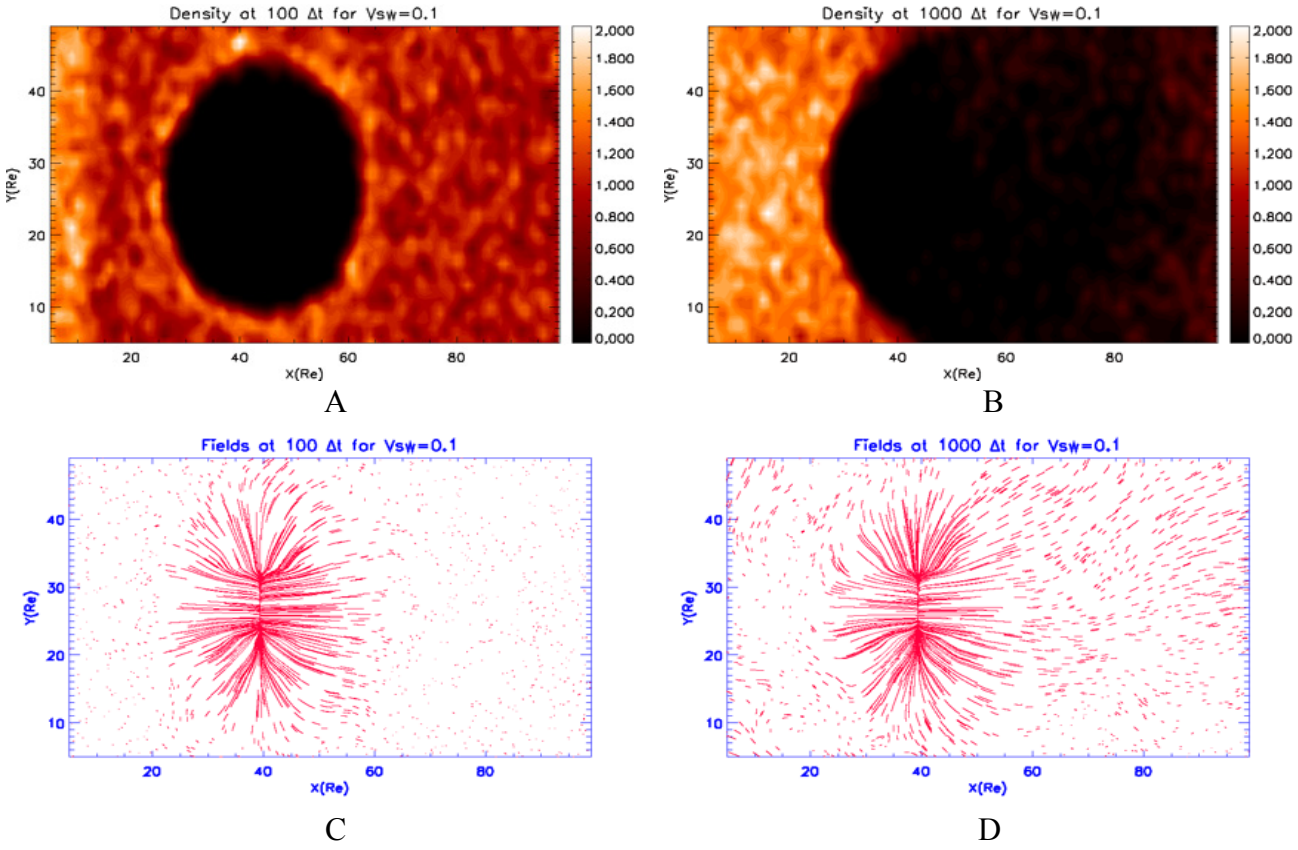

Figure 3.5. Earth's magnetosphere formation inside a box filled by e-ion pairs that have a bulk velocity of 0.25. Solar Wind particles incident on the left side of the box have their bulk velocity Vsw=0.1. The above plots are in the X-Y plane located at Z= 28 Re. Plasma distribution is shown in panels A and B, taken at 100 and 1000 Δt, respectively. The corresponding field topology is shown in panels C and D, taken at 100 and 1000 Δt, respectively

In the same manner, we see in figure 3.6(A) taken at 100 Δt, that the plasma distribution in the y-z direction is impinged toward the planet, the magnetospheric cavity being more confined as compared to that in figure 3.3(A). The size of the magnetospheric cavity contracted in favor of the applied dynamic pressure against the dipole pressure. The northern cusp is shown at 39 Re along z direction and the

southern cusp is seen at 18 Re along z-direction. The corresponding field's lines topology shown in figure 3.6(C), a typical dipole field's lines configuration which are closed at both dawn and dusk direction is seen. Whilst the case in figure 3.6(B) taken at 1000Δt, is different where the elapsed time was long enough for the interaction between the implied dynamic pressure and the dipole field. The two fingers-like shape that appear respectively at (y,z)=(22,14) and (31, 39)Re are the cusps that appear in the same position in Figure 3.4(C). The northern cusp is driven nightside and oriented toward dawn direction, while the southern cusp is driven nightside and oriented toward dusk direction. Figure 3.6(D) shows that the field's lines are flared out at the nightside and confined at the dayside.

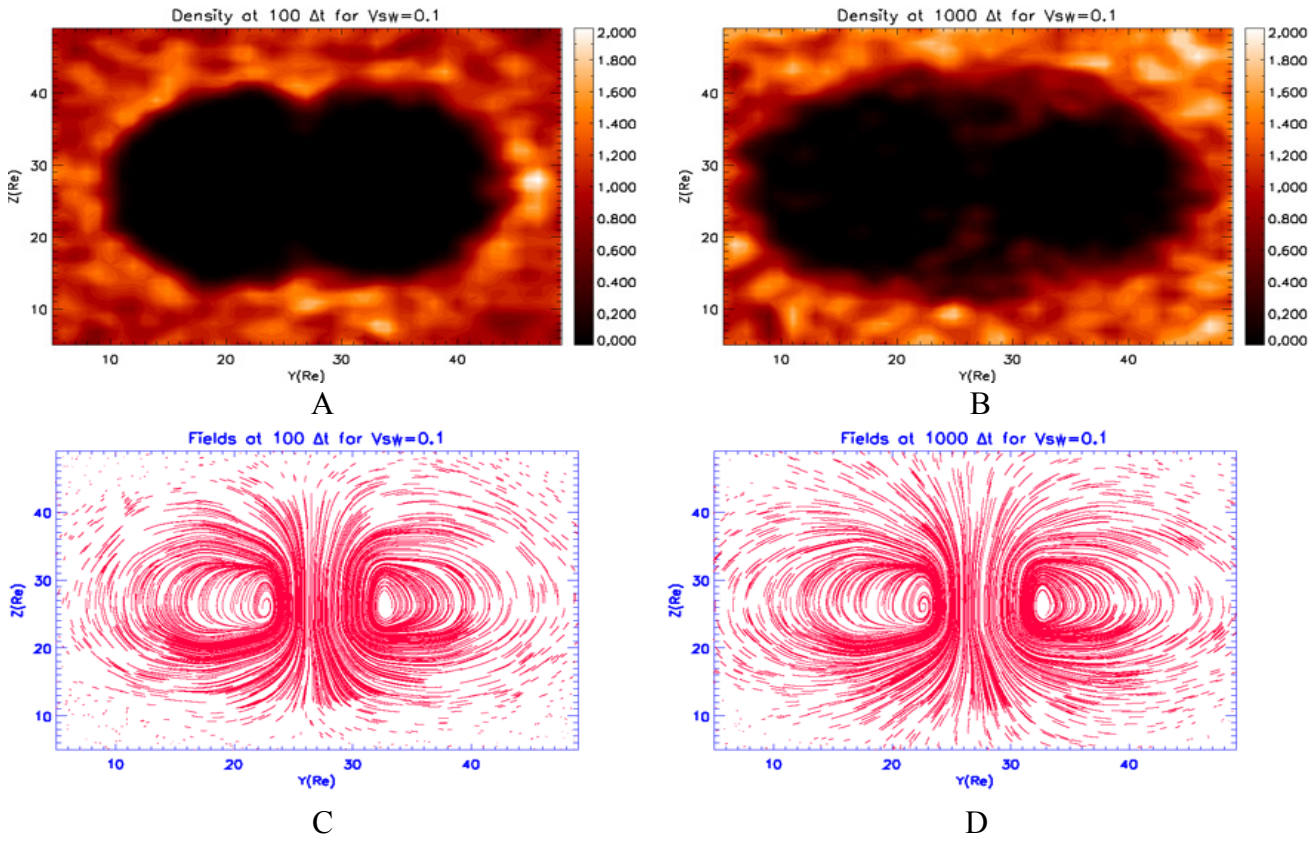

Figure 3.6. Earth's magnetosphere formation inside a box filled by e-ion pairs that have a bulk velocity of 0.25. Solar Wind particles incident on the left side of the box have their bulk velocity Vsw=0.1. The above plots are in the X-Y plane located at Z= 28 Re. Plasma distribution is shown in panels A and B, taken at 100 and 1000 Δt, respectively. The corresponding field topology is shown in panels C and D, taken at 100 and 1000 Δt, respectively

3.4 Application of strong Solar wind drift velocity

3.4.1 Study in noon-midnight directions

To refine our testing of the code, the solar wind drift velocity is now modified to a stronger value of 0.25. As in the previous cases, in Figure 3.7, panels A and B show the density distribution at 100 Δt (~300 sec) and 1000 Δt (~3000 sec), respectively, whilst panels C and D show their corresponding fields distribution. In Figure 3.7(A) the magnetospheric cavity is not yet established (compare to Figure 3.7(B)), with a noticeable compression on the dayside because of the increase in the ram pressure of the incoming solar wind. Also, the polar cusps are clearly seen. In Figure 3.7(C), the field topology, corresponding to the plasma distribution shown in panel A, reveals the compression of the field lines at the nose. At approximately 67 Re on the nightside, opened field lines are clearly seen with the beginning of the tail formation.

Figure 3.7(B) reveals that the so-called trapping region around the equatorial plane now seems thicker (thickness ~5.3Re). The plasma sources in that region are expected from both the cusps and the plasma driven from the nightside through the neutral line. We soon observe a clear formation of dense plasma clouds at around 80-99 Re, with more clouds seen around the equatorial plane. We mean by plasma clouds that low density random-shape ensembles of plasma blobs. Figure 3.7(D) shows the field line topology corresponding to the plasma in panel B. On the nightside, field lines are straightened and stretched out tailward. At around 73Re, we see an X point. On the former right-hand side, the field lines form a vortex-like structure, centered at the point (x, z) = (88, 20)R_e, a structure that corresponds to the plasma spherical clouds that were seen on the tail side in panel B. It is interesting to note that the equatorial plasmasheet is well developed and has a variable thickness that may reach a few Re.

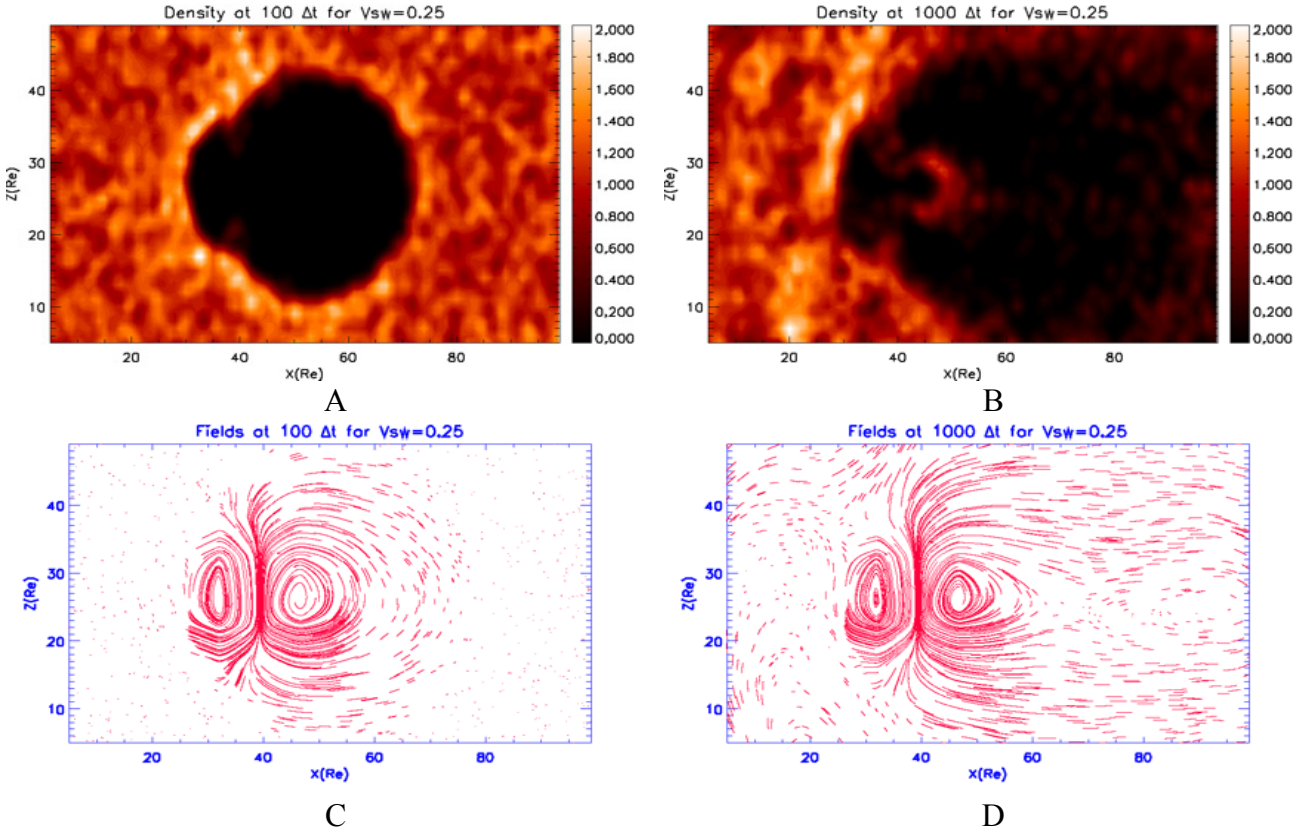

Figure 3.7. Earth's magnetosphere formation inside a box filled by e-ion pairs that have a bulk velocity of 0.25. Solar Wind particles incident on the left side of the box have their bulk velocity Vsw=0.25. The above plots are in the x-z plane located at y= 27 Re. Plasma distribution is shown in panels A and B, taken at 100 and 1000 Δt, respectively. The corresponding field topology is shown in panels C and D, taken at 100 and 1000 Δt, respectively

3.4.2 Other examples in dawn-dusk and south-north directions

To complete our view of the magnetosphere structure that results from the application of a stronger solar wind drift velocity incident onto the system, we found useful to show the corresponding behavior on plasma and field distributions in dawn-dusk and south-north planes. This will enable us to track globally the output of this study in 3D. Hence, for the dawn-dusk plane, we show in Figure 3.8, panels A and B the density distribution at 100 Δt and 1000 Δt, respectively, whilst panels C and D show their corresponding fields distribution. In figure 3.8(A) at 100 Δt, the plasma distribution show a circular shape with tiny density crests implanted inside, duskside of the circular shape in x-y plane. The field

representation of this plasma is shown in figure 3.8(C), where the field lines show an early trace of the formation of the magnetotail. In figure 3.8(B) taken at 1000 Δt, the trapping region around the equatorial plane has a thickness of ~6Re. More plasma filling in the nightside cavity is observed, with a denser distribution toward dusk side (at z=35-45 Re). Figure 3.8(D) show the field topology of the plasma distribution in figure 3.8(B), where the field's lines stretched out tailward to map the classical shape of the magnetotail in x-y plane. Note however that in the former region, the field's lines are driven dusk side (look at the field topology from x=66 Re and beyond). At the magnetopause the field's lines are compressed along x direction.

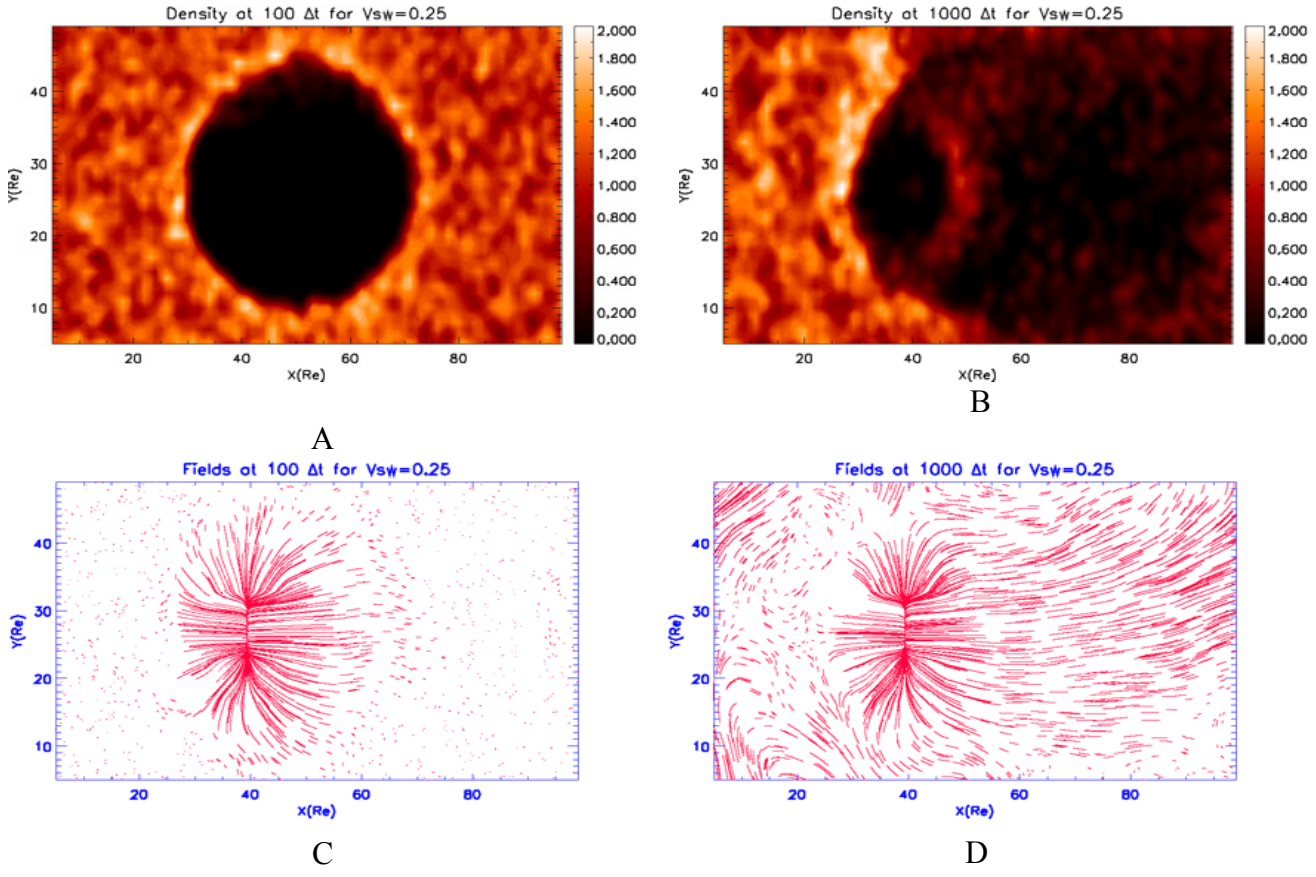

Figure 3.8. Earth's magnetosphere formation inside a box filled by e-ion pairs that have a bulk velocity of 0.25. Solar Wind particles incident on the left side of the box have their bulk velocity Vsw=0.25. The above plots are in the X-Y plane located at Z= 28 Re. Plasma distribution is shown in panels A and B, taken at 100 and 1000 Δt, respectively. The corresponding field topology is shown in panels C and D, taken at 100 and 1000 Δt, respectively

The next interesting section of the 3D system that is commonly studied is of the y-z plane (here taken at x=40Re). For the same case of a strong solar wind drift velocity (Vsw=0.25), we show in Figure 3.9 the density distribution at 100 Δt and 1000 Δt, respectively in panels A and B, whilst panels C and D show their corresponding fields distribution. In Figure 3.9(A), it is clearly seen that the northern and southern cusps are dawn-oriented this time. The effect of applying a stronger dynamic pressure can easily tracked by comparing Figures 3.3(A), 3.6(A) and 3.9(A) where the sequential configuration implies that the stronger the dynamic pressure the more confined the magnetospheric cavity as seen in figure 3.9(A). Two finger-like shaped plasmas are observed at (y, z)= (38,32 and 39,26)Re. In Figure 3.9(C) the field's lines topology start opening at y=11 Re and y=45 Re, they are flared out in the dawn side of the planet and more confined at the dusk side. In Figure 3.9(B), a clear modification for the plasma distribution is apparently developed due to the increase of the dynamic pressure that implied for 1000Δt on the system. The cusps are connected to the trapped region around the planet in both dawn and dusk directions, and one can see that along the y direction the trapped regions have an average thickness of approximately ~7 Re. The cavity size is also confined at the dusk side and more relaxed in the dawn side.

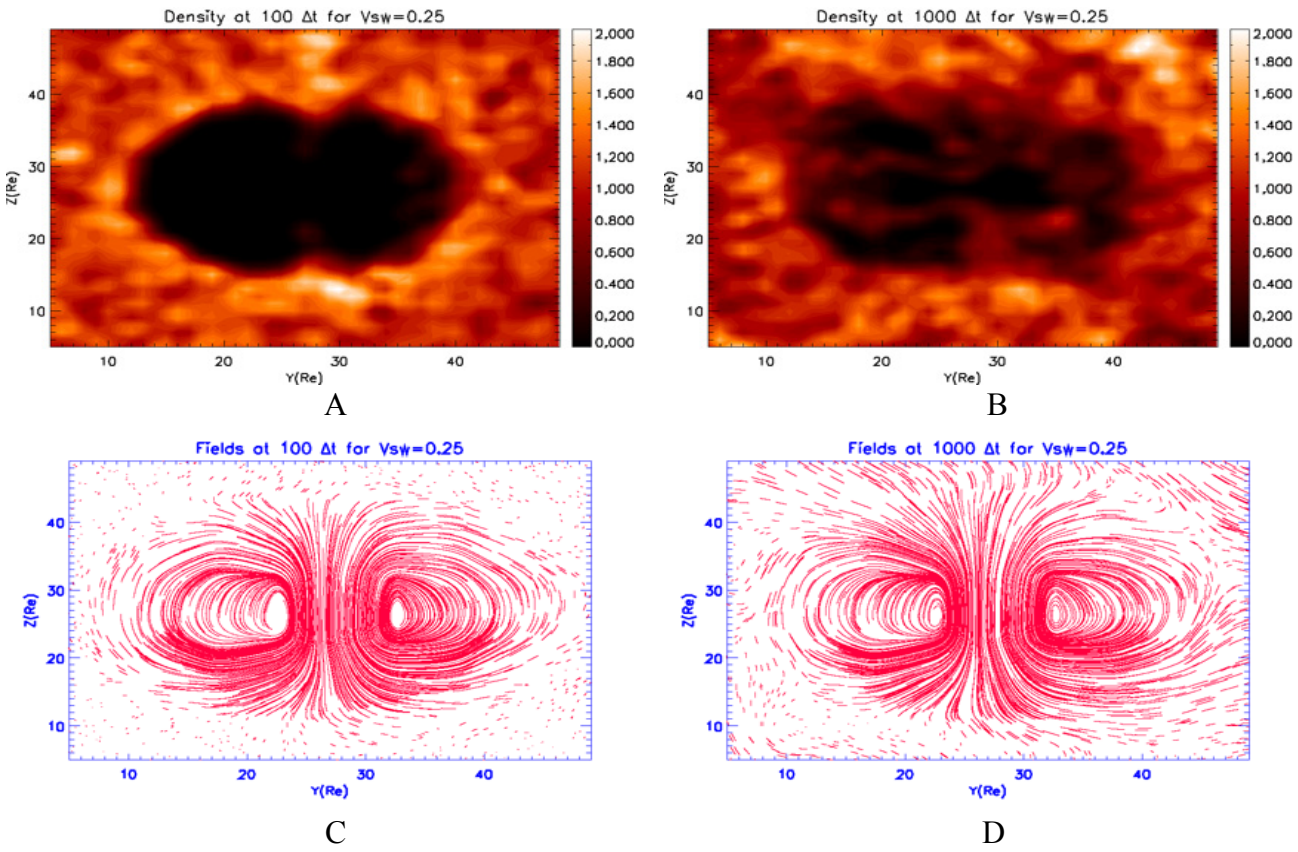

Figure 3.9. Earth's magnetosphere formation inside a box filled by e-ion pairs that have a bulk velocity of 0.25. Solar Wind particles incident on the left side of the box have their bulk velocity Vsw=0.25. The above plots are in the Y-Z plane located at X= 40 Re. Plasma distribution is shown in panels A and B, taken at 100 and 1000 Δt, respectively. The corresponding field topology is shown in panels C and D, taken at 100 and 1000 Δt, respectively

3.5 Application of a depression in the solar wind flow (air pocket effect)

After analyzing these cases, we conclude that our PIC code recovers what is known about the large structure of the Earth's magnetosphere for all regimes of solar wind ram pressure. Hence, the next set of tests for our code is designed to check its capacity to simulate the time variability of the magnetosphere on selected time scales. For example, one of the most manifest natures of solar wind is its dynamic pressure variability, which we choose to simulate. Depression/compression of the solar

wind is simulated by applying abrupt changes to the speed of the steady flow of the solar wind particles inside the simulation box

Shown in Figure 3.10**,** in the noon-midnight plane, is a steady flow with a bulk velocity of 0.25 of solar wind particles that have been injected into the simulation box. The process enables the system to evolve up to 400 Δt, thereby allowing enough time to establish the classical macrostructure of the Earth's magnetosphere. Next, the solar wind bulk velocity is reduced to 0.1 for 100 Δt between 400 and 500 Δt. At 500 Δt, Vsw is again increased to its initial value of 0.25, and the process continues until 1000 Δt. As a result, a gap is generated in the incident plasma structure that can be defined by the drop in both the bulk velocity and the plasma density along the x-axis. This structure results in response to the sudden drop in plasma dynamic pressure. In Figure 3.10, the upstream boundary of the formed gap is around 13 Re and moves with the initial steady state speed of 0.25, whilst the one downstream is around 28 Re (indicated by the two vertical bars in figure 3.10). As shown, the gap has a width of approximately 15 Re, which is consistent with the picture of a differential speed applied during 100 Δt—e.g., (0.25-0.1)*100= 15Re. Our code, then, is capable of reproducing pulse events in the solar wind properties and following them with time whilst measuring their impact on the magnetosphere. In the next chapters, the code will be used to simulate the impact of the disturbances of the incident solar wind on the Earth magnetosphere.

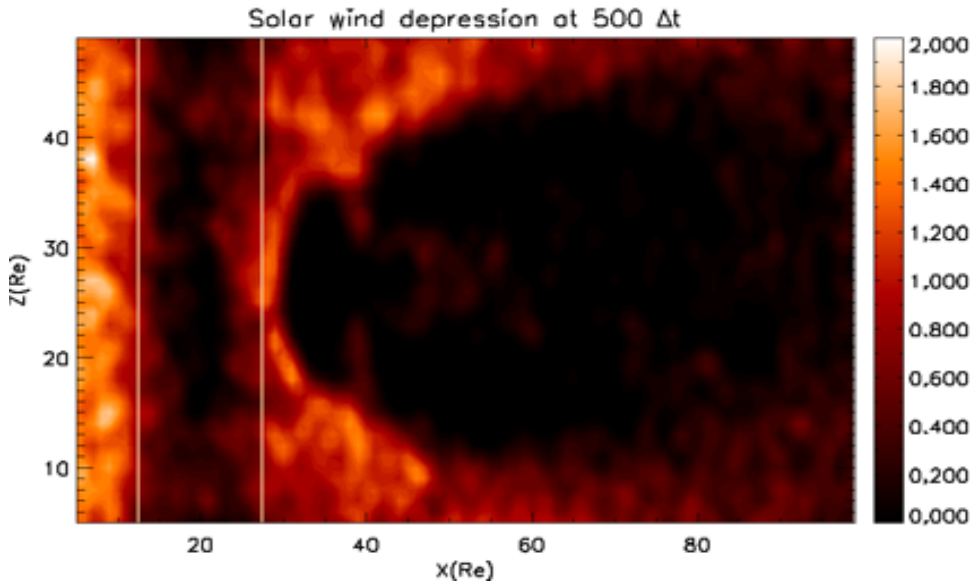

Figure 3.10. Gap generation due to a depression in the Solar Wind flow during its interaction with Earth's magnetosphere at 500 Δt, plotted in x-z plane located at y= 27 Re. At the selected step time, the gap is centered at x~20Re and indicated by the two vertical bars along the x-axis and has a width of ~15Re.

3.6 **Conclusions**

The code described in chapter 2, has been tested on three different levels of the solar wind bulk velocities (slow, moderate, and strong). We showed how the dynamic pressure directly influences the shaping up of the Earth magnetosphere as it can be seen in Figures 3.1 up to 3.9. We have also shown the importance to study the interaction process in different planes, as the example of Figures 3.4(B) and 3.6(B) that describe the plasma during a moderate solar wind bulk velocity. Indeed, in that case, the cusps were shown nightside oriented in 3.4(B) (taken in x-z plane), however when looking at their coordinates in the y-z plane, we saw that the northern cusp is dawn oriented, while the southern cusp is dusk oriented. Then we can conclude that the cusps are nightside oriented, but oppositely diverted along y-direction. In the same way, for strong solar wind velocity, we found the plasma tail is dusk oriented, a result that could not be seen from the only noon-midnight section. A 3D investigation of the magnetospheric topology is then sometimes required to handle the full set of processes acting on the system.

Chapter Four

The Impact of Solar Wind Depression (Air Pocket Effect) on the Dayside Magnetopause in the Absence of the Interplanetary Magnetic Field.

4.1 Introduction

In this chapter, the impact of a depression in the solar wind on the dayside magnetopause during the absence of the interplanetary magnetic field (IMF) will be studied using the PIC electromagnetic code that has been described in chapter 2 and tested in chapter 3. In a first step, we will discuss the strategy of the simulation of the interaction between the solar wind and the Earth magnetosphere. Indeed, the absence of IMF was chosen on purpose as a first case in a sequential study where further orientations of the IMF will be selected. For example as we will see in chapter five the IMF will be included as a steady flow southward and in chapter six, the study will discuss the interaction when the IMF is oriented northward. The dynamic pressure of the solar wind and the Earth magnetosphere magnetic pressure will play the basic controlling elements in the interaction process. Four time spans were chosen as a common duration of time for all cases which are 1001, 1100 and 1175 and 1250 Δt. The plasma density distribution will be discussed in 3D in Figures 4.1, 4.2 and 4.3. The field's lines topologies will be discussed in 3D in Figures 4.4, 4.5 and 4.6. Section 4.2 and 4.3 will be devoted to the description of the plasma distribution in noon-midnight plane, dawn-dusk plane and south-north plane respectively. Section 4.4 and 4.5 will be devoted to the description of fields' topologies in noon-midnight plane, dawn-dusk plane and south-north plane respectively. In section 4.6, analysis and comments are presented to discuss the results obtained so for, particularly with Figure 4.7, which will describe the magnetopause expansion/recovery in 3D, and Figure 4.8 which will show the detachment

of plasma blobs due the depression of the solar wind in different time span. In section 4.7, some of the results will be briefly summarized.

4.2 Plasma distribution at different time span in the noon-midnight plane

As described in chapter 3, to simulate the interaction between a depression in the solar flow and the magnetosphere, we first obtain a steady state after allowing the system to evolve until step time 900 Δt under the influence of a solar wind bulk velocity Vsw of 0.25 but no IMF is applied. We then reduce Vsw from 0.25 to 0.1 and, accordingly, the ram pressure drops by 60% during 100 Δt before the latter is restored to its initial value. Consequently, moving gap forms, as shown in Figure 5.1(A) at time step 1001 Δt when its position was between 12Re and 27Re along the Sun-Earth line. Clouds of plasma from the tail fill the formed cavity and feed the equatorial plane with a plasmasheet that has a variable thickness. The plasmasheet mentioned here is a planar plasma distribution along the neutral line that can be seen between (x,z)=(80,45)Re and (120,50)Re. The cusps are clearly visible. As expected, the particles entering the cusp bounce back and forth due to the exchange of the parallel plasma velocities for the perpendicular velocities, thereby producing the magnetic mirror effect as evidenced by following the particles' motion with time in that region.

In Figure 5.1(B), taken at 1100 Δt, the downstream boundary of the generated gap reaches the dayside magnetopause. At that time, the expansion of the magnetopause apparently extends to 13.5 Re along x-axis. Within the gap, light clouds of plasma of random distribution are seen, some of which reverse direction toward the Sun. On the tail side, a stream of plasmasheet replenishes the space along the neutral line. Figure 5.1(C) reveals a new situation where the magnetopause surface (nose), after an expansion period, breaks up within the gap. During the expansion phase, the stretched magnetopause appears as a thin, distorted layer that breaks up at a distance of approximately 15.5Re from Earth at

~1132 Δt. Soon afterward, the extended magnetopause boundary hits the upstream boundary of the gap area. Plasma clouds (blobs) are visible in the extended dayside cavity of the magnetosphere. The orientation of the cusps (seen as almost upright in this case) is highly affected by the travel of the solar wind depression inside the system. A relatively large plasma cloud is observed along the neutral line at about ~ 80Re tail side.

Figure 5.1(D) shows that after the solar wind gap boundaries pass over the dayside magnetopause, the latter restores its classical shape with a nose position at approximately 10Re from Earth. A thin ring of plasma corresponding to the noon-midnight section of the trapping region is formed around the planet. The size of this region reaches 6.6Re at the nightside equatorial plane. The shape and orientation of the cusps are highly susceptible to changes induced by the gap travelling through the system. At the early nightside, we notice that the magnetospheric structure flared out despite the fact that B_z=0. We believe that the lobes respond positively to the drop in the ram pressure when the gap approaches them, and as a result, they stretch out. Therefore, this flare-out is due to the drop in the solar wind pressure rather than the interplanetary magnetic field. At 100-145Re, lobes are parallel to the Sun-Earth line, with large plasma clouds formed around the equatorial line.

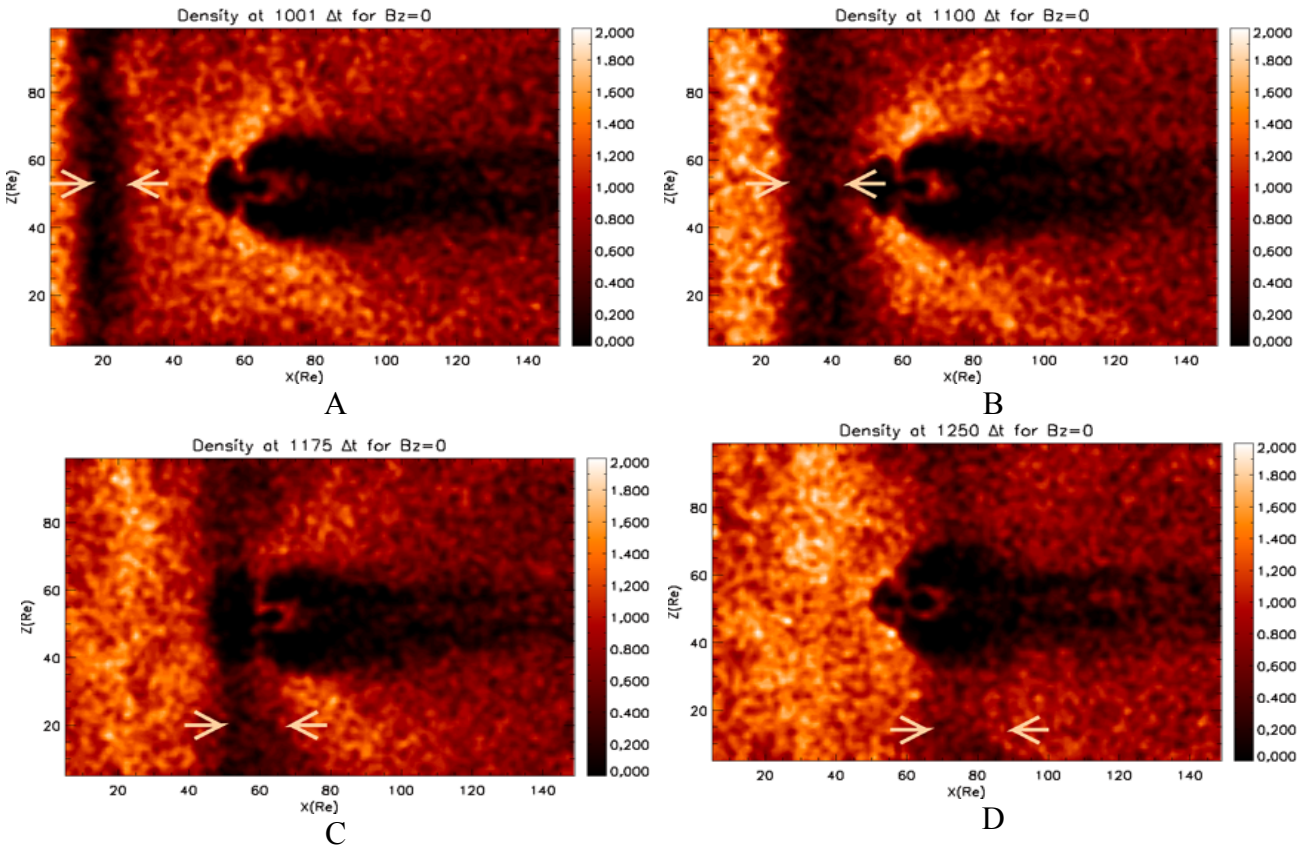

Figure 4.1. Time sequence of the response of Earth's magnetosphere to a depression (air pocket effect) in the incident Solar Wind flow for Bz=0. Plasma density is shown in panels A, B, C, and D, taken at 1001, 1100, 1175 and 1250 Δt, respectively. All plots are shown in the x-z plane located at y= 52Re and the gap position along x-direction is shown in figure between the two arrows heads.

4.3 Other examples of plasma distribution seen in different planes such as dawn-dusk and south-north directions.

To present a global view for the sensitivity of the Earth's magnetosphere to the variability of the solar wind dynamic pressure, we show in the following four images in dawn-dusk plane (x-y plane at z=53Re; equatorial plane) and other four images in south-north plane (y-z plane at x=60 Re of the Earth's position).

First, we discuss the dawn-dusk plasma density distribution. In Figure 4.2(A) taken at 1001 Δt, the generated gap is observed between ~12 and 27 Re along the x-direction. The plasma in the trapped region appears as a concave band along y-direction and has a thickness of ~5 Re. Clouds of plasma from the tail fill the formed cavity in the night side; the filling is denser toward the dusk side. In Figure 4.2(B) taken at 1100 Δt, the gap (air pocket) is advanced to a new position of its upstream edge at 27Re along x-direction. Clouds of plasma in the gap are seen clearly, some of which are observed moving against the stream. Later on, we will try to explain the mechanism that makes these tiny blobs of plasma to reverse directions. The trapped region (plasma band) around the planet along y is observed and has a relative thickness of 6.6Re. At this time of 1000 Δt, the magnetopause is thinning and approaches the downstream of the gap. In figure 4.2(C) taken at 1175 Δt, the expanding magnetopause is observed breaking up. The trapped region in the night side contracted in size to 4.3Re, while filling of plasma becomes denser and dusk oriented in terms of density. In figure 4.2(D) taken at 1250Δt, the solar wind gap boundaries pass over the dayside magnetopause, which restored its position immediately after the disturbance is over. The flare out of the northern and southern lobes is remarkably observed. This flare out is directly associated with the position of the gap (air pocket effect).

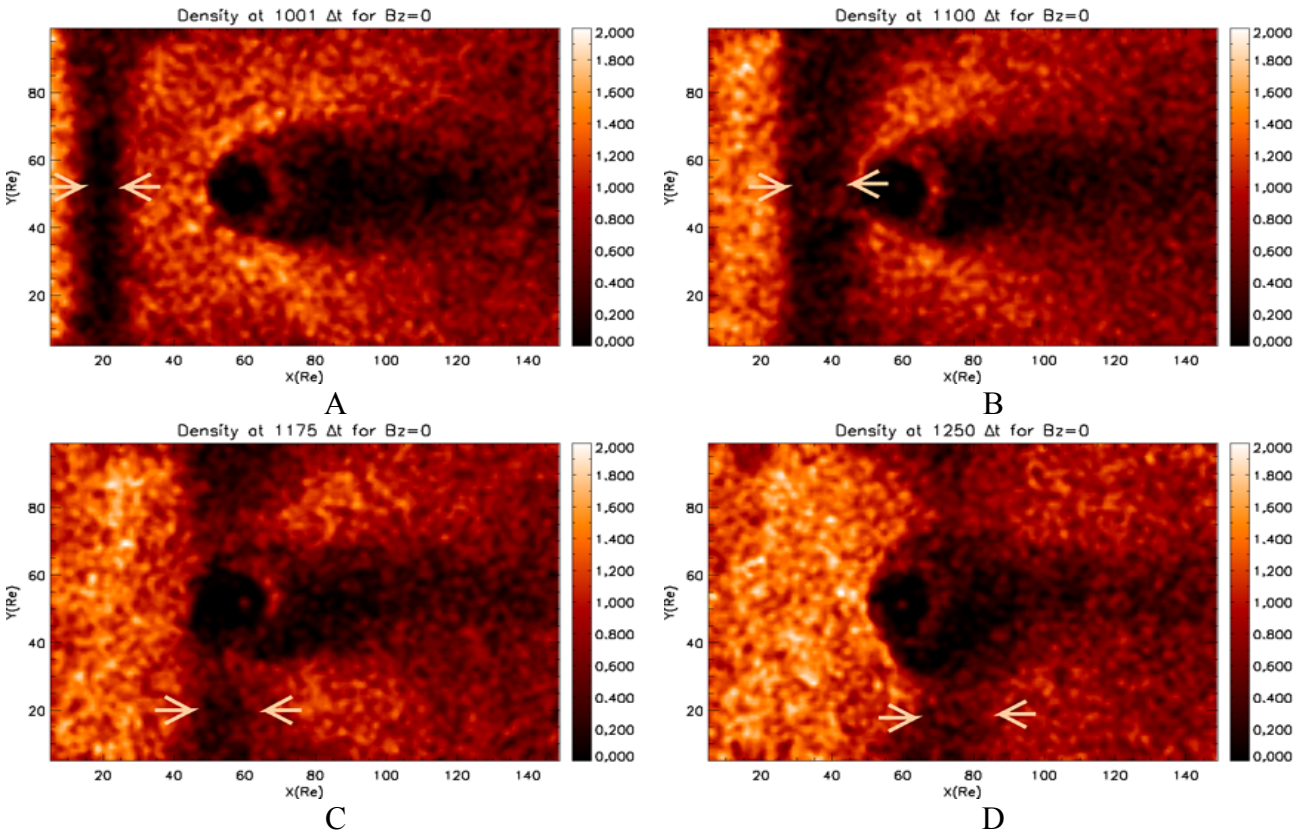

Figure 4.2. Time sequence of the response of Earth's magnetosphere to a depression (air pocket effect) in the incident Solar Wind flow for Bz=0. Plasma density is shown in panels A, B, C, and D, taken at 1001, 1100, 1175 and 1250 Δt, respectively. All plots are shown in the X-Y plane located at Z= 53Re and the gap position along x-direction is shown in figure between the two arrows heads

The plasma distribution (no IMF applied) is now presented in the second plane considered in our extended 3D study, namely the south–north plane (y-z at x=60Re). In Figure 4.3(A) taken at 1001 Δt, a doughnut shape of plasma, which has an average thickness of ~3.5Re is seen around the planet within the magnetospheric vicinity. Also, the cusps are seen linked to the doughnut at both north and south direction. In figure 4.3(B), the cusp is seen up right in the equatorial plane and pointing along the planet coordinate in z-direction. In figure 4.3(C), taken at 1175 Δt, the cavity shows slight expansion along y and z direction, the doughnut shape inside the magnetospheric cavity is squeezed along the planet position(y=52,z=53)Re. Some plasma blobs are observed along the y-direction from the dawn

side and connecting with the boundary of the doughnut shape. Both cusps are seen slightly declined toward dawn direction. Other plasma blobs are seen entering from the opposite direction (dusk) into the inner magnetosphere. At the left upper/lower side of the simulation, box a triangular shape of emptiness signifies that the boundary of the gap traveling along x is concave around the planet position and reaches its position along y-z plane from the dusk side. In Figure 4.3(D) taken at 1250Δt, as the solar wind gap passes over the dayside magnetopause, the northern and the southern cusps are inclined toward dawn (point sharply nightward in x-z plane), and connecting to the trapped region in the low latitude of 3±1Re. The gap boundary hits the simulation box boundary in the dusk side as seen at the upper/lower corners of the simulation box.

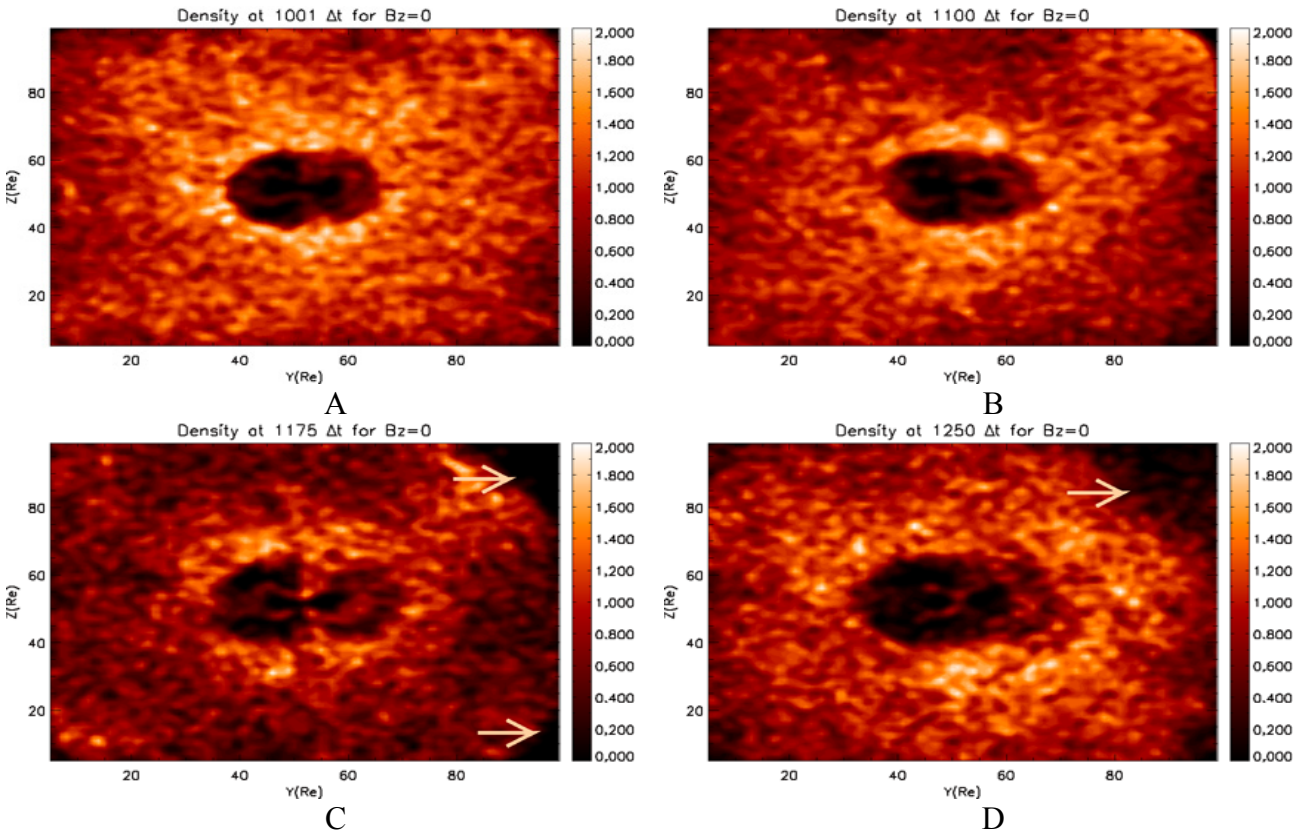

Figure 4.3. Time sequence of the response of Earth's magnetosphere to a depression (air pocket effect) in the incident Solar Wind flow for Bz=0. Plasma density is shown in panels A, B, C, and D, taken at 1001, 1100, 1175 and 1250 Δt, respectively. All plots are shown in the Y-Z plane located at X= 60Δ.

4.4 Field topologies at different time span in noon-midnight plane

In terms of field lines topology in the x-z plane, we see in Figure 4.4(A), taken at 1001 Δt, that the dayside magnetopause stands at around 10.3Re from Earth along the Earth-Sun line. The lobes are seen as approximately parallel to the Sun-Earth line because the gap effect is not yet felt by the nightside system. An X-point can be seen at 103Re. The configuration of the field lines at the tail side implies the existence of plasma concentrated in that region centered at the point (x, z) = (140, 47)Re as confirmed by Fig. 4.1A. In Figure 4.4(B), taken at 1100 Δt, the magnetopause nose is seen expanded up to 15Re from Earth. The lobes are clearly seen driven parallel to the neutral line. At around x =

140Re, a vortex-like configuration of the field lines denotes the plasma confined at that distance, as shown by Figure 4.1(B).

Figure 4.4(C), taken at 1175 Δt, illustrates how the field lines at the dayside magnetopause start breaking up at around 15.48Re from Earth (see figure 4.1(C)). Open field lines are clearly seen around this distance as it was the case for the plasma distribution shown in Figure 4.1(C). One also sees an X-point at 103Re (in fact, we monitored multiple X-points that will be discussed in the conclusion). Field lines configuration at the nightside up to 100Re have a wave shape, much like their corresponding plasma in that region. This configuration corresponds to the interaction between plasma seen at 80Re (e.g., Figure 4.4(C)) and the plasma traveling Earthward from the far tail. In Figure 4.4(D), taken at 1250 Δt, the magnetopause nose's position reads the value of 10.30Re from Earth: this means that it has been recovered after the depression effect is over. Field lines topology shows vortex-like (confined) structures that may be single or multiple along the neutral line (at x = 120Re, and 145Re for z = 53Re). For example, one may count up to four such vortex-like structures during the time evolution of the system. The gap position now is approximately between 65Re and 85Re along the x-axis (see Figure 4.1(D)), which results in stretching of the lobes and thus pulling the position of the X-point Earthward, now seen at (x, z) ~ (90, 53)Re .

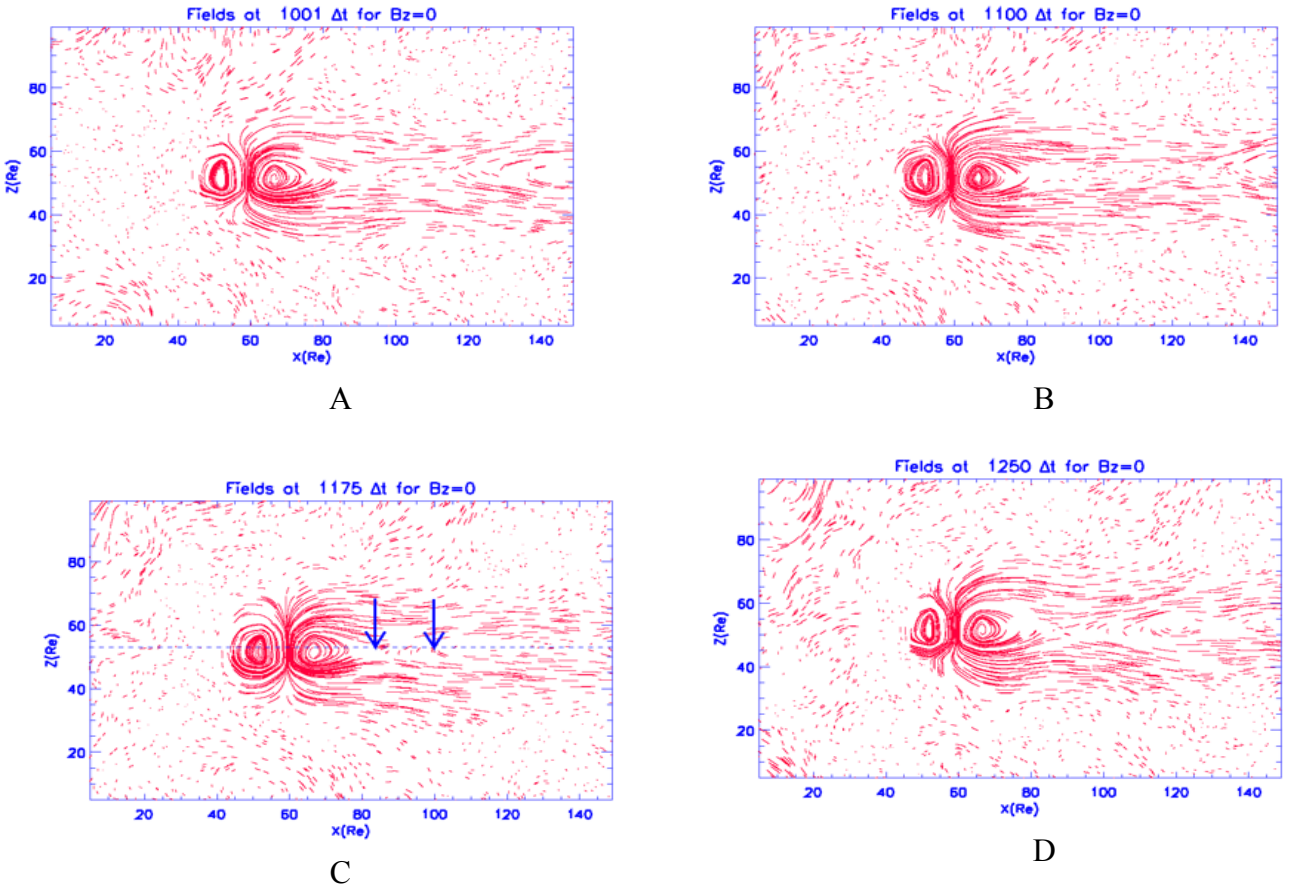

Figure 4.4. Time sequence of the response of Earth's magnetosphere to a depression (air pocket effect) in the incident Solar Wind flow for Bz=0. Field lines are shown in panels A, B, C, and D, taken at 1001, 1100, 1175, and 1250 Δt, respectively. All plots are shown in the x-z plane located at y= 52Δ

4.5 Other examples of field lines topology in dawn-dusk and south-north planes.

Following the same presentation of section 4.3 for plasma distribution, we discuss here two examples of field lines topology obtained respectively in dawn-dusk plane and in south-north plane. First, in Figure 4.5 plotted in x-y plane (at z=53Re), four panels show the field's lines topology at different time span. In Figure 4.5(A) taken at 1001 Δt, the field lines are bent around the

magnetosheath in both dawn and dusk directions. Instabilities in the field' lines grow slightly around x=25Re consequent to the air pocket effect. Along the equatorial plane in the night side, field lines are stretched out tailward and diverted slightly toward dusk which corresponds to plasma density in Figure 4.2(A). In Figure 4.5(B) taken at 1100Δt, the modification of the previous sketch is seen in the confinement of the field's lines topology at the nightside and the advancement of the instabilities toward the magnetopause as the gap is now approaching that point. In Figure 4.5(C) taken at 1175Δt, as the magnetopause expands and reaches a yielding point to break up; we can't see the corresponding field lines breaking up in as the field main component is across the x-y plane. The breaking up of the magnetopause boundary appears here at both dawn and dusk side. Fields' lines at the magnetotail are observed getting denser and packed in which is corresponding to the dense plasma at that region. In Figure 4.5(D) taken at 1250Δt, remarkable instabilities grow at the beginning of the simulation box. These instabilities reflect the plasma injection update of the fast solar wind drift velocity in the dayside of the magnetosphere. These instabilities seem to connect to the position of the gap that now passed over the planet position. At the magnetotail, from x=80 to the end of the simulation box, field lines are stretched out there and drifted duskward.

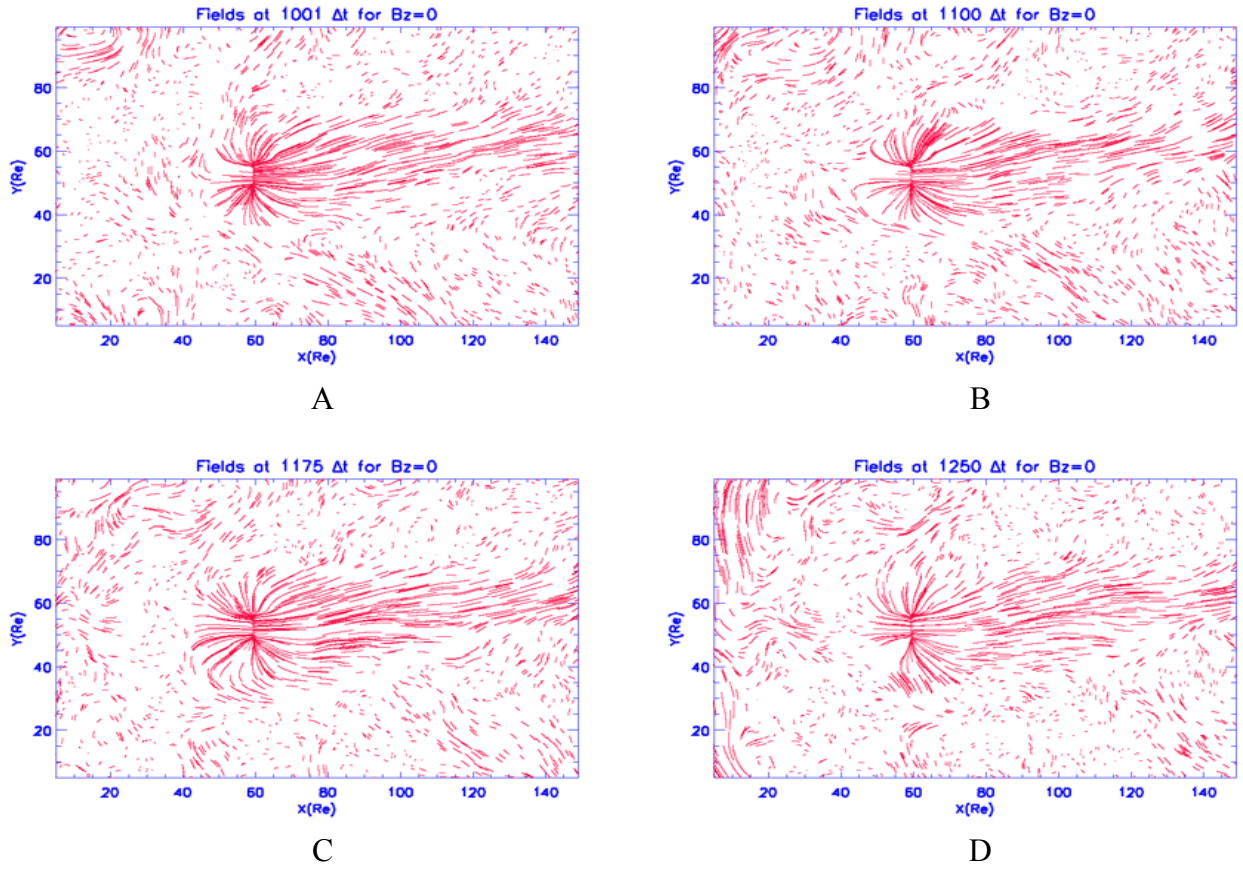

Figure 4.5. Time sequence of the response of Earth's magnetosphere to a depression (air pocket effect) in the incident Solar Wind flow for Bz=0. Field lines are shown in panels A, B, C, and D, taken at 1001, 1100, 1175, and 1250 Δt, respectively. All plots are shown in the X-Y plane located at Z= 53Δ

Second, in Figure 4.6 plotted in y-z plane at x=60Re, four panels show the field's lines topology at different time span. In Figure 4.6(A) taken at 1001Δt, field's lines at the dawn side (East) are seen peeled off back at both north and south direction, while the corresponding lines are confined at the dusk side (West) of the planet. The footprints appearance of instabilities can be seen all around the planet. The particular reason of this appearance is directly related to the abrupt change in the dynamic pressure and the proximity of the advancing gap to the planet at that step time. In Figure 4.6(B) taken at 1100

Δt, the field lines are again peeled off at the dawn side back to dusk side. An example of this process can be seen at (x,z)=(48,67 and 49,36)Re nearby the cusps region. The signature of instabilities shown in Figure 4.6(A) is seen here but at a different position due to their dynamic nature. In Figure 4.6(C) taken at 1175 Δt, a new situation is seen here, the field lines at the dawn side are not peeled off, but rather opened; at this particular time the magnetopause in the x-direction is broken up and its expansion is widened in 3D. The field lines are straightened at the northern and southern cusps regions, which resembles upright position of the cusps in Figure 4.1(C). In Figure 4.6(D) taken at 1250 Δt, the depression effect of the solar wind is over, and the field's lines topologies are recovered as a normal dipole configuration. It is worth to note that the peeling off of the field's lines appeared during the approaching of the solar wind plasma flow to the planet position (figure 4.3(B and C)), which signifies particle entries in/out the inner magnetosphere.

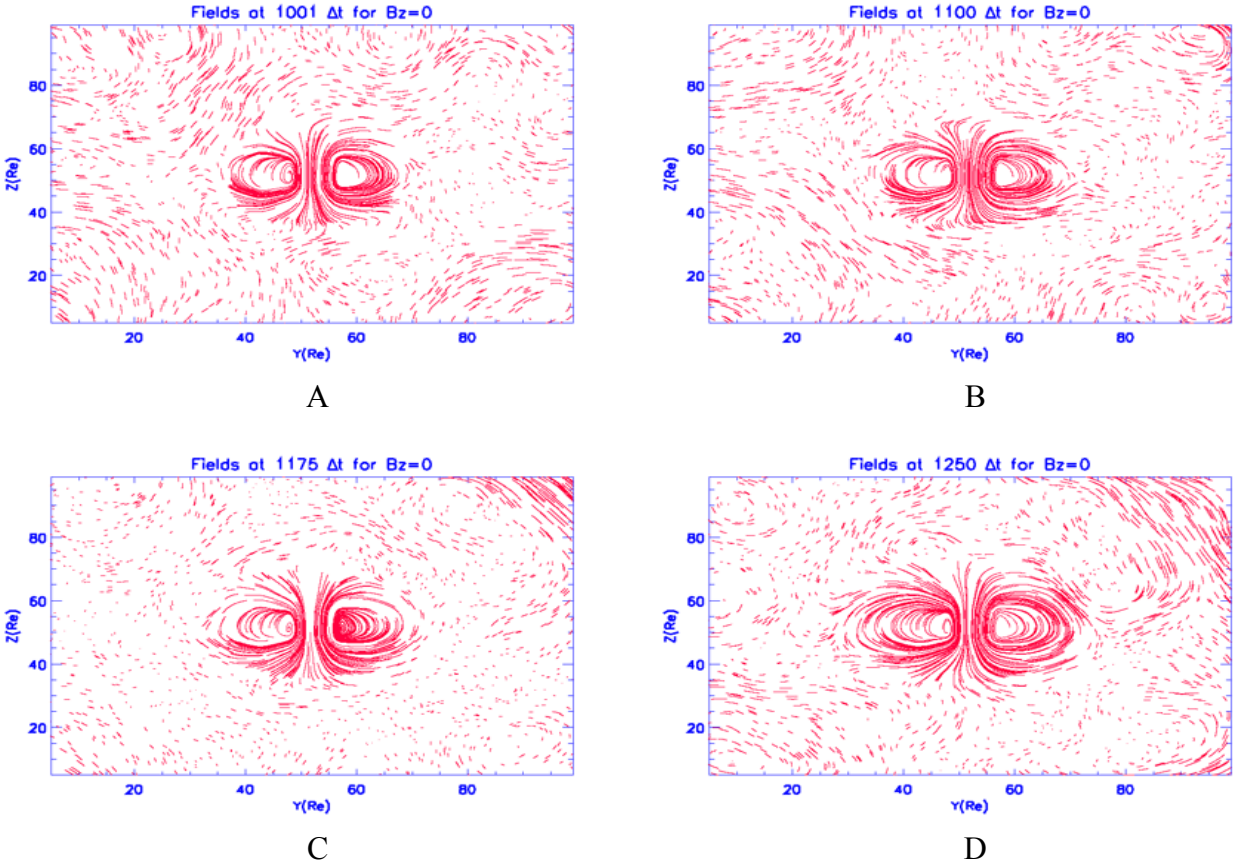

Figure 4.6. Time sequence of the response of Earth's magnetosphere to a depression (air pocket effect) in the incident Solar Wind flow for Bz=0. Field lines are shown in panels A, B, C, and D, taken at 1001, 1100, 1175, and 1250 Δt, respectively. All plots are shown in the Y-Z plane located at X=60Δ

4.6 Analysis and Comments

Two points are worth to discuss here before we present some concluding remarks. The first pertains to the breaking up of the nose of the magnetopause as it responds to the depression of the solar wind. The second point refers to the detachment of plasma blobs from the downstream edge of the generated gap.

In the first point, we noticed that after an expansion phase necessary to respond to the drop of the dynamic pressure of the incoming solar wind, the outer boundary (nose) of the magnetopause

breaks up with open magnetic field lines at a distance of ~15.48Re from Earth. This result is confirmed from both the plasma density and the distribution of field lines (e.g., Figures 4.1(C) and 4.4(C)). When we think of the magnetopause as an interface of equilibrium between two opposite magnetic and particle pressures, our results for the case with no IMF show that the magnetopause (MP) boundary is dragged far enough from its equilibrium position to lead it to break up. In addition, no apparent modification in the global field resists this inflation. Indeed, in our case, there is neither ionosphere-magnetosphere coupling nor flux tubes that transfer plasma from the upper ionosphere into the inner magnetosphere and, hence, no modification of the magnetic field strength. As long as we discussed the plasmas density and fields' topologies in 3D, it is worth to also discuss the response of the magnetopause to the depression of the solar wind in 3D. Figure 4.7 gives an analytical description in 3D of the expansion/contraction of the magnetopause due to the air pocket effect

In Figure 4.7, panels A, B, and C represent the expansion/contraction phase when B_z=0 and when they are measured through the size of the magnetopause along x (from Earth), y (dawn to dusk), and z (south to north), respectively. Here, x represents the Sun-Earth line (at (y, z) = (52, 53)Re), y represents dawn-dusk line (at (x, z)=(60, 53)Re), and z represents south-north line (at (x, y)=(60, 52) Re); no tilt is assumed. To locate the magnetopause boundary along any axis, we plot the density profile and look for the abrupt drop-off of the density by definition of the stagnation region. Next, we measure the position of that density edge relative to the Earth's position at (x, y, z) = (60, 52, 53)Re. In panel A, the magnetopause response to the abrupt change shows a nearly-fast linear expansion of its size from ~10Re up to ~15Re between 1117 and 1130 Δt. Since the gap (air pocket effect) extension is large enough, the induced non-restricted force blows off the magnetopause structure and the magnetopause boundary breaks up at ~15.5Re at ~1132 Δt, leaving the magnetopause with an open boundary. As the upstream gap boundary moves closer to the new, expanded magnetopause, plasma

accumulates and again produces enough dynamic pressure to balance the dipole magnetic one. It is interesting to note how that expansion phase (in terms of distance) grows faster than the recovery phase. In panel B, the magnetopause in y direction with B_z=0 shows a different behavior. Its length expands from 17Re up to 28Re, but between 1141 and 1198 Δt, the length relaxes for 4 Δt, and then the magnetopause shrinks back for ~ 2Re (probably due to induced pressure by the tiny particle ensembles inside the gap) and stays there until 1204 Δt. At 1204 Δt, the system again starts its expansion for ~4Re up to 1208 Δt. At this stage, the system enters the recovery phase and restores its average length of (~14Re) at 1244 Δt. Figure 4.7(C), obtained similarly when B_z=0, reveals that the expansion phase along z reaches ~21 Re between 1081 and 1124 Δt, then shrinks for 10 Δt for ~ 1.4Re. It expands again to ~ 27Re at 1162 Δt and recovers its initial value between 1162 and 1225 Δt.

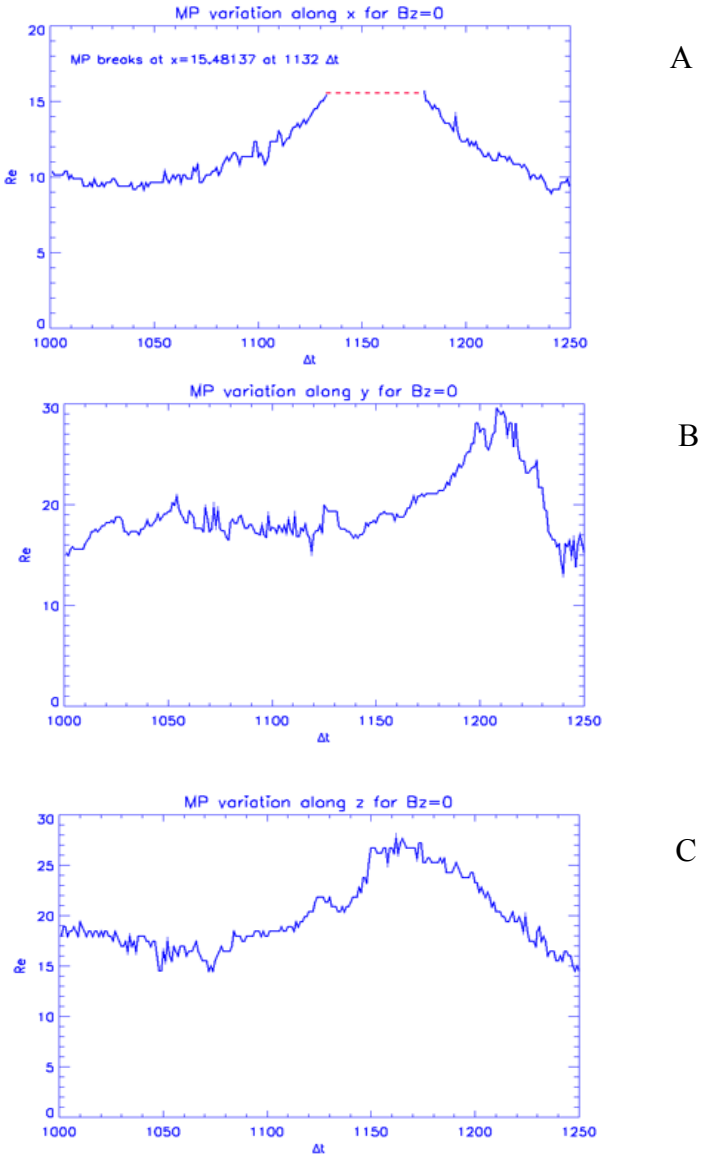

Figure 4.7**.** Magnetopause expansion/recovery measured from Earth location (x, y, z)=(60, 52, 53)Re in 3-D along x, y, and z axis for B_z=0 (panels, A, B, and C). Panel A shows that during its expansion phase, the MP breaks down at a distance ~15Re from Earth when zero IMF is applied.

To better understand the expansion phase of the MP surface, we study in the following the dynamics of the reversed clouds/blobs of plasma inside the generated gap. The blobs are defined as those ensembles of low density plasmas that are seen detach from the gap downstream boundary and reverse direction against the stream. Here, we adopted the analytical method of Mishin (1993) to calculate the different plasma pressures inside the gap and around its upstream and downstream sides. At an early stage of the process and downstream of the gap, one may sketch a simple scenario: the drop in the solar wind drift velocity from $V_1 = 0.25$ to $V_2 = 0.1$ induces a pressure gradient $\Delta P=\rho*((V_2)^2 - (V_1)^2)$ that should drive a mechanical force $F = \Delta P/\Delta l$ oriented along the x-axis, where Δl is a scale length that should be close to the width of the gap's edge. Because $\Delta P < 0$, this mechanical force is directed sunward and should accelerate particles back from the upstream of the magnetopause. As the flow has an initial bulk velocity directed opposite to the force direction, the induced force will stop the particles and then reverse their velocity direction sunward (against the initial direction of the flow). The fascinating result is that the mechanical acceleration is so strong in the gap region that the plasma is blown off backward, sweeping the field lines away with it. This result is responsible for making the MP expansion run linearly along x, and later causing it to break up at a certain distance.

For the sake of clarity, a region zoomed in between $10\Delta \le x \le 89\Delta$ and $30 \le z \le 69\Delta$ was selected. As shown in Figure 4.8, and much like coronal mass ejections from the Sun, we see the formation of blobs of plasma (two are circled in the image) that are ejected into the gap space after a lapse of time. We believe that these unusual blobs are the consequence of the mutual impacts, respectively, of the depression force and the instability of the plasma layer that stands upstream in the magnetopause.

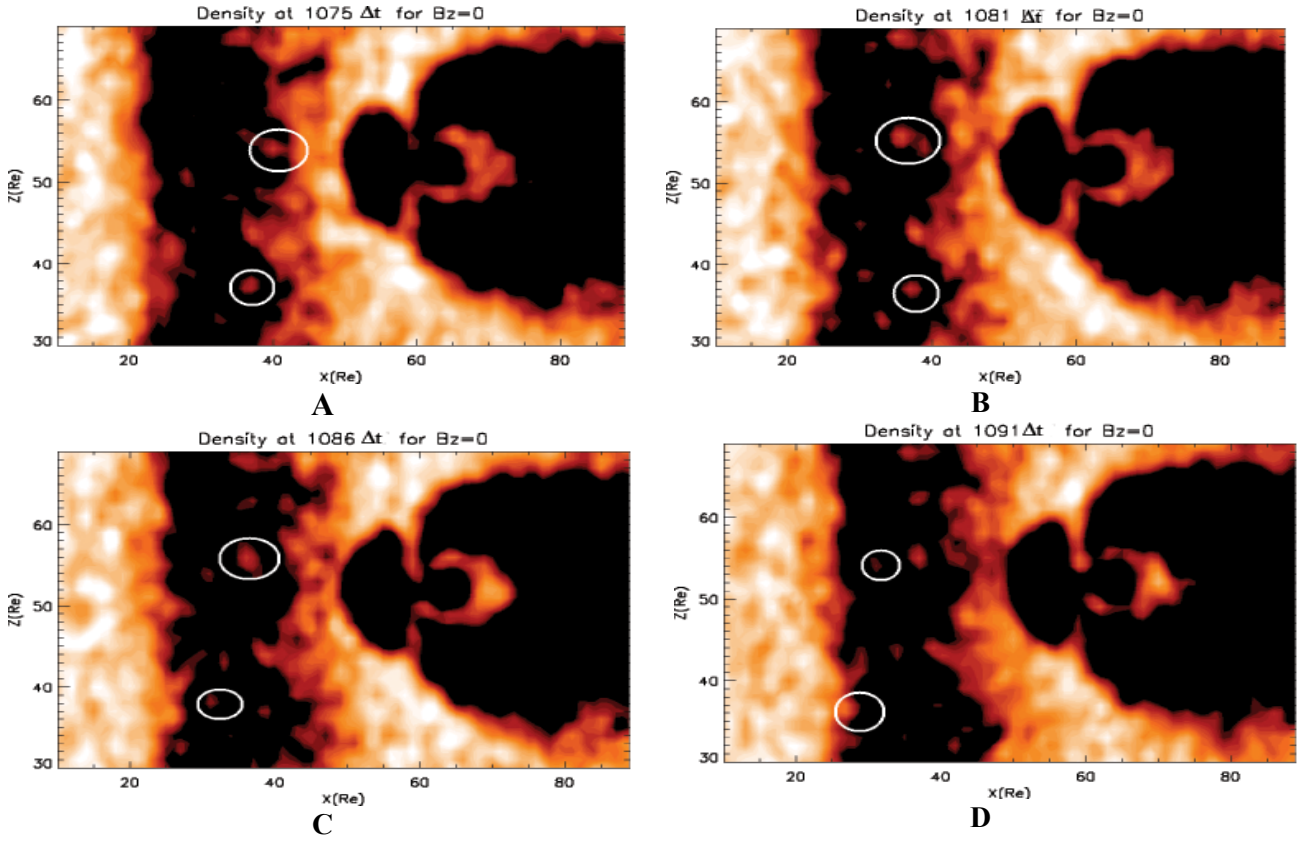

4.8**.** Time sequence of the detachment and sunward travel of a blob of plasma in the gap when no IMF is applied (B_z=0). Plasma density is shown in panels A, B, C and D, taken at 1075, 1081, 1086, and 1091 Δt respectively. All plots are shown in the x-z plane located at y= 52Re and zoomed in between x = [10-89]Δ and z = [30-69]Δ. Images' contrast was increased to highlight the blobs.

4.7 Conclusion and Remarks

The 3D description of plasma and fields in this chapter was particularly important to give a global image of the magnetospheric structure at any time. For example, Figure 4.1(C) shows the cusps nightside oriented, but when look at figure 4.3(C) one can have more insight about the orientation of the cusps in the dawn-dusk direction. This suggests the importance for numerical modeling to acquire a global and instantaneous description of the magnetosphere structure as it responds to the variability of the solar wind dynamic pressure. In this chapter it was shown that low density plasma inside the generated air pocket reversed direction at an early time of the onset of the simulation process. Blobs of plasma get detached from the downstream edge of the gap, reducing by mass loss the width of the plasma layer that sustains the magnetopause. An intriguing result was obtained when the magnetopause dayside boundary broke up during its sunward expansion phase, an expansion that started as soon as the advancing gap got close enough to that region. Other interesting results show that the orientation of the cusps is highly affected by the depression in the solar wind flow while lobes flared out. Also, our simulation showed that one can track up to two X points in the magnetotail neutral sheet as indicated by two arrows in Figure 4.4 (C) [same double x-points may also be seen in figure 4.4(D)=]. These results will be further discussed in chapter 8 when comparing to observations

Chapter Five

The Impact of a Solar Wind Depression (Air Pocket Effect) on the Dayside Magnetopause During Southward Interplanetary Magnetic Field.

5.1 Introduction

In chapter 4, the impact of the solar wind depression on the day side magnetopause during the absence of the interplanetary magnetic field (IMF) was discussed. This chapter will follow up the same scheme but with the presence of IMF which was chosen southward oriented with a steady state flow Vsw=-0.2. Four time spans were chosen as a common duration of time for all cases in all directions which are 1001, 1100 and 1175 and 1250 Δt. The plasma density distribution will be discussed in 3D in Figures 5.1, 5.2 and 5.3. The corresponding field's lines topologies will be discussed in 3D in Figures 5.4, 5.5 and 5.6 respectively. Section 5.2 and 5.3 will be devoted to the description of the plasma distribution in noon-midnight plane, dawn-dusk plane and south-north plane respectively. Section 5.4 and 5.5 will be devoted to the description of fields' topologies in noon-midnight plane, dawn-dusk plane and south-north plane respectively. In section 5.6, analysis and comments are presented to discuss the results obtained so for, part of which figure 5.7 will describe the magnetopause expansion/recovery in 3D. In section 5.7, the main results of our simulation will be briefly summarized.

5.2 Plasma Distribution in Different Time Span along Noon-Midnight Plane

We present the results of the interaction of a solar wind "air pocket" with Earth's magnetosphere when IMF is included as a steady southward field (B_z<0). As in the previous chapter, the system is first allowed to become established before the depression takes place at 900 Δt; Vsw is then reduced from 0.25 to 0.1 and, accordingly, the ram pressure drops by 60% during 100 Δt before being restored to its initial value (see Figure 5.1(A), taken at 1001 Δt). This effect results in the formation of a 15Re wide gap (shown between two opposite arrows in the figure) located between 10Re and 25Re along the x-axis, as shown in Figure 5.1(A). The classical structure of the Earth's magnetosphere is easily observed, and one can see the signature of the Earth's bow shock at 44-48Re. The cusps are quite prominent and nightward-oriented. In figure 5.1(B), taken at 1100 Δt, an expansion of the magnetopause sunward is noticed due to the depression ahead of the nose. Bow shock can be seen at around ~ 48Re along the x-axis. As the gap moves downstream Earthward, it begins to show a curvature around 5-20Re and 80-100Re along the z-axis that appears as a departure from the z-direction toward the planet. This curvature is the result of the gap's boundary that begins to respond to the strong magnetic pressure of the Earth on the Sun-Earth symmetry line, whilst across, at both ends of the boundary along z, this pressure is not yet fully felt, and thus the gap's boundary continues its forward motion unimpeded. More clouds of plasmas are seen filling the generated gap. The cusps are clearly seen, and clouds of plasma are also seen along the neutral line on the nightside. The magnetopause is still in its expansion phase at this stage, having a length of ~12.3Re from Earth along the x-axis.

In Figure 5.1(C), taken at 1175 Δt, the subsolar magnetopause starts retreating Earthward at around 43Re (Earth position is 60Re). We observe that the plasma flow enlarges the indentation at the cusp. On the other hand, the cusp region expands toward the poles. At this particular time, we clearly

see a ~2Re thick belt/sheet of plasma formed at the dayside of the magnetopause; it appears at the nightside and has a thickness of about ~3Re. Here, the dayside magnetopause structure never breaks as it did when B_z=0 discussed in chapter 4. In Figure 5.1(D), taken at 1250 Δt, the dayside magnetopause recovers its classical shape after the gap's boundaries pass over the planet. The effect of the reduction of the ram pressure can be felt at 63-80 Re along x. We see that the cusp outflow region becomes more flared relative to the Earth-Sun line. At 100-140Δ, we observe that the tail boundary is reduced, thereby increasing the plasma sheet thickness. Birn (2005) discussed the relation between the tail boundary reductions and the plasma sheet thickness at the magnetotail**,** a relation that our simulation seems to confirm. The denser plasma comes from the nightside that feeds the equatorial plane along the neutral line.

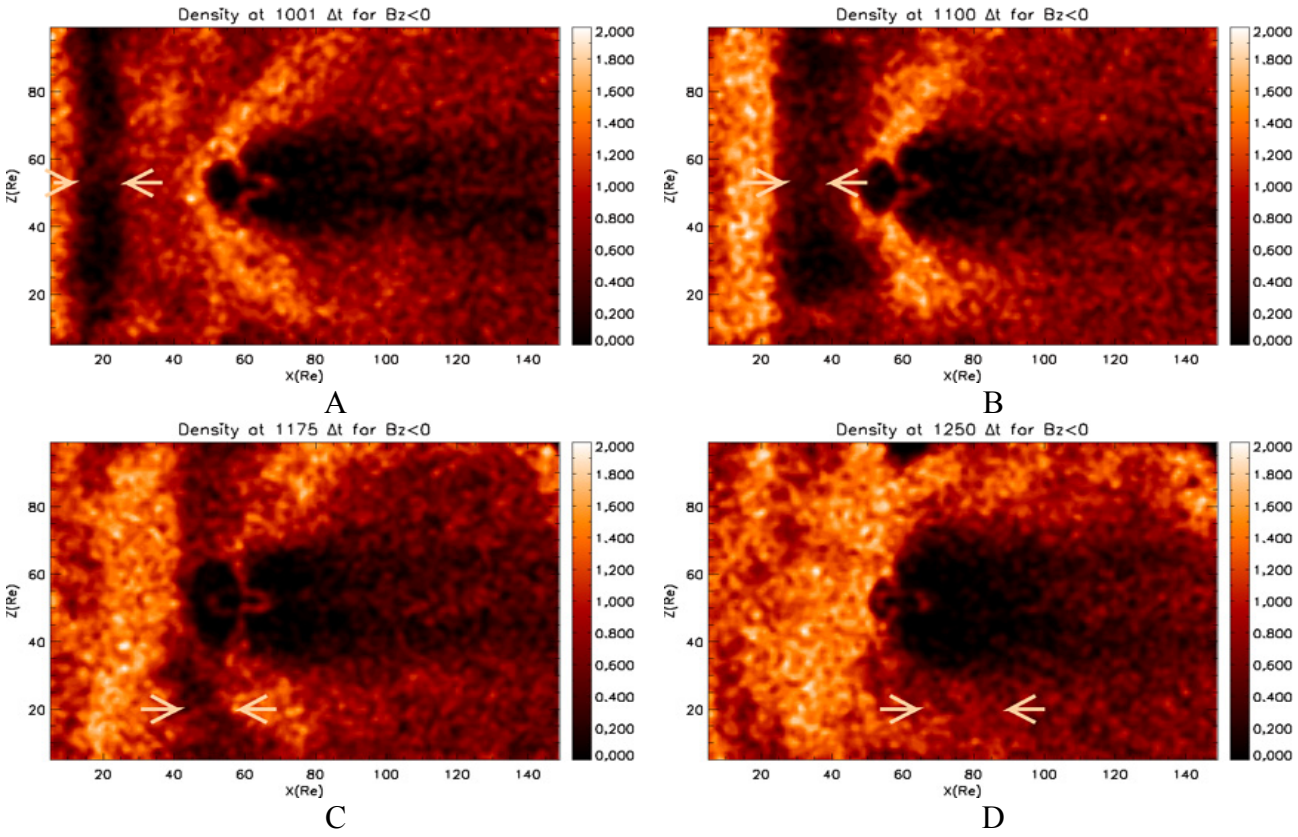

Figure 5.1. Time sequence of the response of Earth's magnetosphere to a depression (air pocket effect) in the incident Solar Wind flow for Bz<0. Plasma density is shown in panels A, B, C, and D, taken at 1001, 1100, 1175 and 1250 Δt, respectively. All plots are shown in the x-z plane located at y= 52Δ.

5.3 Other examples of plasma distribution seen in different planes such as dawn-dusk and south-north directions

In the same context as we did in chapter 4, we now present the plasma density distribution in different planes. We will present here four images in dawn-dusk plane (x-y plane at z=53Re; equatorial plane) and other four images in south-north plane (y-z plane at x=60 Re), all taken at the same time span of 1001, 1100, 1175 and 1250 Δt respectively. By doing so, we tend to acquire a global description of the plasma distribution when IMF is southward oriented.

First, in figure 5.2(A) taken at 1001Δt, the classical structure of the Earth magnetosphere is observed in the equatorial plane, where the gap is shown (indicated by opposite arrows in the figure) between x=10 and x=25Re. The signature of the bow shock is observed at x=44Re. A trapped region of plasma of thickness ~3Re at the night side appears as a concaved shape sideway to the planet. Plasma clouds are filling the equatorial plane at the night side especially at x=82 and onward. In figure 5.2(B) taken at 1100 Δt, the expansion of the magnetopause sunward is noticed. The gap moves earthward, and starts showing a curvature around the magnetopause; inside which blobs of plasma are seen all over. The magnetotail contracted earthward setting a temporary new boundary of plasma at x=95Re. This contraction is a signature of reconnection in the magnetotail. In the inner magnetosphere, a strip of plasma, more oriented toward dawn, is seen adjacent to the inner boundary of the magnetopause, which is another signature of possible reconnections. In figure 5.2(C) taken at 1175Δt, the gap now moves in the magnetospheric region, and its curvature described in preceding figures leave a very low density two parcels at the boundary of the simulation box(see the zone indicated by the two arrows in the figure) along y-directions. It is worthy to note that during this expansion of the magnetopause, it didn't break up as it was the case at the same duration of time when B_z=0. In figure 5.2(D) taken at 1250 Δt, one clearly sees the plasma belt which was shown in Figure 5.2(C), now extends from x=55 out to 64

Re along x-direction. The magnetopause recovered its classical shape as the gap passes over the planet position. Almost an empty parcel indicated by the two arrows in the figure at the far y-direction indicates the gap position at this particular time. The contraction of the magnetotail is still seen in this figure at x=103Re.

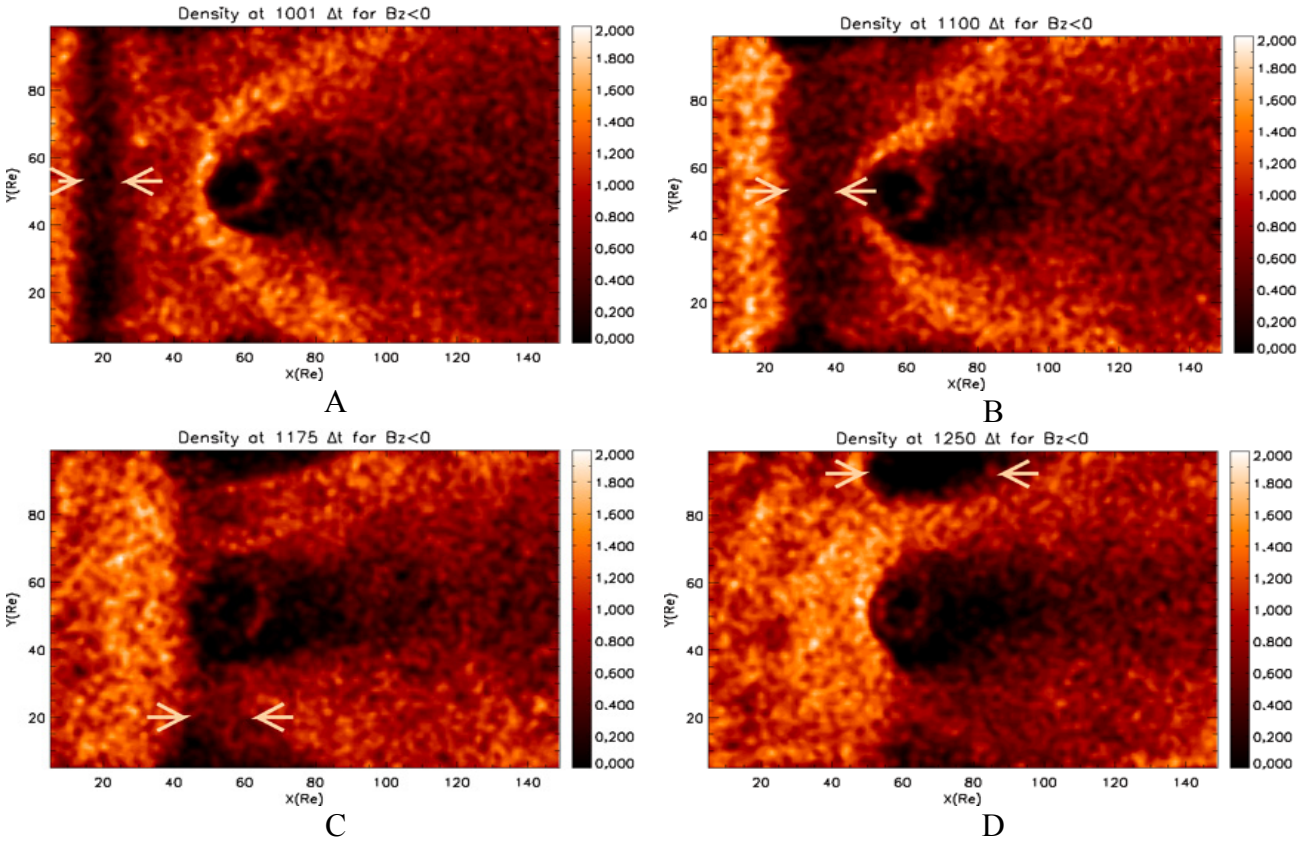

Figure 5.2 Time sequence of the response of Earth's magnetosphere to a depression (air pocket effect) in the incident Solar Wind flow for Bz<0. Plasma density is shown in panels A, B, C, and D, taken at 1001, 1100, 1175 and 1250 Δt, respectively. All plots are shown in the x-z plane located at y= 52Δ.

As a second study, we now show the plasma density distribution in the south-north direction (y-z plane at x=60Re). In Figure 5.3(A) taken at 1001 Δt, the northern and the southern cusps alike are pointing toward the dusk direction. A doughnut shape of plasma, which has an average thickness of ~1.5Re, is seen inside the magnetospheric cavity. In figure 5.3(B) taken at 1100Δt, both cusps show the same orientation as the previous figure and point duskward. The doughnut shape is squeezed in the right hand side of the planet (toward dawn) and relaxed in its left hand side (toward dusk). Plasma entering from north and south poles are seen at the upper/lower dusk side of the magnetospheric cavity. In figure 5.3(C) taken at 1175, as the gap moves inside the magnetospheric cavity at this particular time, the gap boundaries, indicated by the arrows in the figure, show the strength of the created disturbance more clearly in y-z plane. The plasma doughnut broke up at the dusk direction and connected to the magnetopause in the y-direction. The northern cusp is almost upright, whilst the southern cusp is dusk oriented. The gap in figure 5.3(D) taken at 1250 Δt, is more driven toward nightside along x direction at the dawn side boundary. This explains that we still see it in the duskward direction but not in the dawnward direction.

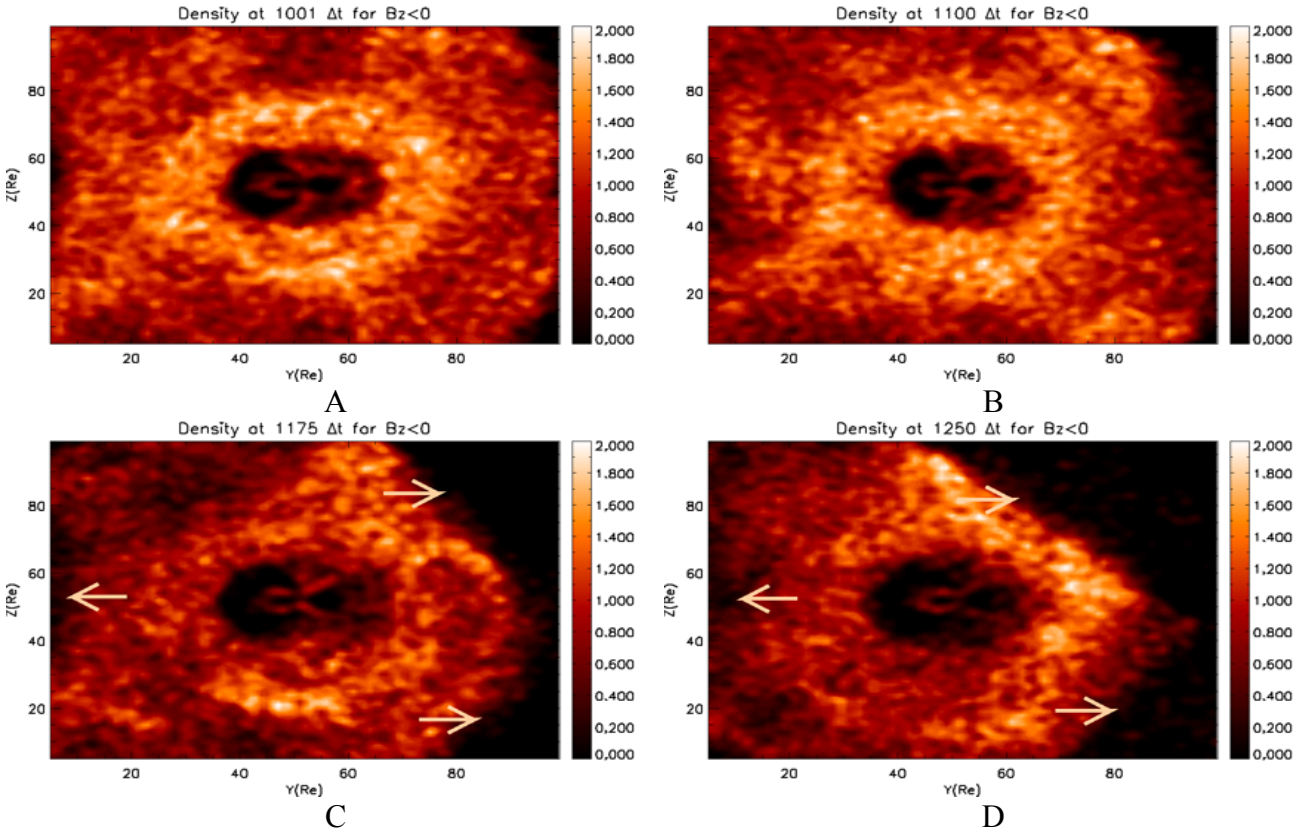

Figure 5.3 Time sequence of the response of Earth's magnetosphere to a depression (air pocket effect) in the incident Solar Wind flow for Bz<0. Plasma density is shown in panels A, B, C, and D, taken at 1001, 1100, 1175 and 1250 Δt, respectively. All plots are shown in the x-z plane located at y= 52Δ.

5.4 Field topologies in different time span along noon-midnight plan that correspond to the above mentioned plasma distribution

We discussed the plasma density distribution in 3D in the last three sections and built up a global idea about the behavior of the plasma when the Earth magnetosphere responds to a depression in the solar wind flow. Now we need to see the corresponding fields' topologies in the same manner as have been previously described. We start by the fields' topology at the noon-midnight plane as in Figure 5.4.

Figure 5.4(A) shows the field topology corresponding to the particle density in Figure 5.1(A). The diffusion of the field lines with respect to the plasma at 15-30Re shows a drop in their strength because of the noticeable drop of the plasma dynamic pressure in that area. An opening of the field lines and the signature of reconnection are observed at the dayside magnetopause. This signature is seen better at (x,z)=(43,37)Re, when the image is zoomed between (x=5-80Re) and (z=25-90Re). The Earth's bow shock is seen at ~42-46Re. At the upper and lower lobes of the magnetotail at points (x, z) = (100, 62) Re and (100, 43)Re, respectively, a fishtail shape configuration is observed. In addition, an X-point formed at ~80Re.

In Figure 5.4(B), instabilities seen at 5-30Re are due to the cumulated effects of the new, fast-approaching solar wind plasma as well as the plasma that slows down from the gap during 100 Δt. Indentations of the field intensities are seen ahead of the subsolar point and reflect the existence of the bow shock from 30-60Re. Enlargement of the dayside configuration of the magnetopause at the Sun-Earth line is seen at 46Re along x (Earth's position is 60Re). Field lines are driven tailward, and in this instance, an X-point is observed at ~80Re. The fishtail configuration appears with roughly the same position as the previous case. In figure 5.4(C), as the upstream boundary of the plasma approaches the subsolar point, field lines become stronger—a sort of convection. The upstream of the air pocket effect

now hits the expanded magnetopause at the distance of ~42Re (at 18 Re from the planet). The expansion of the magnetopause along the south-north direction is seen in the field topology. Magnetic erosion takes place in which field lines are bent tailward rather than squeezed; as a result, they feed the tail with particles. An X-point is seen at ~80 Re on the nightside, and the instabilities seen in figure 5.4(B) move Earthward. In Figure 5.4(D), the magnetic field topology at the magnetopause restores its classical bullet-like shape after the induced gap boundaries pass over the planet position at 60Re. Field lines in the cusp region show inclination to the nightside direction: in other words, this system is highly dynamic, even in a very short instance of time. The topology seen in this figure resembles the classical structure of the magnetosphere field representation. The fishtail configuration is now more flared out due to the air pocket effect at points (x, z) = (90, 70)Re and (90, 42)Re, respectively, up to the box boundary.

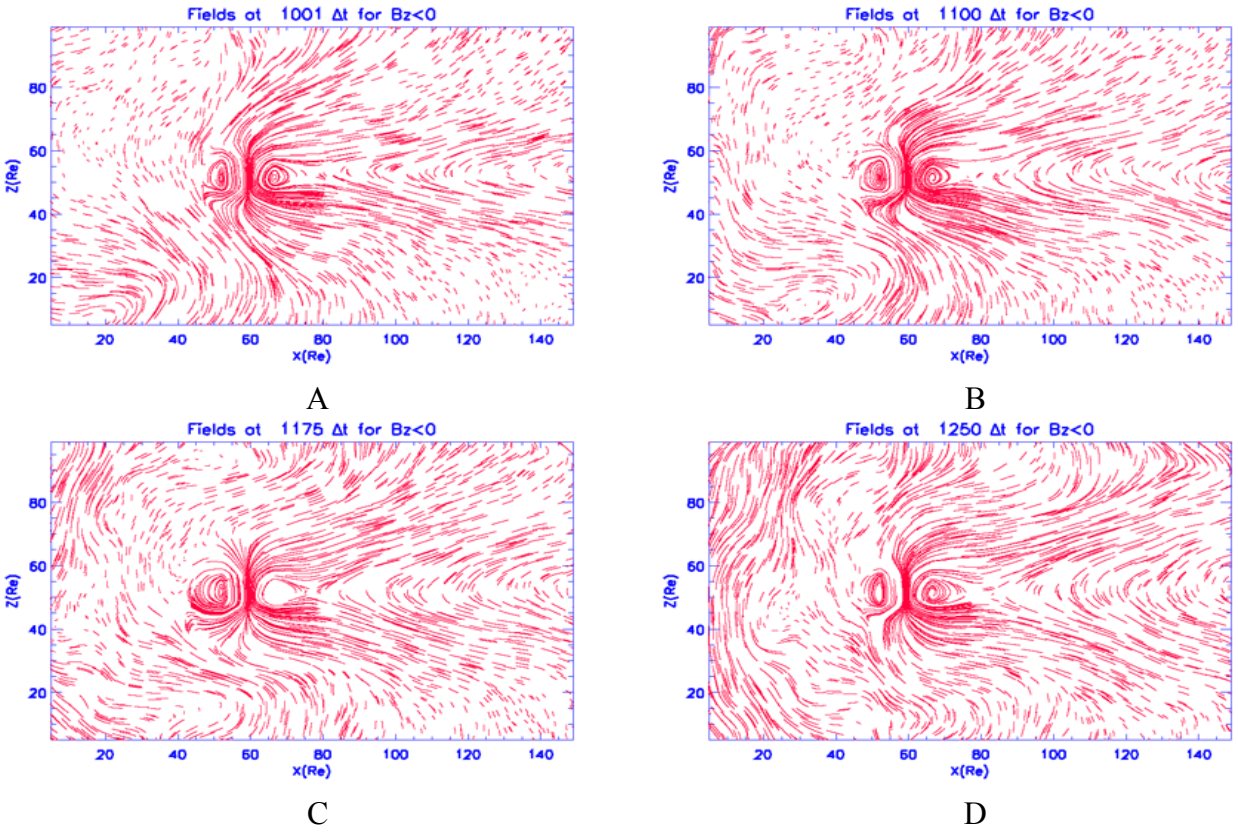

Figure 5.4. Time sequence of the response of Earth's magnetosphere to a depression (air pocket effect) in the incident Solar Wind flow for Bz<0. Plasma density is shown in panels A, B, C, and D, taken at 1001, 1100, 1175 and 1250 Δt, respectively. All plots are shown in the x-z plane located at y= 52Δ.

5.5 Other examples of fields' topologies seen in different planes such as dawn-dusk and south-north directions.

Two field configurations are presented in this section: in the dawn-dusk plane (in x-y plane at z=53Re; figure 5.5) and in south-north plane (in y-z plane at x=40; figure 5.6).

First, figure 5.5(A) taken at 1001Δt, shows the field's lines topologies in the equatorial plane directed tailward. At the nightside of the planet, there is a clear drift of the field lines toward dusk side. Instabilities of the field lines appear along x direction between y=70-90Re. In figure 5.5(B) taken at 1100Δt, at x=73Re out to 110Re, we see that the field line across the equatorial plane at the nightside is clearly flared out toward the dusk. After this distance, field lines are drifted again along the x-direction. A small fishtail field configuration can be observed at x=144Re between z=50 and 63 Re. In Figure 5.5(C) taken at 1175Δt, as now the gap occupies the inner magnetosphere position, the field's lines at the dayside look uniformly distributed, while at the nightside they are straightened and directed toward the neutral line. Instabilities are observed at the beginning of the simulation box, provided that these instabilities might be related to the new solar wind plasma update. In other word, the plasma to the left of the upstream of the generated gap is fast plasma; this may make the disturbances in the flow In Figure 5.5(D) taken at 1250Δt, most if not all the plasma at the dayside have restored its strong initial drift velocity, hence the dynamic pressure is updated by the square of the drift velocity. Therefore, the dynamic pressure dominates the weak southward magnetic pressure, which results in these strong instabilities all around the dayside. The field lines at the night side are almost straightened out toward the tail. A clear vortex appears centered at (x,y)=(130,91)Re

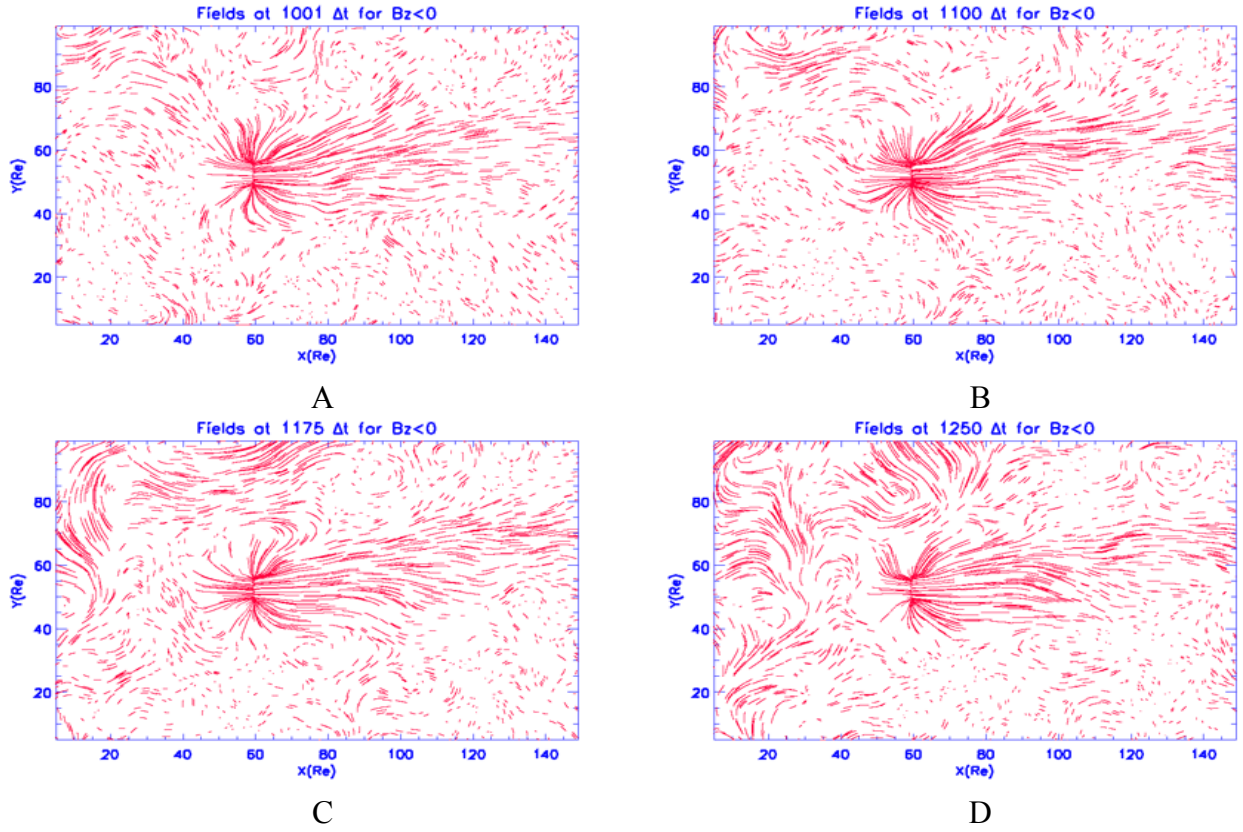

Figure 5.5. Time sequence of the response of Earth's magnetosphere to a depression (air pocket effect) in the incident Solar Wind flow for Bz<0. Plasma density is shown in panels A, B, C, and D, taken at 1001, 1100, 1175 and 1250 Δt, respectively. All plots are shown in the x-z plane located at y= 52Δ.

Second, the field's lines topologies will be presented in the south-north direction (at y-z plane at x=60Re). In Figure 5.6(A) taken at 1001Δt, the y-z plane reveals important view of the dipole structure and the resultant topology of the field and the possible reconnections either at the dawn-dusk, south-north directions or the cusps. For example at (y,z)=(37,46)Re and at (y,z)=(67,48)Re, signature of reconnection is clearly seen. In the cusps regions signature of reconnection is observed at the north cusp at (y,z)=(49,66)Re and at (y,z)=(49,36)Re at the south cusp. In figure 5.6(B) taken at 1100Δt, the field lines are opened and peeled off back in the dawn side around the dipole, but on contrary they are confined in the dusk side. Field lines at the cusp region are dense and mostly drifted at dusk side as compared by position to their corresponding regions in the plasma of Figure 5.5(B). In Figure 5.6(C) taken at 1175Δt, field's lines are widely flared out at the dawn side, and more confined and slightly drifted toward the south at the dusk side as the gap now is at the planet position. What appears at the two right corners of the simulated box corresponds to the empty parcels shown in figure 5.3(C). investigation the corresponding fields, yields that the field's lines within the limit of the said parcels are very week, then the strong configurations of these line's are not a sign of the magnetic fields, but rather a sort of noise. In fact, it is not clear why this happens. Same effect appears in figure 5.6(D)

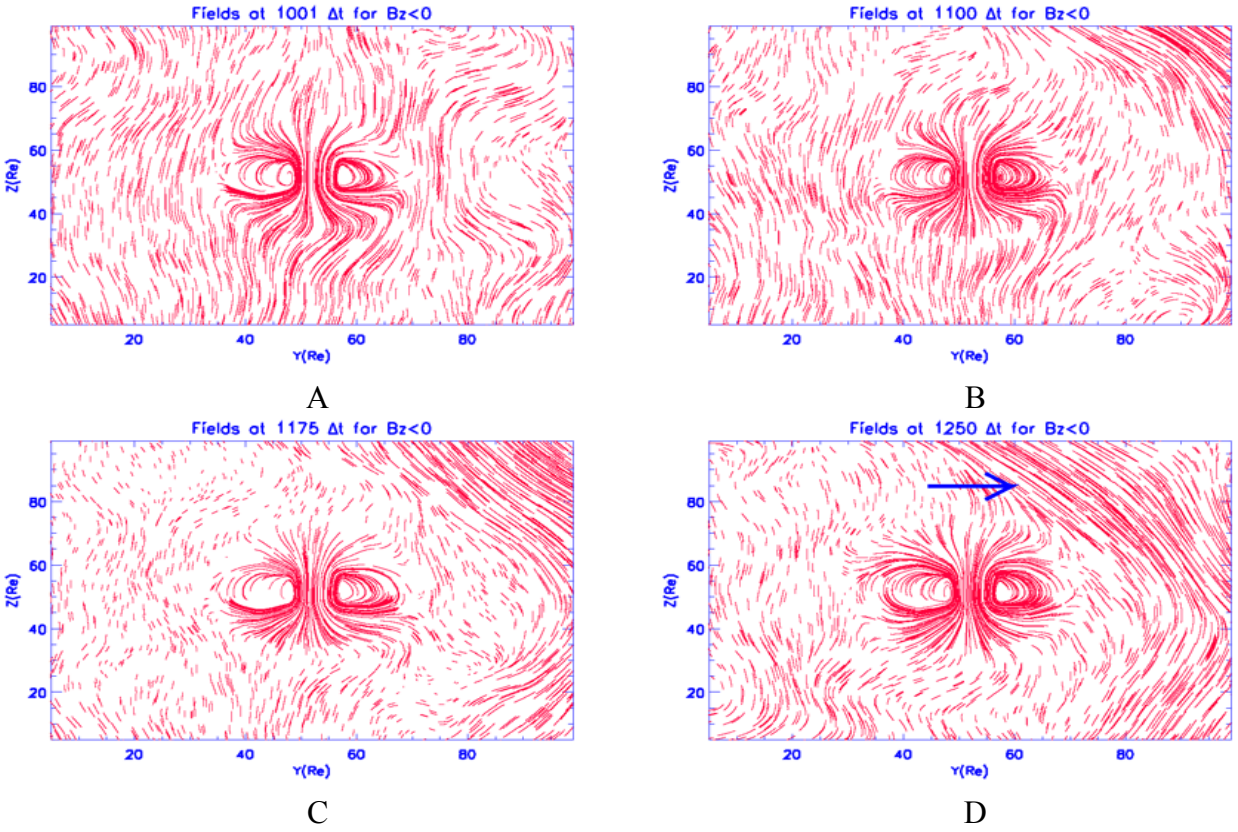

Figure 5.6. Time sequence of the response of Earth's magnetosphere to a depression (air pocket effect) in the incident Solar Wind flow for Bz<0. Plasma density is shown in panels A, B, C, and D, taken at 1001, 1100, 1175 and 1250 Δt, respectively. All plots are shown in the x-z plane located at y= 52Re.

5.6 Analysis and comments

As we did in chapter 4, the response of the magnetopause to the disturbance in the dynamic pressure, is discussed here following the same analysis. In Figure 5.7, panels A, B, and C represent the expansion/recovery phase when B_z<0 as measured through the size of the magnetopause along x (from Earth), y (dawn to dusk), and z (south to north), respectively. Here, x represents the Sun-Earth line (at (y, z) = (52, 53)Re), y represents dawn-dusk line (at (x, z)=(60, 53)Re), and z represents south-north line (at (x, y)=(60, 52) Re); no tilt is assumed. To locate the magnetopause boundary along any axis, we plot the density profile and look for the abrupt drop-off of the density by definition of the stagnation region. Next, we measure the position of that density edge relative to the Earth's position at (x, y, z) = (60, 52, 53)Re.

In Figure 5.7(A), the magnetopause expands from 10Re up to 18Re nonlinearly. Existence of B_z makes the expansion phase slower, thus leading to shorter distances of the MP for the same step time. In other words, the IMF confines the plasma, and the magnetopause never breaks up. This expansion takes place within duration between 1089 and 1172 Δt.

In Figure 5.7(B) the expansion phase takes place very slowly between 1087 and 1205 Δt, and the recovery phase is very fast between 1205 and 1236 Δt. Now, in the expansion phase, the magnetopause size grows slowly and nonlinearly up to ~ 35Re until 1205 Δt. The recovery of the magnetopause size in the y-direction takes place very quickly: it shrinks from ~35 to ~16Re between 1205 and 1240 Δt. We believe that the fast recovery of the magnetopause is due to a magnetic force directed tailward (the slingshot effect) that adds to the magnetic force of the dipole when the dynamic pressure of the solar wind overpasses the magnetopause boundary for B_z<0.

In Figure 5.7(C) we have a perturbed expansion of the size in z-direction for ~ 26Re between 1101 and 1172 Δt; the system then recovers its equilibrium position between 1172 and 1220 Δt. We measured the size of the magnetopause 5Re away from the vertical position of the dipole to avoid the interference of our readings with the cusp's position, a region that is highly susceptible to pressure gradients.

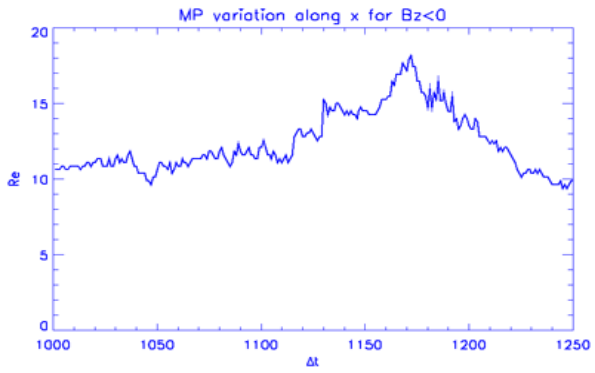

A

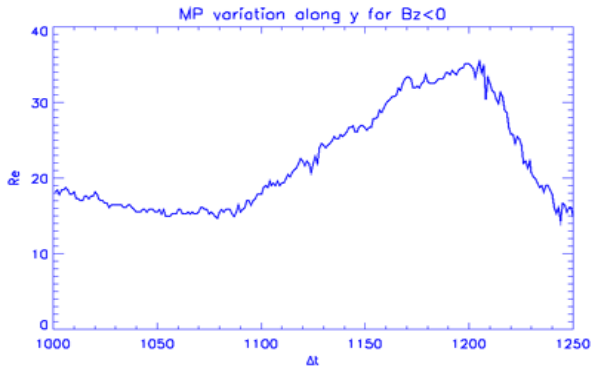

B

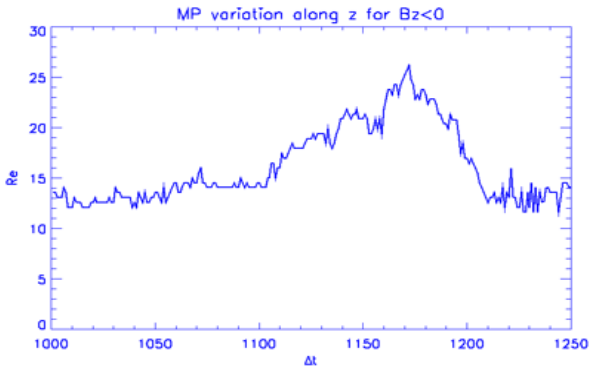

C

Figure 5.7**.** Magnetopause expansion/recovery measured from Earth location (x, y, z)=(60, 52, 53)Re in 3-D along x, y, and z axis for B_z<0 (panels, A, B, and C).

5.7 Conclusion and Remarks

The low density plasma inside the generated air pocket continued flowing along the stream when B_z<0 with more density fillings. The magnetopause, as it responds to the gap effect, sustained its shape and never breaks up. In addition, its expansion/recovery phases were not linear.

Indication of reconnection is observed for B_z<0 through the manifestation of both field's lines topology, and particles injection inside the inner magnetosphere, as seen in the obtained plasma distributions (see Figures5.3(C)). The X-points are observed located more closer to the planet's position because the tail side boundary shrank as compared to the previous case with No IMF included. Earth's bow shock was successfully simulated and was shown for both plasmas and fields.

Chapter Six

The Impact of a Solar Wind Depression (Air Pocket Effect) on the Dayside Magnetopause during Northward Interplanetary Magnetic Field.

6.1 Introduction

In our endeavor to understand the general problem of the Earth magnetosphere response to the variability of the solar wind dynamic pressure, and after testing our PIC code (chapter 3) to simulate strong disturbances in the solar wind flow, we present in this chapter a follow up study of the impact of a depression in the solar wind flow on the Earth's magnetosphere but with north IMF condition ($B_z>0$). We remind that comparable studies were conducted respectively in chapter 4 when no IMF was applied ($B_z=0$), and in chapter 5 for south IMF condition ($B_z<0$). To summarize, we found that the existence of the IMF when southward oriented has apparently a stronger influence in shaping up the Earth's magnetospheric structure. As an example, in response to an air pocket in the incident solar wind (SW) flow, the dayside magnetopause broke up during the expansion phase at ~15Re when $B_z=0$ (chapter 4), but sustained its classical shape when $B_z<0$ (chapter 5). We also found that inside the generated gap "air pocket", there was low density ensembles of plasma 'blobs" which reversed direction and flew against the stream sunward in $B_z=0$ case. By contrast, this reversal was much slower when $B_z<0$. Other findings were that the orientation of the cusps was found to be highly affected by the depression in the solar wind flow, while lobes were flared out when $B_z=0$ due to the

air pocket effect. To complete our diagnostic, it would therefore be useful to see how these results could change when IMF is included but northward.

In this chapter, as in chapters 4 and 5 (Baraka and Ben-Jaffel, 2007), our PIC code is applied to carry out this follow-up study. For reference, we remind that our simulation box has dimensions (155,105,105)Δ, Δ = 1 Re, and is loaded by $2x10^6$ electron-ion pairs, where Earth is located at (60,52,53)Re. The behavior of the plasma distribution and field topology at the dayside magnetopause, including the formed gap (air pocket effect) and the macrostructure of the Earth's magnetosphere are all the focus of this chapter. The time evolution of the system along the Sun-Earth direction will also be discussed. A brief comparison with observations and other related work will be presented. The same organizational scheme of our previous work will be adopted to easily explore the similarities and the differences in our work. Therefore, in each dimension, we present four images for the plasma density distribution taken at 1001, 1100, 1175 and 1250 Δt (see Figure 6.1, 6.2 and 6.3 respectively for the three directions previously considered). The corresponding four images of the field topology in each dimension are shown (see Figure 6.4, 6.5, and 6.6). For reference, figures are drawn in x-z plane at (x, y, z) = (155, 52, 105) Re, in x-y plane at(x,y,z)=(155, 105, 53)Re, and in y-z plane at (x,y,z)=(60, 105, 105)Re.

As in the previous chapters, the code was run for enough time (900 Δt) to establish the magnetospheric structure when a northern IMF (B_z=0.2) is steadily included. Then, a disturbance is applied during 100 Δt to generate the gap. The magnetopause variation in 3D measured from Earth position (at: x=60, y=52, z=53) Re as it responded to gap effect is then derived and analyzed. A particular attention will be paid to the onset of the expansion phase of the magnetopause and related processes. Final conclusion will draw attention to the effect of a solar wind depression on the dayside magnetopause when northern IMF is included, with brief comparison with our previous study cases of southern and zero IMF. With

the three main directions considered, we foresee that our theoretical model PIC simulations will help understand the magnetosphere response to a simple pressure force, to make predictions, and to build diagnostic tools that could be useful for future data comparison.

6.2 Plasma Distribution in Different Time Span along Noon-Midnight Plane

In Figure 6.1(A), taken at 1001 Δt, a gap is formed between 13Re and 28 Re along x direction. The gap size is almost the same as it was for both cases of zero and southward IMF discussed in chapter 4 and 5 respectively. Clouds of plasma in the tail are filling the formed cavity and feed the equatorial plane with **a** plasmasheet that has a variable thickness. It is worth to note that the location of the Van Allen belts is latent within this plasma layer in the nightside. Signature of a bow shock can be observed at 44-48 Re (12-16 Re from Earth position). Cusps are clearly seen nightside oriented. Lobes are observed almost parallel to the neutral line along x from 60 to 85 *Re***;** beyond this distance, they converge toward the neutral line with denser fillings of plasma up to 145 Re.

In Figure 6.1(B), taken at 1100 Δt, the downstream of the generated gap is now approaching the dayside magnetopause, and concaves over the magnetosheath as a cover. This cover has an apparent thickness along the x-direction of ~5.5 Re. The concavity of the flowing plasma is related to the fact that the dipole magnetic pressure is felt stronger on the Sun-Earth line of the gap downstream, whilst both ends (toward poles) proceed almost steadily along x. Inside the gap, clouds (blobs) of plasma are seen all over and are more uniformly distributed. Magnetopause stand-off position reads the value of ~12.52 *Re* in the x direction, compared with~13.5 *Re* for B_z=0 and ~12.3 *Re* for B_z<0. At the nightside, around 8 Re from the planet, a plasma sheet is formed. Bow shock is observed between 42 and 46 Re along x-direction. Both cusps are observed clearly and nightside shifted. Random distribution of plasma clouds is filling the magnetospheric cavity at the nightside.

In Figure 6.1(C), taken at 1175 Δt, the gap is apparently filled by plasmas with its downstream edge now almost located along the planet position (at: x=60, y=52, z=53) Re, while its upstream edge stands off at ~15 *Re*. By coincidence of the selected time, it seems that this distance traces also the stand off position of the magnetopause at the subsolar point. In previous chapters, at the same time duration, the magnetopause was broken up at ~15.4837 *Re* for B_z=0 but expands with no breaking up to ~17 *Re* for B_z<0. The magnetopause inner boundary is not seen smoothly curved; it seems that the particles entries into the inner magnetosphere (signature of reconnection) cause that discontinuity. The formation of a plasma ring around the planet is seen about~7 *Re* thick. Blobs of plasma observed at around 80 Re (along x-axis) could be plasmoid. Plasmoid usually formed as a result of reconnection from different orientation of IMF in the northern and southern lobes. They seemingly were dragged back by the air pocket effect and have the position x~58.7 Re, close to the planet position at x=60 Re. The cavity structure of the magnetotail can be seen along x down to ~110 Re (50 Re from planet). Beyond that distance, in contrast to the cases for B_z=0 and B_z<0, the magnetotail becomes filled up with plasma.

In 6.1(D), taken at 1250 *Δt*, the stand off position of the dayside magnetopause is now restoring its classical shape at ~10 *Re* (almost same with B_z=0 and B_z<0). The lobes are flared out due to the air pocket effect that hit their edges. The flared out upper/lower lobes almost extends from 36-72 Re along z. The magnetospheric cavity is occupied with low density plasma blobs up to ~110 Re along x. Plenty of plasma clouds accumulate in the cavity farther to this distance. The cusps are now more oriented nightward. A plasma ring around the planet is formed clearly and extended to ~5 *Re* in size nightward. It is remarkably clear that the magnetotail ceased to flare out at 74.9Re (~15Re from the planet position).

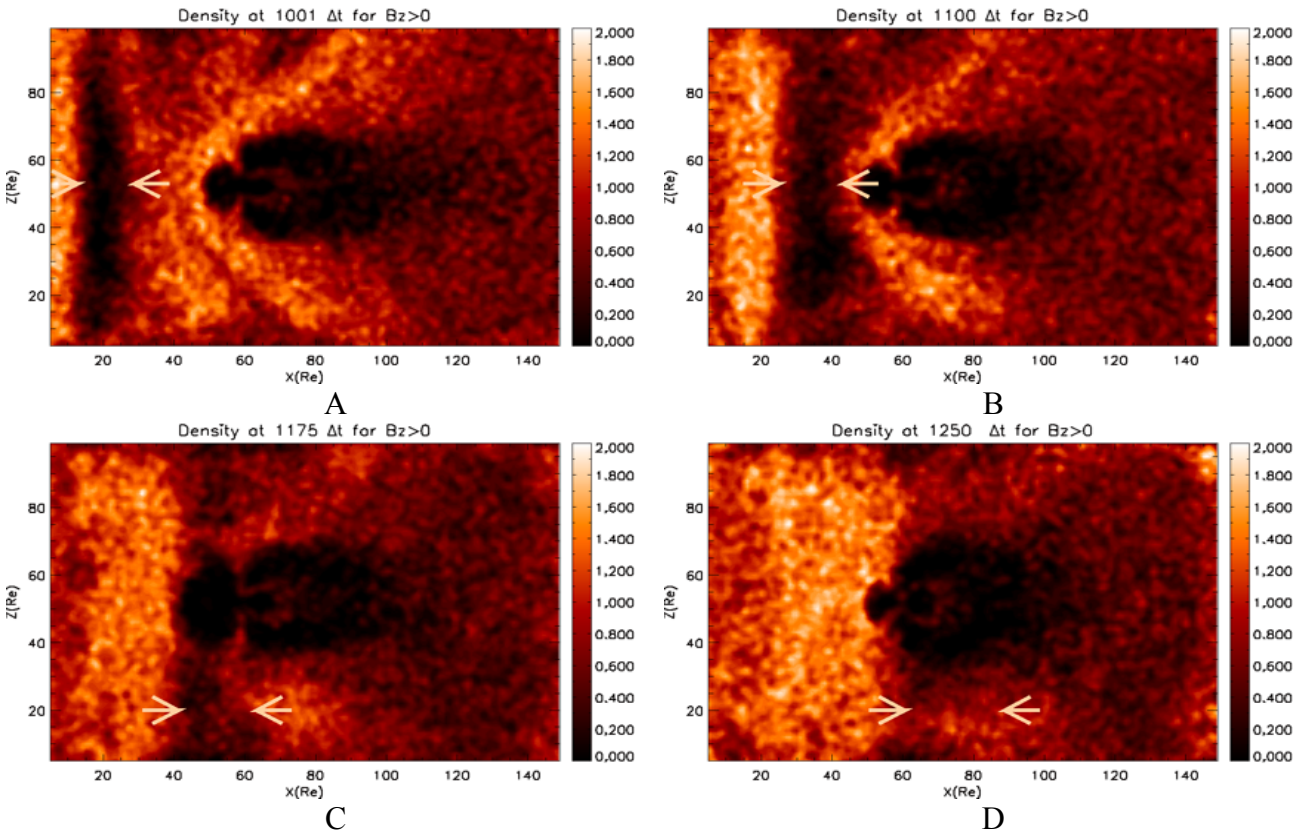

Figure 6.1. Time sequence of the response of Earth's magnetosphere to a depression (air pocket effect) in the incident SW flow for B_z>0. Plasma density is shown in panels A, B, C and D, taken at 1001, 1100, 1175 and 1250 Δt respectively. All plots are shown in the x-z plane located at y= 52Re and the gap position along x-direction is shown in figure between the two arrows heads.

6.3 Other examples of plasma distribution seen in different planes such as dawn-dusk and south-north directions

Two examples for the plasma distributions in x-y plane at z=53Re and y-z plane at x=60Re will be presented in this section to expand our view of the magnetospheric plasma behavior under the strong depression implied by the incident solar wind dynamic pressure.

First, we discuss the plasma distribution in the dawn-dusk direction as shown in Figure 6.2. In Figure 6.2(A) taken at 1001Δt, a gap indicated by the two opposite arrows in the figure is formed with a width of ~15Re. The bow shock can be seen at ~45Re. The trapped region plasma in the nightside around the planet has thickness of ~4Re. The convergence of the lobes in Figure 6.1(A) is confirmed in this figure and the filling of the plasma in the nightside is seen up to 140Re.

In Figure 6.2(B) taken at 1100Δt, the structure of concave plasma band, previously shown in Figure 6.1(B), is now seen more concave sideway at the dayside of the magnetopause. The magnetic pressure of the dipole fields superimpose over magnetic pressure of the northern IMF at the subsolar point, thus producing a resistance that decelerates plasma downstream of the incident gap. The plasma trapped region is expanded out to 10Re in size nightward with its radius of curvature is seen reduced. The far magnetotail boundary is seen dragged inward toward the planet; it seems that a reconnection took place in a region bounded along the x-direction from x=115Re out to 145Re. This figure also shows same observations made by Nishikawa, Neubert and Buneman (1995), where the magnetotail was shifted toward south and its length is shortened. This result is consistent with occurrence of the magnetic reconnection at the high latitude mantle. Due to the more effective reconnection at the north side, more plasma move into from that side, therefore the distant magnetotail move toward south shortening its length.

In Figure 6.2(C) taken at 1175Re, the magnetopause inner boundary and the trapped region (located at 8Re on the nightside of the planet) form a rough magnetospheric circular cavity in the equatorial plane. Additionally, at both dawn and dusk direction around the boundary of the

magnetosphere and within the boundary of the gap, a dense plasma blobs is accumulated. Moreover, this accumulation of plasma is lessened as distance increases in both directions (dawn and dusk) away from the planet. At 113Re in the nightside, a sort of plasma walling is formed vertically along z-direction; comprising within its boundary and in both lobes a random distribution of plasma blobs.

In Figure 6.2(D) taken at 1250Δt, as soon as the gap passes over the planet position, the magnetopause roughly recovers its position. Further more the gap is almost filled with plasma. Moreover, the magnetotail becomes more confined with a conic shape that has a base located at planet position and its apex is filled up by plasma blobs at x=117Re. Additionally, the trapped region at the night side seemingly reduces in size.

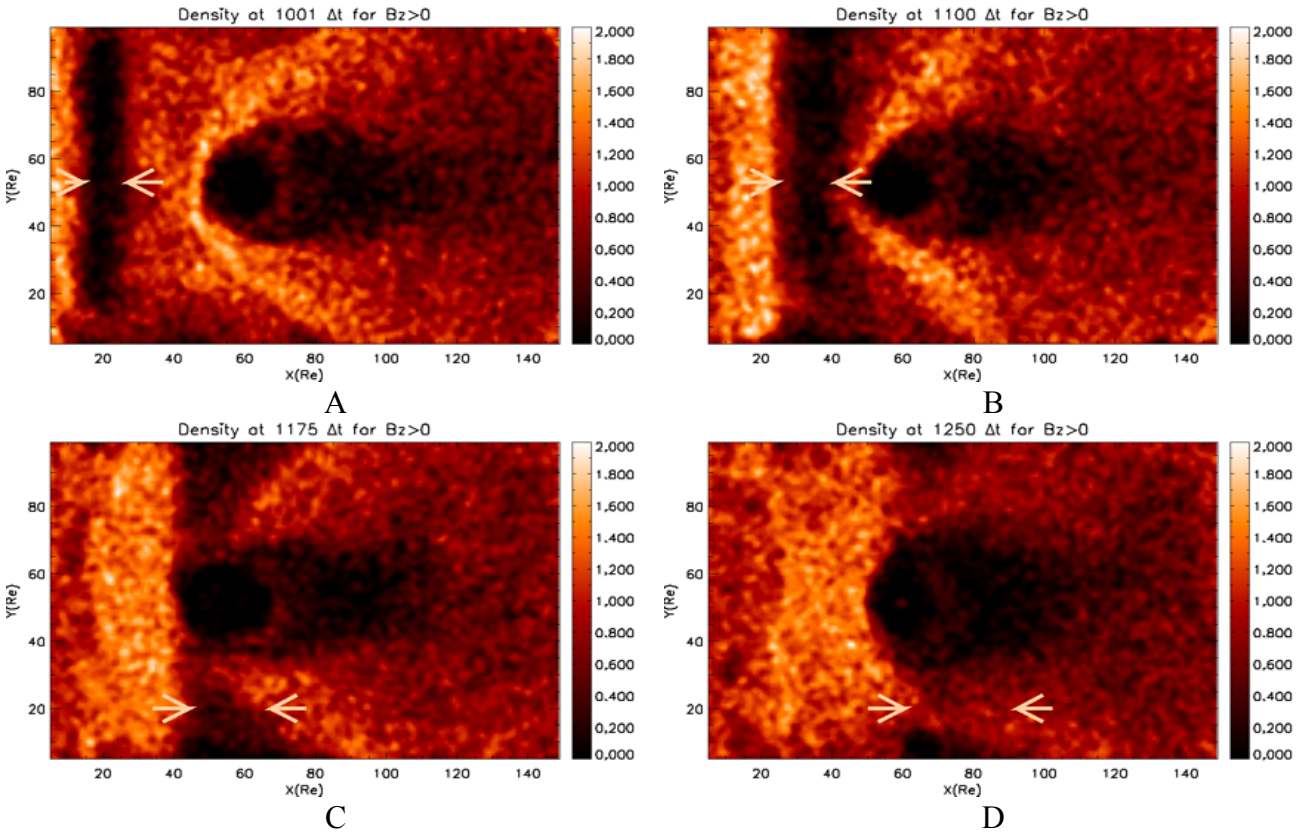

Figure 6.2. Time sequence of the response of Earth's magnetosphere to a depression (air pocket effect) in the incident SW flow for B_*z*>0. Plasma density is shown in panels A, B, C and D, taken at 1001, 1100, 1175 and 1250 *Δt* respectively. All plots are shown in the x-y plane located at z= 53Re and the gap position along x-direction is shown in figure between the two arrows heads.

As a second example, we consider the plasma distribution in the south-north direction (y-z plane at x=60Re). In Figure 6.3.a (A) taken at 1001Δt, the magnetospheric cavity has an oval shape with its narrow part pointing toward dawn. Inside the cavity, C-shaped plasma band on the dawn side of the planet is seen. This C-shaped band is seemingly related to particles entry through the flanks in the dawn direction.

In Figure 6.3.a (B) taken at 1100Δt, at this time the magnetospheric oval shape is modified in terms of shape and particles distribution inside it. Particularly, this magnetospheric oval cavity is zoomed-in between y=[25, 79] and z=[20,79] as shown in Figure 6.3b, to better illustrate the particles

entry regions around the cavity. Potential particles entry regions (flanks/cracks…etc) are pointed out by the white arrows shown in Figure 6.3b. These regions correspond to where the magnetic field's lines, which are shielding the planet, are subject to reconnections that cause 'openings' in the cocoon around the planet; as a result particles penetrate into the inner magnetosphere.

In Figure 6.3.a(C) taken at 1175Δt, the magnetospheric cavity is now filled with blobs of plasma. The doughnut shape plasma inside the cavity is squeezed from both north and south direction above and below the planet position. The gap can be tractable at the very far boundary of the box at dawn and dusk directions.

In Figure 6.3.a (D) taken at 1250Δt, the oval shape, previously shown in figure 6.3.a (A), appears now in a reversal order, with the narrow part of its elliptic shape pointing toward dusk. The northern and the southern cusps are seen dawn oriented. At this time step, the magnetopause length in y-direction reads the value of 15.73Re. Moreover, a zoomed view of the magnetospheric cavity, reveals that at the dawn side of the inner magnetosphere, there are two opposite arcs of plasma configuration extended out from 51Re (~1 Re from the planet) to 36Re along x-direction.

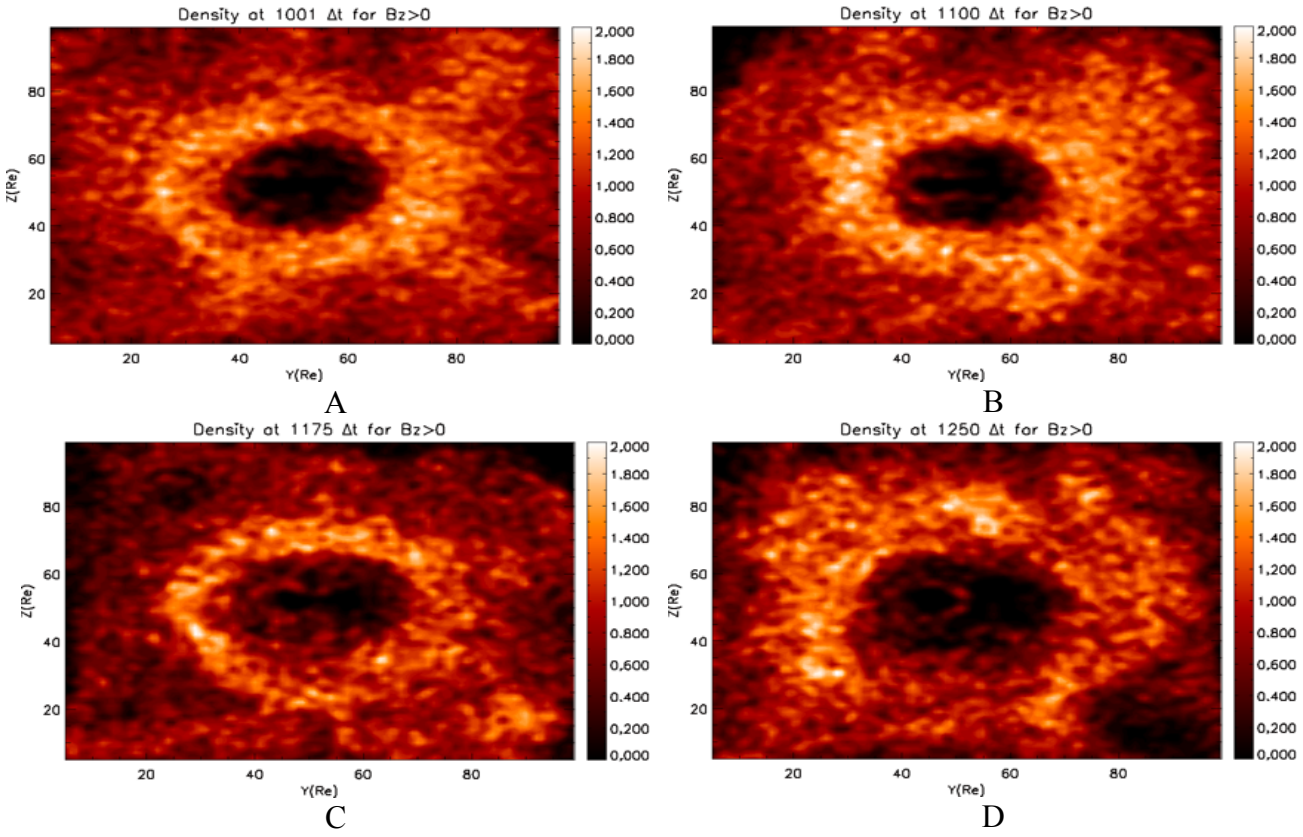

Figure 6.3.a Time sequence of the response of Earth's magnetosphere to a depression (air pocket effect) in the incident SW flow for B_z>0. Plasma density is shown in panels A, B, C and D, taken at 1001, 1100, 1175 and 1250 *Δt* respectively. All plots are shown in the y-z plane located at x= 60Re.

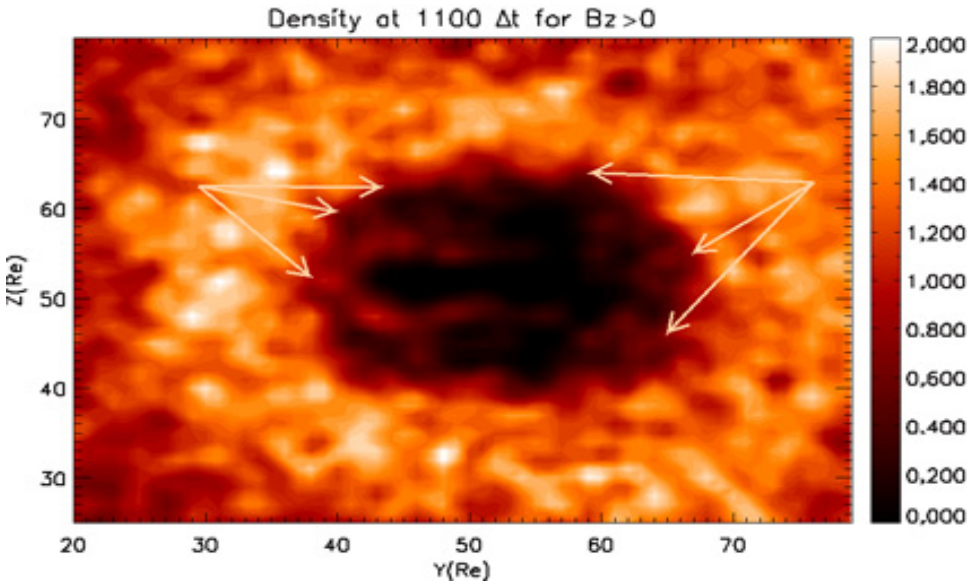

Figure 6.3.b Zoomed-in plasma distribution between x= [20, 79] Re and z= [25, 79] Re, in the y-z plane at x=60 Re. White arrows show some of the potential regions at the magnetospheric cavity through which particles enter inside the inner magnetosphere.

6.4 Field Lines topology in different time span along noon-midnight plane

In the previous section, we discussed the response of the magnetosphere to a disturbance in the solar wind flow under northern IMF condition, in terms of plasma 3D distributions. In the same context, we go forward to discuss the corresponding field's lines topology in 3D.

In Figure 6.4(A), taken at 1001 Δt, the field's lines topology, that corresponds to the plasma distribution of Figure 6.3.a (A), is shown. The northern IMF field lines are superimposed to the dipole field lines, thus strengthening them. Accordingly, the magnetic field's lines at the magnetopause are closed. Further more, at ~44 Re along x-direction, one can see a concave stripe of dense field's lines around the dayside magnetopause, evidently revealing the signature of the Earth bow shock. At the same time, at the lower side of the simulation box about~ 45-90 Re along x, distorted field's lines

(instabilities) are seen. We don't know exactly what physical processes are behind these distorted lines. Admittedly, these lines are real, may be future similar work will disclose the reason, why these lines are produced at this region and what causes them? Another important piece of information can also be drawn from Figure 6.4(A), which is the existence of an X-point that is located roughly at around ~110 Re. By comparison, the corresponding location of the X-point that appeared after the same duration of time was respectively at 80 Re for B_z<0 (chapter 5) and 103 Re for B_z=0 (chapter 4). Therefore, the effect of northern IMF in the solar wind-Earth magnetosphere interaction, generate a field's topology with x-points located more distant nightward than in zero and southern IMF.

In Figure 6.4(B) taken at 1100 Δt, the superimposed northern and dipole field's lines shield out the magnetopause nose which is seen at~ 11 Re on the dayside. However, in the northern cusps region, the field's lines are open. On other hand, the previously obtained X-point sustains its position at 110 Re. Deeper in the nightside around 40 Re from the planet position, the field's lines constellated in a manner that seemingly related to a potential reconnection. The distorted field's lines mentioned in figure 6.4(A) not only appear in this figure but changing position as well. In addition, we notice that the magnetopause expands sunward along the x-direction.

In Figure 6.4(C), taken at 1175 Δt, the position of the downstream boundary of the gap falls together with the inner magnetospheric cavity. Coincidently, the field's lines of the inflated magnetopause are almost tangential to the upstream of the air pocket boundary. The drift in the position of the plasma distribution in the magnetotail to the south as shown figure 6.1(C), is also clearly seen in this figure for the field's lines topology.

In Figure 6.4(D), taken at 1250Δt, as the depression effect over passes the planet position, the dayside magnetopause restores its position at around ~10 *Re*. It is praiseworthy to see that the field lines are larger (in comparison to that before the disturbance effect was applied) at the standoff distance

of the subsolar magnetopause. Further to what was observed at figure 6.1(D) where the magnetotail ceased to flare out at 15Re from the planet position. In conclusion, this result is consistent with the work of Chen et al., (1993), where a similar observation by ISEE 1 and 2 spacecraft was attained.

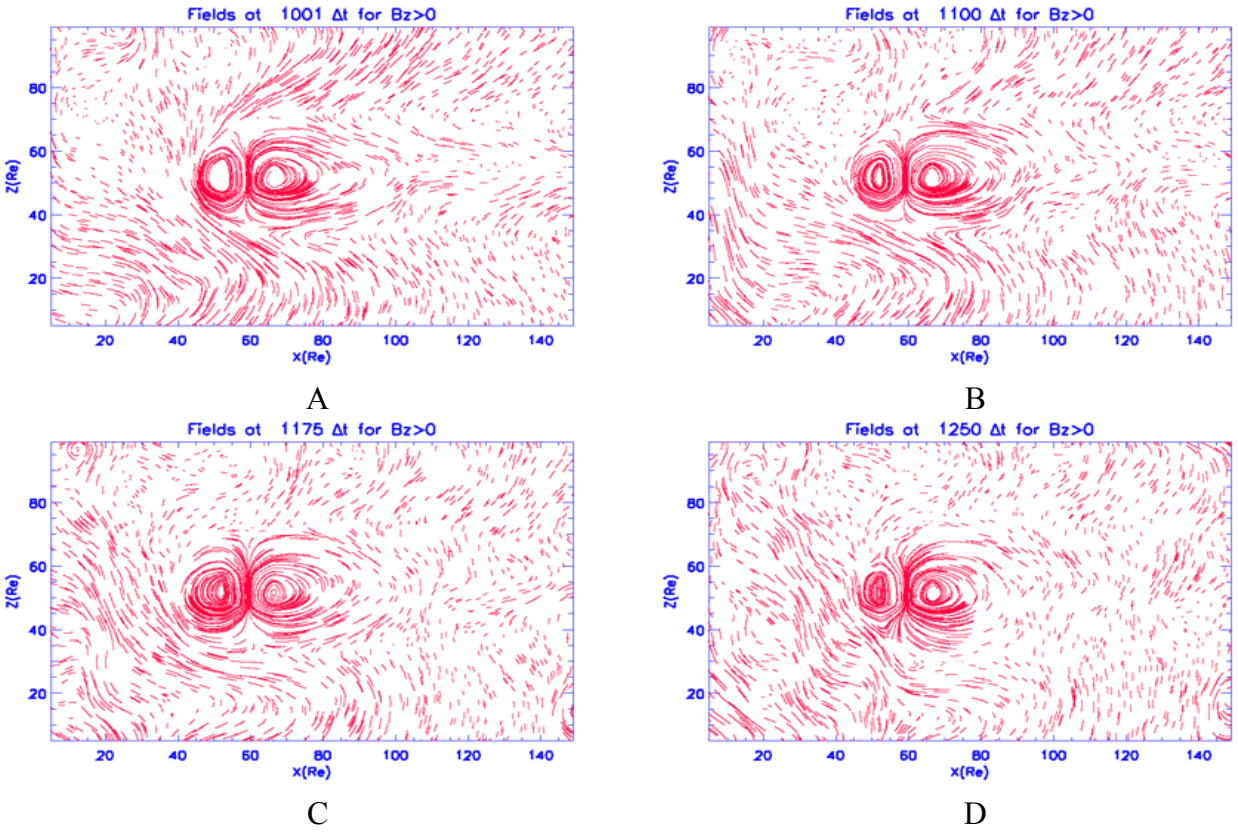

Figure 6.4. Time sequence of the response of Earth's magnetosphere to a depression (air pocket effect) in the incident SW flow for B_*z*>0. Field lines are shown in panels A, B, C and D, taken at 1001, 1100, 1175 and 1250 *Δt* respectively. All plots are shown in the x-z plane located at y= 52Re and the gap position along x-direction is shown in figure between the two arrows heads..

6.5 Other examples of field's lines topology in dawn-dusk and south-north directions

Further to the intrinsic structure of this chapter, we now present two examples of field's lines topology in dawn-dusk and south-north directions. As a first example, the field's lines will be described in the x-y plane at z=53Re. In Figure 6.5(A) taken at 1001Δt, the dipole lines, within the vicinity of the magnetospheric cavity, are radiantly spread out mainly toward dawn-dusk direction. Besides that, the magnetotail is slightly mapped by distorted low-density field lines extending out to 120Re. Similarly, the instabilities shown in Figure 6.4(A) in the x-z plane have also a signature in the equatorial plane and can be seen all around the planet.

In Figure 6.5(B) taken at 1100Δt, the structure of the field's lines topology in this figure reflect what the plasma density in Figure 6.2(B) showed through the pressuring of the magnetopause Earthward, Accordingly, the field's lines are diverted toward the dusk direction around (x, y)=(48,60)Re. Also, on the nightside, the field's lines do not show a regular structure outside x=83Re, forming unmapped zone, before appearing again in irregular structure beyond x=105Re.

In Figure 6.5(C) taken at 1175Δt, despite the fact that the disturbance (gap) is localized inside the inner magnetosphere at this particular time step, the outward radiant field's configuration are clearly seen around the dipole. Furthermore; at the nightside the field's lines are not easily tractable at this particular time in the equatorial plane.

In Figure 6.5(D) taken at 1250Δt, as soon as the gap over passed the planet position, more violent instabilities are appearing on the dayside, and the field's lines of the dipole are tractable nearby the planet, but not at the magnetotail. In the following, the corresponding south-north plane will better describe the field's lines at this particular time.

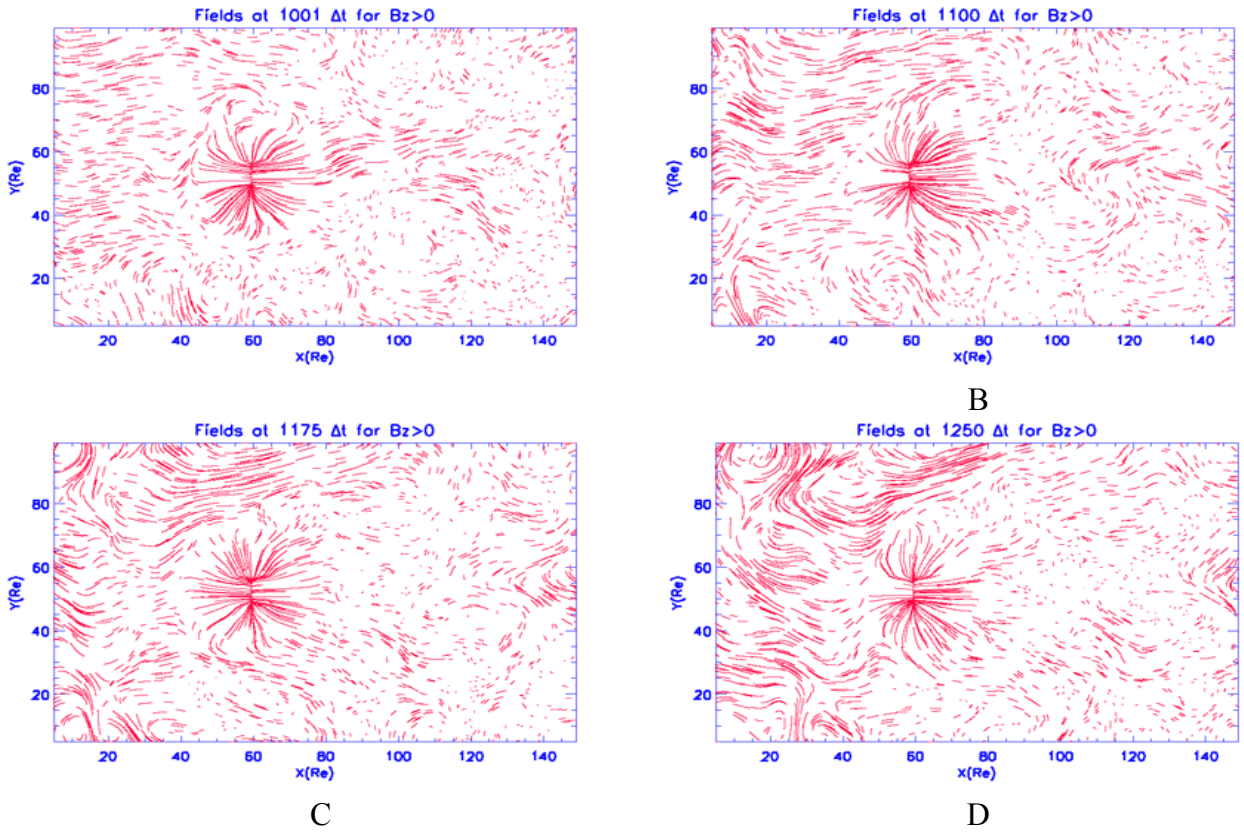

Figure 6.5. Time sequence of the response of Earth's magnetosphere to a depression (air pocket effect) in the incident SW flow for B_z>0. Field lines are shown in panels A, B, C and D, taken at 1001, 1100, 1175 and 1250 *Δt* respectively. All plots are shown in the x-y plane located at z= 53Re and the gap position along x-direction is shown in figure between the two arrows heads..

As a second example, the field's lines topology will be presented in the y-z plane at x=60Re, corresponding to the Earth's position. In Figure 6.6(A) taken at 1001Δt, the northern IMF on both sides of the magnetospheric cavity (along y-direction) apparently confines the dipole field's lines at this particular time step (very much like a cocoon). On the other hand, the field's lines at the northern and southern cusps are seemingly dawn oriented.

Sequentially, the field's lines in Figure 6.6(B) taken at 1100 Δt, are apparently inflated along the z-direction in the dawn side of the planet, and more confined and denser at the dusk side of it. Further more, the magnetic field's lines that shield the planet are subject to reconnections with the

northern IMF; which in turn cause ‘openings’ in the shield configuration (a signature of reconnection appears at the southern part of the planet at (y, z)=(63,39)Re). Consequently, this is consistent the with corresponding plasma distribution shown in Figure 6.3.a (B)

In Figure 6.6(C) taken at 1175Re, as it has been earlier shown in figure 6.3(C) that the inner magnetospheric cavity is filled with blobs of plasma particles, evidently the opened field’s lines at the dawn direction is the potential gateway for plasma blobs entry. Accordingly, these particles entry are probably partially related to a potential reconnection at the dawn side flank of the magnetosphere. In the mean time, the northern and the southern cusps field’s lines are driven dawn side.

In Figure 6.6(D) taken at 1250Δt, as soon as the depression effect is over passing the dayside magnetopause, the dipole field’s configuration at the dawn side is seen flared out, while it is more confined inward at the dusk side. In addition, the field’s lines that are closer to the planet position are apparently closed. In the cusps regions, the field lines show a dawnward orientation. Furthermore, this orientation of the cusps is accompanied by dense particles entries inside the inner magnetosphere.

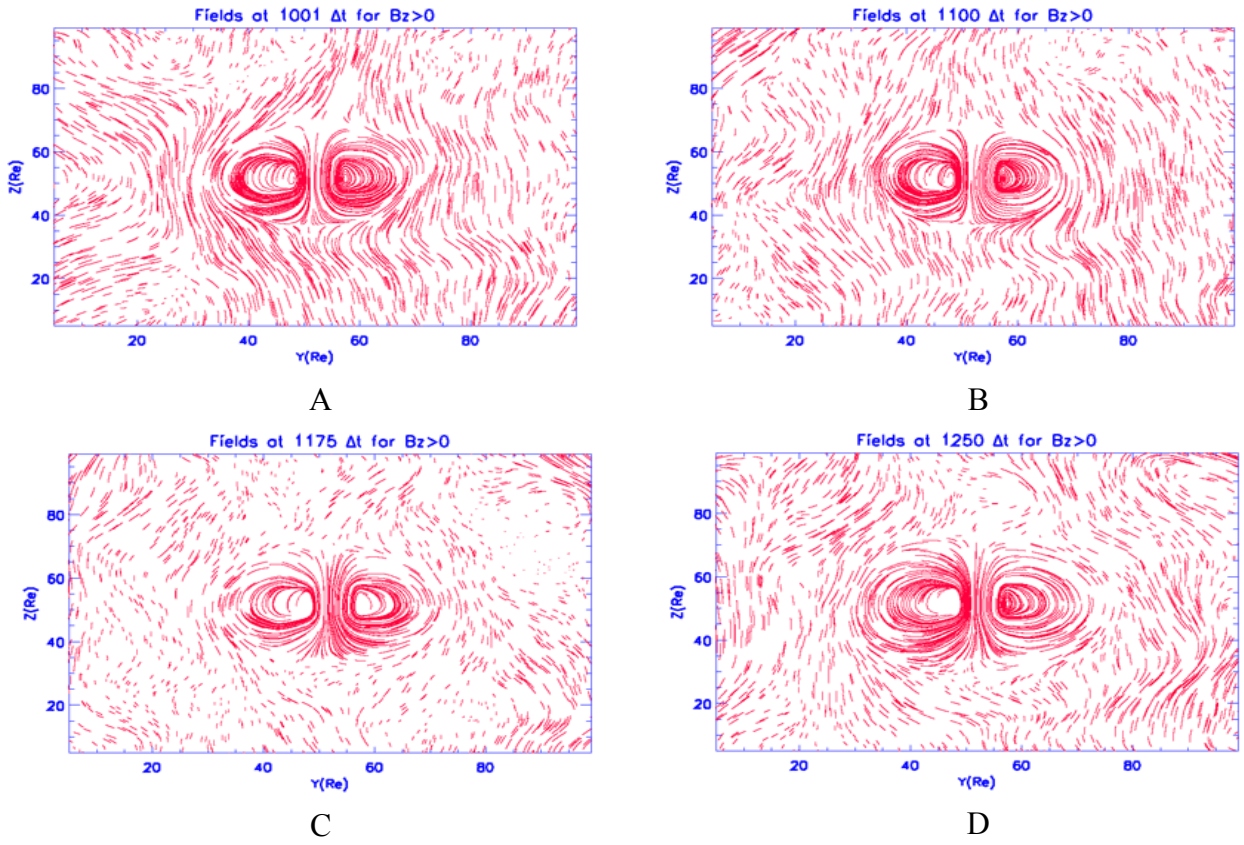

Figure 6.6. Time sequence of the response of Earth's magnetosphere to a depression (air pocket effect) in the incident SW flow for B_z>0. Field lines are shown in panels A, B, C and D, taken at 1001, 1100, 1175 and 1250 Δt respectively. All plots are shown in the y-z plane located at x= 60Re and the gap position along x-direction is shown in figure between the two arrows heads.

6.6 Analysis and comments

In Figure 6.7, the expansion/recovery phases of the magnetospheric system are shown when B_z>0. Panels A, B, and C represent the magnetopause (MP) size along x (from Earth), y (dawn to dusk), and z (south to north), respectively. We remind that x represents the Sun-Earth line (at: y=52, z=53) *Re*, y represents dawn-dusk line (at: x=60, z=53)*Re*, and z represents south-north line (at: x=60, y=52) *Re*, (no tilt is assumed).

In Figure 6.7(A), as a consequence of the abrupt decrease in the solar wind ram pressure, the magnetopause expands. In the beginning, the magnetopause starts expanding from 11Re up to 13Re (~2 Re) between 1099 and 1107 Δt, then it shrank from 13Re down to 12Re between 1107Δt and 1115Δt. Subsequently, the MP linearly expands from the former position up to ~20 Re, a size that it reached at about 1160 Δt. Apparently the system then relaxes for 6 Δt, before the MP starts contracting, thusly entering the recovery phase. The recovery phase starts as soon as the upstream edge of the air pocket hits the expanded nose of the magnetopause. The MP then recovers linearly its undisturbed size that it attains at 1212 Δt.

In Figure 6.7(B), we report the expansion rate of the magnetopause size in the y-direction when B_z>0. The onset position of the MP in y-direction reads the value of ~13.3 Re. Soon after the nose of the magnetopause starts expanding in response to the air pocket effect, the magnetopause shrinks at dawn-dusk direction during the time interval between 1000 and 1101 Δt. During this contraction, the MP reached its minimum size ~9.222 *Re* at 1050.78 Δt. In order to understand this phenomenon, we propose in the following the model of elastic magnetic field's lines. Figure 6.8 shows the scenario to illustrate the onset of the expansion phase of the magnetopause in the y-direction. In that figure, curve

1 (green dashed curve) represents the magnetopause "stand off" position before expansion. Curve 2 (red dotted curve) represents the onset of the expansion phase that started along the x-direction while delayed in the y-direction for ~100 Δt. Curve 3 (blue dashed dotted) represents the response of the MP to the air pocket effect in the y-direction. In conclusion, the whole scenario resembles a U-shaped rubber band that is fixed at the ends, while pulled out from the concave part, and then stretched from the walls sideway. To sum up, during the onset of the expansion in dusk direction, the magnetic field's lines behaved like an elastic rubber band. Further to the process described above, the MP nonlinearly expands from 13.4 to 27.27 *Re* between 1101.27 to 1165.7 Δt. Once the gap effect approaches the magnetopause, the effect of northward IMF seemingly hinders the MP expansion/recovery, where the system relaxes from 1166 Δt until 1223.2 Δt. Afterward the system recovers very fast as the effect is over at 1235.7042 Δt.

In Figure 6.7(C), the expansion/recovery of the magnetopause in shown in the z-direction. In contrast to aforementioned directions, at the onset of the expansion, the MP size remains relatively stable at ~ 19 *Re* from 1000 Δt up to 1136.8599 Δt. Obviously, the air pocket effect is still relatively far to be felt by the MP boundary at z-direction. Moreover, the system expands linearly out to 28.555 Re at 1190.69 Δt, before it relaxed until 1228 Δt (~37 Δt). The recovery phase is linearly attained when the MP reached its initial position (19 Re) at about 1240 Δt.

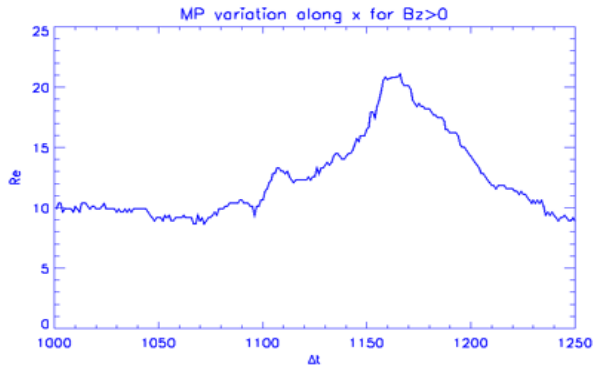

A

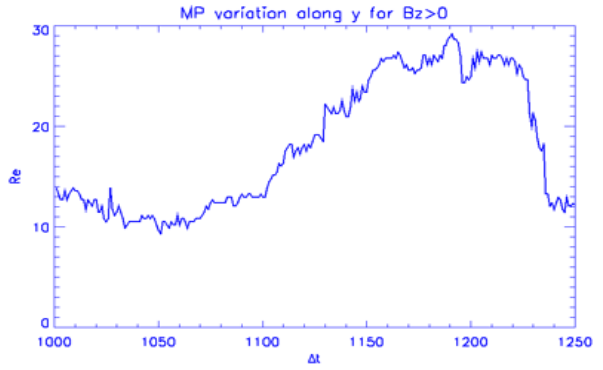

B

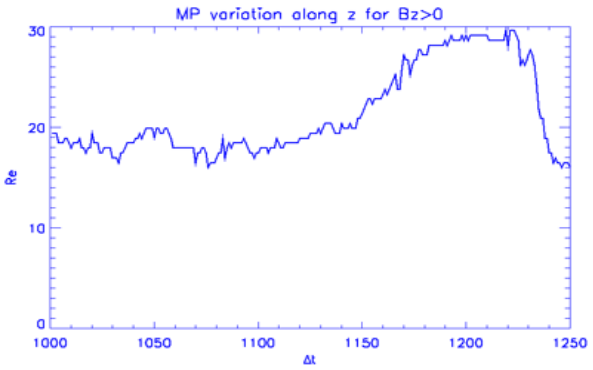

C

Figure 6.7 Magnetopause expansion measured from Earth location (x=60, y=52, z=53)*Re* in 3D; x, y and z for B_z>0 at panels A, B, and C respectively

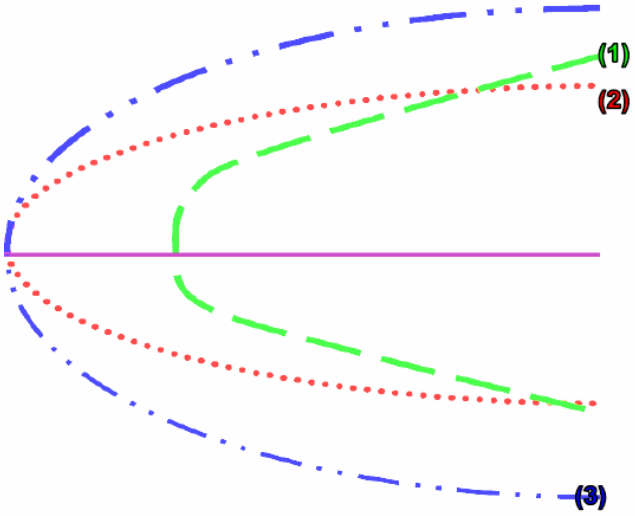

Figure 6.8 this sketch describes the model of elastic magnetic Field lines during the expansion phase in y-direction. Curve 1 green-dashed represents the MP balanced position in xy-plane at z=53Re, before the expansion took place. Curve 2 red-dotted, expansion took place on x-direction but time-delayed in y-direction. Curve 3 blue-dashed-dotted represents the response of the MP in y-direction to the air pocket effect.

6.7 Conclusion and Remarks

In this chapter, we studied the impact of a solar wind depression (air pocket effect) on the dayside magnetopause during the northern IMF, a follow up to two case studies for the absence of IMF (chapter 4) and southern IMF(chapter 5). Our conclusions are the following:

The generated gap due to the simulation of the depression in the solar wind has a comparable size ~15 Re to the one obtained with of B_z<0 and B_z=0. More dense plasma populates the cavity at the magnetotail which results in tail shift to the south (figure 6.1 (C)), which by turn is a sign of reconnection at that region. For the magnetopause expansion rate, the MP expands along x-direction with speed equal ~ 0.18 (a solar wind speed of 0.25 corresponds to a bulk velocity of the SW of ~500 km/s) corresponding to an equivalent velocity of 360 $km.s^{-1}$, and recovers at a speed rate equal ~0.16 (~320 $km.\ s^{-1}$). On the other hand, the rate of the MP expansion along y-direction is 0.177 (~354 $km.s^{-1}$) and the corresponding recovery speed is ~0.31 (~ 620 $km.s^{-1}$). Moreover, the expansion rate as seen in the z-direction shows a speed around 0.12 (~ 240 $km.\ s^{-1}$), whilst the corresponding recovery speed reads the value ~0.45 (~900 $km.s^{-1}$). In conclusion, the expansion phase in x-direction is the fastest compared to the expansion in y and z-direction; because the subsolar point of the magnetopause is closest to the generated disturbance than the other two boundaries in y and z-directions. On contrary, the recovery phase of the magnetopause in y and z-direction is very much faster than that at the x-direction. The evidence is that: the disturbance is effectively generated as a planar cut along x-direction, therefore the elapsed time for the gap to over pass the magnetopause along x-is longer than that elapsed along y and z.

Orientation of the cusps is less affected by the depression in the solar wind flow during the northern IMF than the two case studies in chapter 4 (no IMF) and 5 (southern IMF). Particles entry in the dawn direction shown in Figure 6.3(C) is believed to be caused by a reconnection at both southern and northern cusps. In Figure 6.8, a model of elastic magnetic field lines is proposed to explain the contraction at the onset of the expansion phase of the MP along the y-direction.

Chapter Seven

Code application on analysis of the October 2003 solar activity event using ACE data.

7.1 Introduction

For reference purpose, we remind that the Particle-in-cell (PIC) code considered in this work has been extensively used before by Buneman (1992, 1993, and 1995), Nishikawa (1995, 1997, 1998, 2000) and Cai et al (2003, 2006) under different versions. In this thesis project, we use an evolved version that has been developed by a French-Polish team (Ben-Jaffel et al., 2006). The code structure and its basic elements are described in chapter 2. We tested its validity as described in chapter 3. Then the code was used in three case studies to simulate the impact of a depression (air pocket) in the solar wind flow on the macrostructure of the Earth's magnetosphere during the absence of IMF (chapter 4), the southward IMF (chapter 5) and the northern IMF (chapter 6). By doing so, we intended to separate effects and study them individually. So far we didn't include ionosphere in our simulation, but we will consider that improvement in the future work. The conclusion of these case studies is that the code effectively simulated the macrostructure of the Earth magnetosphere, including the magnetopause, magnetotail, as well as the drop in the dynamic pressure (depression) of the solar wind flow. Moreover, signatures of reconnection, and other dynamical structures in the day and/or night side, such as vortices, erosions and multiple X-points were successfully obtained by the code. The time response of the magnetosphere to the air pocket disturbance was then derived in 3D along the main axes, namely the noon-midnight, the dawn-dusk and the south-north directions.

The output of the aforementioned applications is now used as a prototype model to expand our experiments to simulate the response of the magnetosphere to real solar wind data. We contacted the Advanced Composition Explorer (ACE) science center at Caltech (A. Davis and R. Skoug) who thankfully provided us with processed data from ACE. The ACE spacecraft is carrying six high-resolution sensors and three monitoring instruments samples low-energy particles of solar origin and high-energy galactic particles with a collecting power 10 to 1000 times greater than past or planned experiments (http://www.srl.caltech.edu/ACE/).

The violent solar eruptions of October-November 2003 and are one of the best observed outbreaks of intense solar activity to date. These events, referred to as the *Halloween* storms, are extreme events in terms of both their source properties at the Sun and their heliospheric consequences. The plasma, particle, and electromagnetic consequences of these events were detected at several locations in the heliosphere thanks to the distributed network of spacecraft (Gopalswamy, et al, 2005). Three components of the ACE data of the solar wind flow are used in our task, namely the number density (N_sw), the bulk velocity (V_sw) and the Interplanetary Magnetic Field in the z-direction (IMF). The resultant total pressure (magnetic and dynamic) of the solar wind flow is then derived and all components are shown in Figure 7.2.a. This data is measured by ACE at 1AU every 64 seconds. The data have been scaled to a constant time of ~3.36 seconds corresponding to 1 Δt of our code's time scale, so that it requires to the code to run almost 19 Δt time steps under the same ACE input.

To simulate the impact of the Halloween event, the macrostructure of the magnetosphere was first established based on the same procedure adopted in chapters, 4, 5, and 6. The system was left to evolve for 900 Δt, by using the solar wind bulk velocity along the x-axis and the IMF z-axis component from one side, and the planet dipole magnetic field from the other side. Consequently, during the

application of our code to the ACE data, we only used the B_z, Vsw_x and the particle density from their data profile versus time. Later we noticed that the code cannot manage strong and abrupt changes in the components of the incident solar wind parameters (IMF field strength, bulk velocity, density, etc). Previously, in all our case studies, we held the SW density constant and then supplied south/north IMF as a steady flow all over the simulation box. As shown in Figure 7.2.a, with the ACE data, it is not any more the same case. Fortunately, we succeeded to simulate few hundreds of step times of the ACE time variable solar wind flow impact on the Earth's magnetosphere. The density distribution in the noon-midnight sector is shown in Figure 7.1 at four time steps since the variable flow hit the left side of the simulation box. The corresponding field's lines topology is shown in figure 7.3. We believe that the whole event can be globally simulated with an extended and denser grid and a larger number of pair-particles loaded in the simulated box. In fact, several factors make it difficult to carry out this task all the way out to simulate all the available ACE data. First, lack of computer resources as we only use one 4-processors machine, and limitation of data storage capacity. For example, each binary file to describe one step time consumes a size of ~100 MB. To carry out the whole event we need to compile almost 6390 files for particles, and same number for fields, before reading and analyzing this data by IDL to generate the output images (each IDL output needs a space of ~50 MB). The total required space exceeds a terabyte, a space that was not available at the time of this thesis project. This task could be however a good research project for future or post-doctoral work if faster computers and few terabytes disk storage are available.

In the following, we present four images in x-z plane taken at y=52 for plasma distribution (Fig. 7.1) and their corresponding field's lines topology (Fig. 7.3) taken at 920, 1015, 1091 and 1186Δt. Then we briefly add our concluding remarks leaving discussion and analysis of the results to chapter 8.

7.2 Simulation of the magnetosphere response in terms of plasma distributions to the abrupt solar event observed during the solar activity on October, 2003.

The plasma distribution corresponding to the solar activity during Oct. 2003 is presented in Figure 7.1, in noon-midnight plane (x-z plane: at y=52Re). In Figure 7.1(A) taken at 920 Δt, which is the first step time when the ACE data is applied. At this particular time the macrostructure of the magnetosphere is well established. The magnetopause size at the x-direction reads the value of 10.4 Re. Moreover, on the dayside, a signature of the Earth's bow shock is seen at 42-44 Re along x-direction, while both south and north cusps are clearly seen and nightside drifted. Furthermore, the trapped region in the nightside seemingly extends from 66-70 Re along x-direction. Worthy to report that, the structure of the lobes as they are observed is consistent with the typical lobes structure when a southward IMF is applied in the system. At the magnetotail there is seemingly dense plasma blobs randomly distributed starting from x=90Re out to the boundary of the simulation box.

Later on, in Figure 7.1(B) taken at 1015Δt, the cusps are seen almost at the same position as they appear in the previous case. In addition, the magnetopause stand off position reads the value of ~10Re. A gap is observed as a double curvature cut between 19Re and 35Re along x-direction. Additionally, the plasma density at the downstream boundary of the gap is denser than its upstream one. This is exactly the opposite case of what we saw in Figures 4.1(B), 5.1(B) and 6.1(B), where the upstream boundary of the gap is denser than downstream boundary of the gap. In other words, Figure 7.1(B) demonstrates new classes of disturbances that are not created this time as a result of the abrupt change in the bulk velocity of the SW flow considered in previous chapters, but rather related to the strong IMF input value (southward oriented).

To realize the aforementioned difference between the case studies (chapter 4, 5, and 6) and the current application, we present the following analysis of the solar wind injection in the simulation box

versus time. As the time goes on, SW particles move in the box as layers orthogonal to the x-direction of different properties (density, bulk velocity, IMF). For example, at the time 1015Δt, the SW plasma penetration in the box translates to a spatial distribution within the box between 0 out to 35 Re as shown in Figure 7.1(B). Figure 7.2.b (up to Δx=35 Re) shows the density input profile (pink color), the scaled solar wind velocity input profile (green color), the IMF input profile (red color), and the local value of the IMF (blue color) inside the simulation box. Apparently, the dramatic jump in the input IMF (compared to B_z=-0.2, the IMF value that has been used for our starting model; see chapter 5 for example) causes the gap to form. This strong jump (x-direction) in the southward IMF strength generates a duskward (y-direction) magnetic force, which in turn sweeps sideway the plasma. This is indeed confirmed by the velocity field in the y-z plane at the position of the gap around x=35 Re. In conclusion, the IMF is the key input parameter that causes the strong disturbance in the plasma flow, as the solar wind density and velocity don't have a differential significance to cause either compression or depression in the plasma flow. Surprisingly, when compared to the description Sibeck et al. (1999) of a hot flow anomaly formation, we found similar ingredients to produce our air pocket with the ACE data. Indeed, Sibeck et al. advocated a tangential discontinuity that interacted with the Earth bow shock that itself produced an HFA in the magnetosheat, a rarefied space that allowed the magnetopause to expand as far as 5 Re from its nominal position. Our simulation results go in the same direction. The nice result obtained here is that our code produced a rarefied space by the only application of a huge gradient in the impinging IMF! The gap produced here may be the equivalent of an HFA as reported by Sibbeck et al., 1999 or investigated later by Omidi and Sibeck, 2005, 2007. Further investigations are still need to validate this claim by a direct comparison to existing data. Worthy to note that the jump is caused by our decision to have IMF=-0.2 before injecting the ACE data with an IMF starting at -1.2. These new class of disturbances should be studied more carefully in the future.

Worthy to note that the jump is caused by our decision to have IMF=-0.2 before injecting the ACE data with an IMF starting at -1.2. These new class of disturbances should be studied more carefully in the future.

In Figure 7.1(C) taken at 1091Δt, the gap advances earthward along x-directions keeping almost the same shape. The downstream boundary of the gap is shaped such that it concaves over the nose of the magnetopause (a thickness of ~4 Re), while on the other hand it stretches out along the south (at: x=52 Re) and the north (at: x=54 Re) directions. Furthermore, the upstream of the boundary of the gap, located x=16 Re, has a layer of low density plasma blobs distributed between x=16 and 34 Re. The magnetopause stand off distance reads 9.5Re. Another aspect of the magnetospheric structure is that the northern and southern cusps apparently grow thicker and extend closer to the planet position with an approximate upright orientation. On the other hand, the trapped region in the nightside of the planet is monitored at x=65 Re with a relative thickness of ~3Re. Moreover, the lobes are flared out, a shape that characterizes the configuration of magnetospheric structure when a southward IMF is included. The magnetotail, seemingly, is filled by plasma clouds with a plasma sheet that has variable thickness along the neutral line.

In Figure 7.1(D) taken at 1186Δt, the downstream position of the disturbance over passes the planet position in a curvilinear manner, at both far northern and southern hemisphere. Seemingly, the standoff position of the magnetopause is no longer seen, an indication of the effect of the induced magnetic force. On the other hand, the upstream edge of the generated gap can be observed at x=31 Re with a random boundary configuration. Moreover, the cusps are seen thinner at this particular time and having a nightside orientations. At the nightside, the magnetospheric configuration suggests that the total pressure inbounds the plasma toward the neutral line, where the lobes compacted inward as we

move tailward. We demonstrate also the extensive fillings of plasma clouds inside the magnetospheric cavity at the magnetotail.

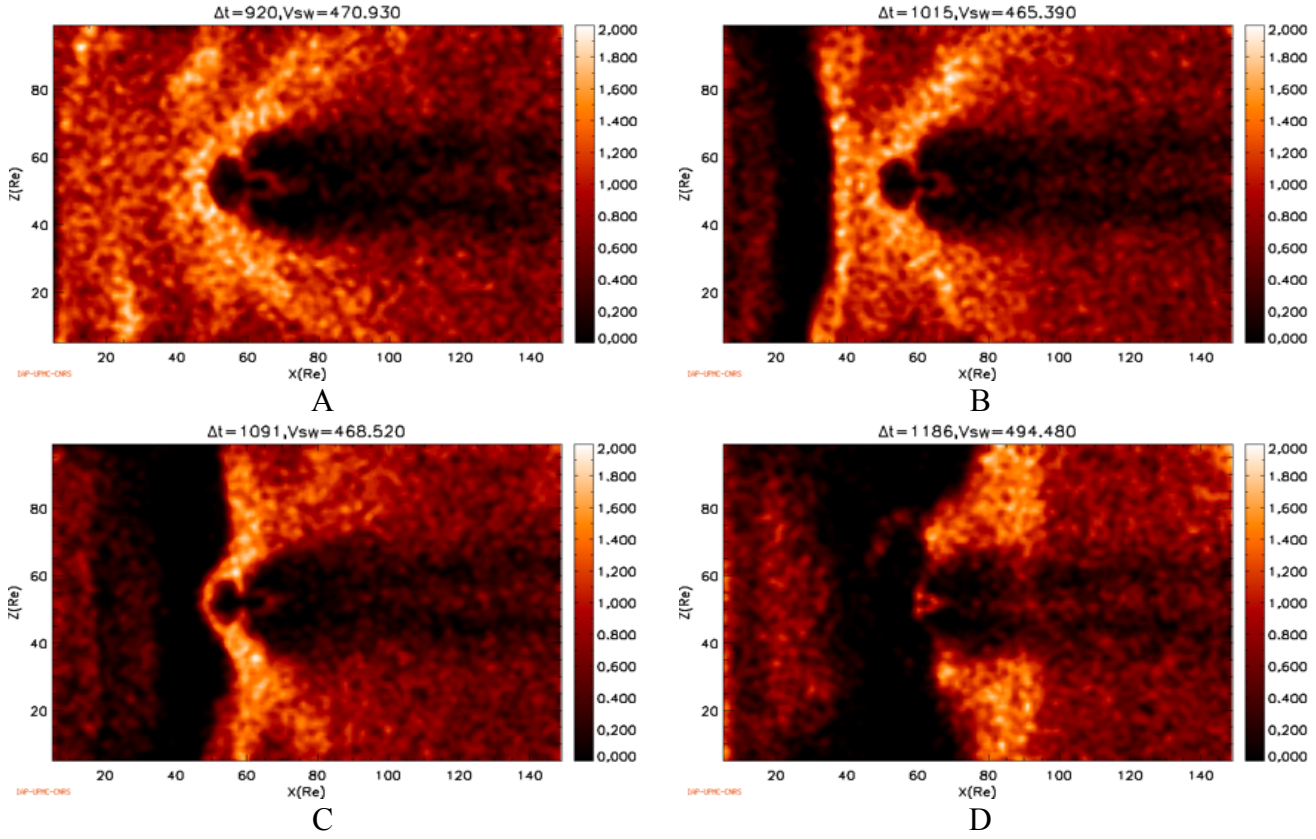

Figure 7.1. Time sequence of the dramatic response of Earth's magnetosphere to a short piece of the Halloween event, Oct., 2003. Plasma density is shown in panels A, B, C and D, taken at 920, 1015, 1091 and 1186 Δt respectively. [1Δt~ 3.368 sec]. Plots are shown in the x-z plane located at y= 52Re.

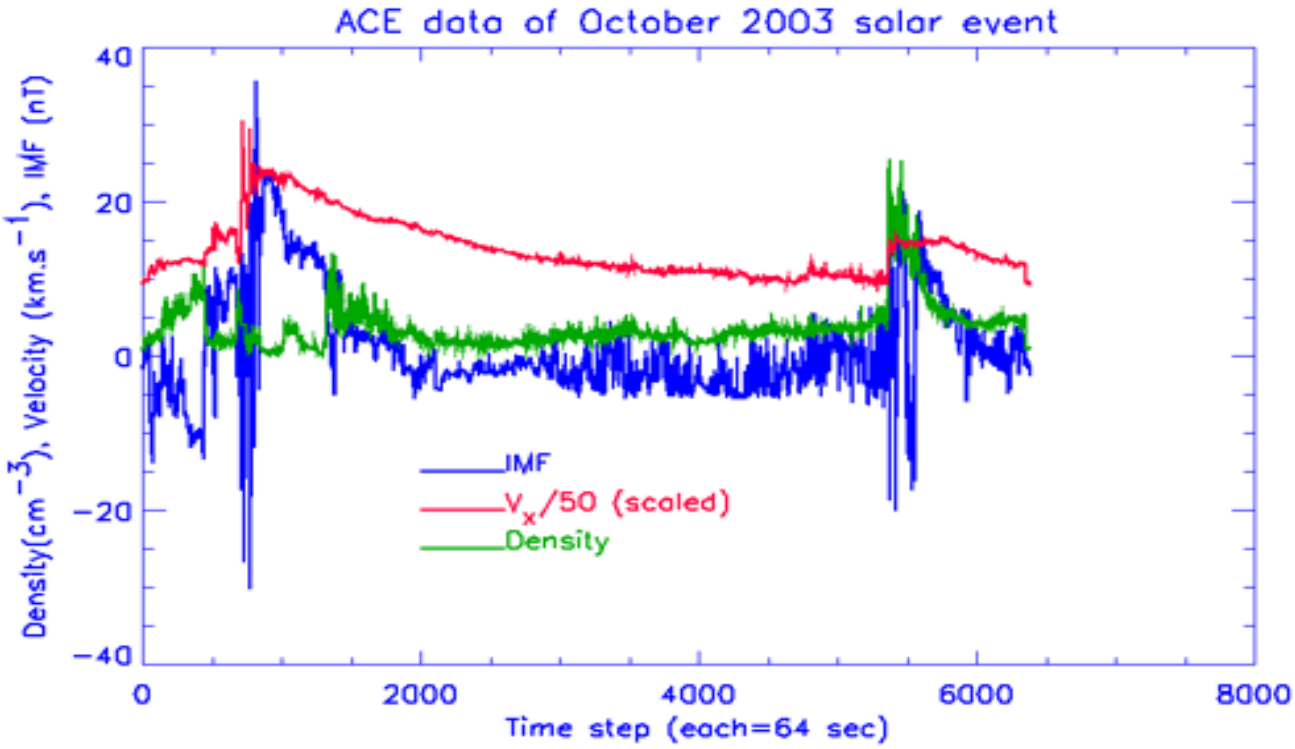

Figure 7.2.a The solar wind parameters of the ACE data during the Halloween event, Oct., 2003

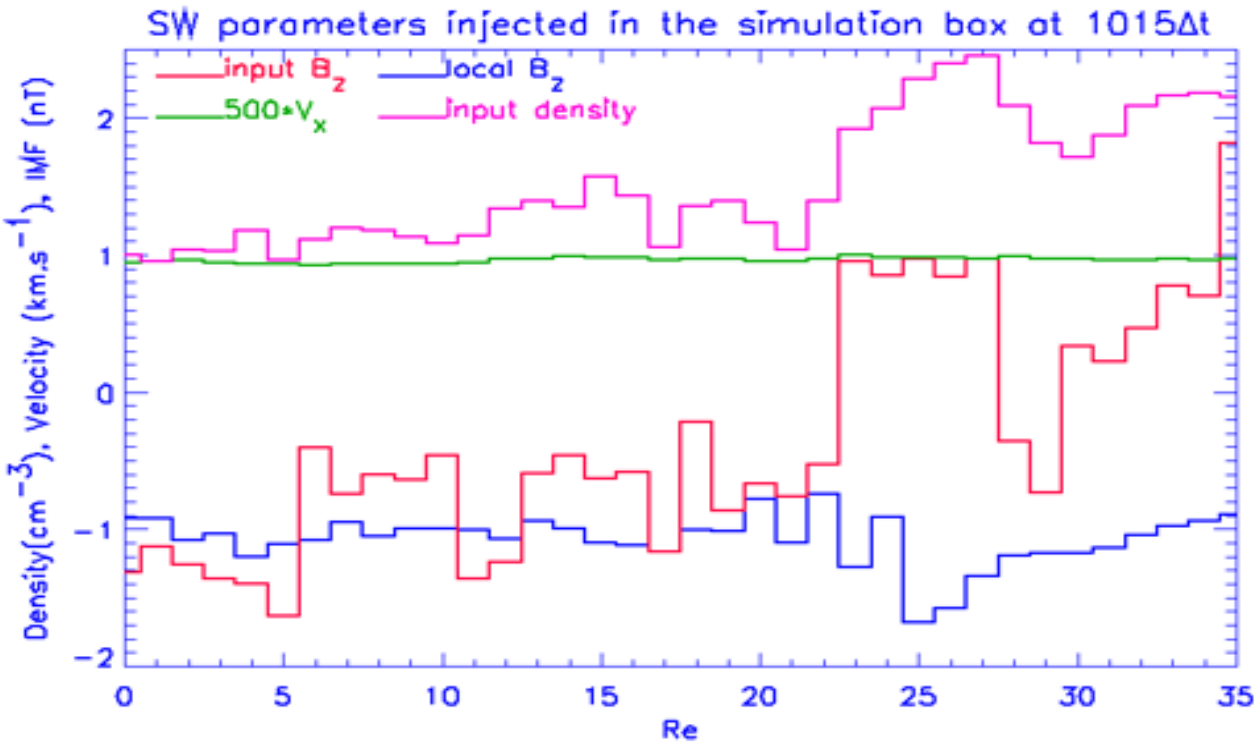

Figure 7.2.b The solar wind input parameters of the ACE data during the Halloween event, Oct., 2003 and the measured IMF at 1015Δt. At that time, the profile of these values is taken within the box along the expected position of gap from 0 to 35Re along x-direction.

7.3 Simulation of the magnetosphere response in terms of field's lines topology to the abrupt solar event observed during the solar activity on October, 2003.

The field's lines topology of the solar activity during Oct. 2003 is presented in figure 7.3 in the noon-midnight planet(x-z plane: at y=52Re). In Figure 7.3(A) taken at 920Δt, the field lines are opened at the dayside. Moreover, those lines at the southern hemisphere and around the magnetopause boundary are bent backward; seemingly undergo erosion process. On the other hand, the field's lines are flared out at the early nightside. Additionally, the fishtail configurations (a result already obtained in our synthetic case in chapter 5, and that seems to be a constant in the Earth's magnetosphere response to strong disturbances when a southward IMF is included) appears clearly starting from x=100 Re and beyond. Also, at the nightside the x-point is observed at around 80 Re.

Figure 7.3(B) taken at 1015Δt, shows the field's topology that corresponds to the plasma distribution described in figure 7.1(B). The field's lines shown along x-direction at the supposed position of the gap (x=0-35Re) are pointing southward. Therefore, these lines are real field's lines topology, a conclusion of the IMF representation that Figure 7.2 can provide. Apparently, the opened field's lines at the magnetopause in the southern hemisphere are again subject to erosions same case as described in Figure 7.3(A). On the other hand, at the nightside the field's lines are flared out with the fishtail configuration of the field's lines is observed starting from x=95Re and on. Also an x-point appears clearly at 77 Re, followed by subsequent connected or bent field's lines along the neutral line all the way out to the end of the simulation box.

In Figure 7.3(C) taken at 1091Δt, the southward IMF field's line advances toward the magnetopause position and is seen concaved sunward at x-44Re, much like the plasma distribution shown in Figure 7.1(C)); further discussion of this figure will be presented in section 7.5. In addition, at the magnetopause a signature of reconnection with the IMF field lines is observed, namely along

z=46Re and 55Re at x=50Re. Moreover, at the nightside of the field's configurations, the field's lines are largely flared out In addition; they are subject to reconnection to the IMF at both hemispheres. An x-point is clearly observed at x=77Re, followed again like in Figure 7.3(B) by subsequent connected or bent field's lines along the neutral line all the way out to the end of the simulation box.

Figure 7.3(D) taken at 1186Δt, the density profile at the first 40Re along the x-direction indicates that the plasma density goes down to an average value of 0.18 (separate analysis of the IMF profile at the said range yields the average IMF value of ~0.18 nT). For this reason, the field's configuration appears stormy in shape. As a result, specifically two vortices appear at two locations centered at the points (x,z)=(30,24) and (30,52)Re. Additionally, the field's lines at the magnetopause are open and reconnect to the advanced southward IMF. Further more, the northern and the southern planet poles seem like a hub through which the field's lines are seen either entering or leaving. While at the nightside, the field's lines are slightly flared out and seemingly more drifted toward the south.

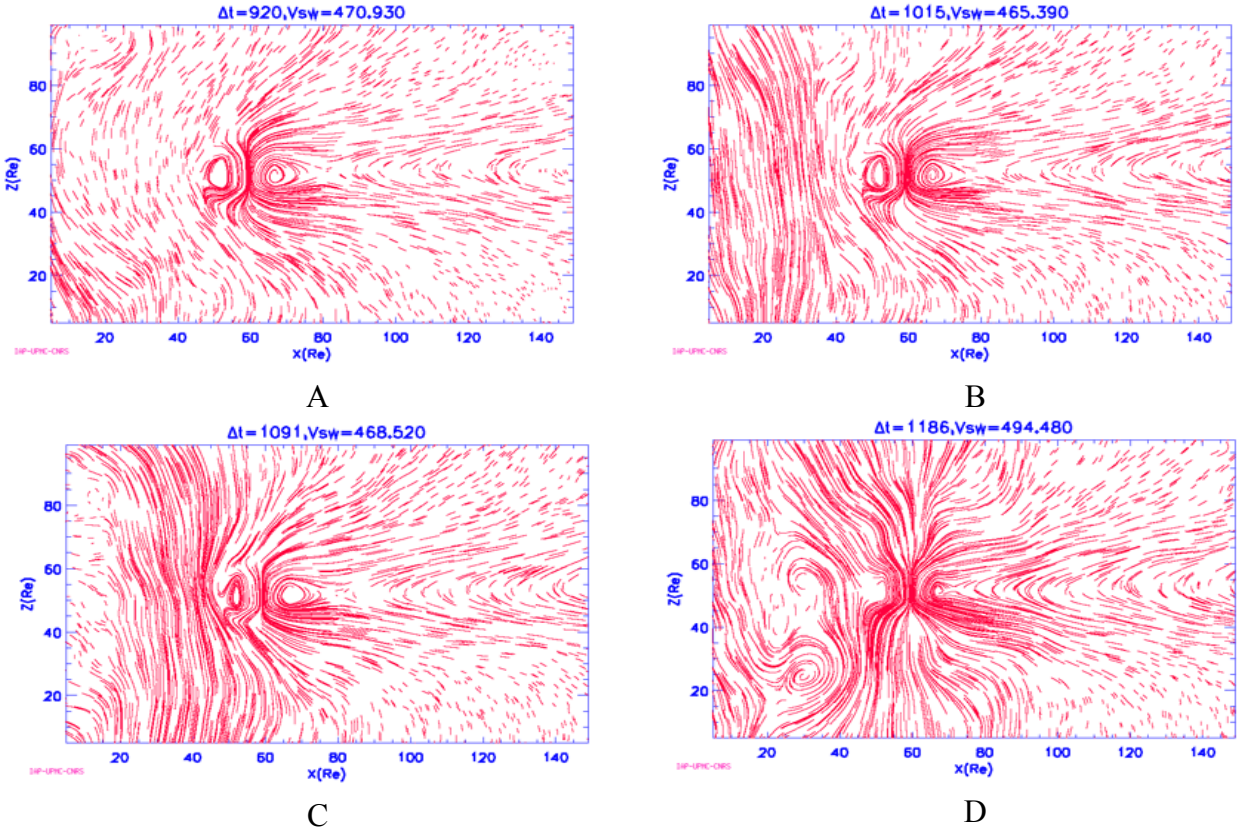

Figure 7.3 Time sequence of the dramatic response of Earth's magnetosphere to Halloween event, Oct., 2003. Field's lines topologies are shown in panels A, B, C and D, taken at 920, 1015, 1091 and 1186 Δt respectively. Provide real time period that correspond to these code step times. Plots are shown in the x-z plane located at y= 52Re.

7.4 Future works and plans

ACE data will be a good source for implementing our theoretical model, after enhancing its parameters in terms of number of particles per cell and the grid size. This is possible as shown by recent work by Cai et al. (2006) who improved the statistics of the PIC code using a higher density of particles per cell and a better resolution for the field description (0.5Re scale compared to 1 Re in our work). However, this would require to access fast and parallel computer with few terabyte storage capacity. The learned lesson from the study of the Halloween events is that: during the erupt of a solar activity a problem of data collections might be raised, and is then attributed to the impact of the erupted activity on the satellites, probes and other space instrumentations themselves. Therefore, an enhanced tested-code will be of a great asset for future studies; this is the pillar of my future potential research activity.

7.5 Conclusion and Remarks

In this chapter the PIC code has been applied to study real solar wind data. In chapter 5 and 6, the IMF input value was set as a steady flow all over the simulation box equal to -0.2 (south) and 0.2 (north), respectively. On contrary the implied IMF value during the application of ACE data is much higher. One of the important conclusions of this chapter is that a gap can also be generated when strong IMF is abruptly applied. The strong gradient in the applied field immediately induces an electric field that sweeps out the plasma from the region where it is applied. By contrast, we remind that in chapter 3, a gap was generated as a drop in the solar wind speed flow. Another process that may also cause a depression in the solar wind is the formation of a hot flow anomaly that allowed the magnetopause to expand sunward by as much as 5 Re from its nominal position (Sibeck et al., 1999). We may thus conclude that by considering our simple air pocket model, we raised a general problem of interest in the study of the Earth's magnetosphere and its response to the solar activity. This class of disturbances covers a wide range of processes that should be studied more in depth in the future

Chapter Eight

Summary and Discussion

8.1 Results

The thesis title is “Study of the Interaction of the Solar Wind with the Earth Magnetosphere: Theoretical Model and application on the Halloween Event in Oct. 2003”. The thesis is based on a fully 3D electromagnetic relativistic particle-in-cell code that represents the skeleton of the theoretical model that we propose to study the response of the Earth’s magnetosphere to a specific class of disturbance in the impinging solar wind. Concretely, we focus on disturbances that may induce a gap (depression) in the plasma flow in front of the dayside of the magnetosphere, either by a sharp gradient in the density, velocity, or IMF profiles.

In practice, the study is carried out with the basic controlling elements, namely the ram pressure and the IMF of the solar wind on one side, and the Earth’s dipole magnetic field on the other. For example, low, moderate and strong bulk velocities of the solar wind are used as inputs to read the reaction of the Earth’s magnetosphere. Consequently, an artificial disturbance in the solar wind dynamic flow is then created to simulate its variability. As a result a gap is created in the solar wind flow (depression); later this gap is called ‘air pocket effect’ based on a statistical analysis of the behavior of plasma blobs inside it. Moreover, to gradually study the time evolution of the response of the Earth’s magnetosphere to the depression in the solar wind, IMF is set first to zero, and then was separately included as a steady flow in both south and north directions. This strategy enabled us to build up a diagnostic tool, by which later the model was applied to the Halloween event in October 2003.

The conclusion of each chapter presented in this thesis is summarized in the following sub-sections. Comparison to existing studies and/or observations is included when there is a need. Generally speaking, this thesis work is related to diverse topics, such as the Sun-Earth connection, Space Weather, Magnetospheric Physics and Space Plasma Physics.

8.1.1 Code description [chapter 2]

The code initially proposed by Buneman et al (1992, 1993, and 1995) is described in chapter 2 in terms of particles updates, magnetic and electric fields updates. This code has been extensively used in the past years (Nishikawa, 1997, 1998; Nishikawa and Ohtani, 2002;Wodnicka, 2001; Cai et al., 2006; Baraka and Ben-Jaffel, 2007). It may be worth to remark that the way the PIC code was built is to have the fields evaluated over the grid nodes, while particles can have any position within the box. Kinetic effects of particles are then included, though fields are averaged over a cell's scale (1 Re here) and the particles mass ratio, mi/me, is large but far from its real value. It follows that our PIC code is well designed for the study of the macro-structure of a magnetosphere but requires a denser grid and a better particle statistics for smaller scales (Cai et al., 2006).

8.1.2 Code Validation on test study cases [chapter 3]

The code has been tested successfully to recover the macrostructure of the Earth magnetosphere. In a small simulation box and small number of electrons-ions pairs, three different categories of solar wind bulk velocities were successfully tested. The code was also used to simulate disturbances in the incident dynamic pressure of the solar wind. As a result a gap was generated (depression in the solar wind dynamic pressure). The 3D representation of plasmas density distributions and the fields' topology offer a comprehensive image about the different regions of the magnetospheric

macrostructure. As an example, the magnetopause, the magnetotail, the northern and southern cusps, the magnetospheric cavity were all recovered.

8.1.3 Air Pocket Effect on the Dayside MP when B_z=0 [chapter 4]

Our simulation for the depression of the solar wind pressure produced a planar volume of depletion in the plasma (figure 4.1), with sharp edges perpendicular to the x-direction and propagating Earthward. In the real solar wind, an analogous depression in the IMF strength has been observed just upstream of the bow shock by three satellites AMPTE UKS, IRM and ISEE1 (Chisham et al 2000). In our PIC model, the solar wind pressure perturbation (gap) as it approaches the magnetosheath region, is decelerated with the generation of instabilities, evidenced both in the plasma distribution and in the field lines topology (Figures 4(1,2)). Our results seem consistent with the general idea for the occurrence of instabilities and turbulence in the magnetosheath as observed by Cluster (Lucek et al., 2005). In response to the depression of the solar wind pressure, the magnetopause expands sunward along the x-direction from 10 Re out to 15 Re with an average speed of 0.12 (equivalent to 240km.s^{-1}) and then recovers its original size with an average speed of 0.133 (equivalent to ~266 km/s). We also note that if the perturbation is spatially confined, only a limited section of the magnetopause should expand. It is worth to note that in the absence of the IMF, and during its expansion phase, the magnetopause structure breaks up at 15.5Re. Similarly, observations by Interball-1 and Magion-4 of a hot flow anomaly (HFA) with a strong depression revealed that the magnetopause expanded sunward by as much as 5 Re from its nominal position (Sibeck et al., 1999). Magnetic field measurements in solar wind and outer magnetosphere onboard the INTERBALL-1 was discussed by Klimov et al., (2002). According to Sibeck et al. (1999) the HFA was born after an IMF tangential discontinuity interacted with the Earth's bow shock. The results of our simulation are remarkably consistent with the Interball-1 observations. Thus hot flow anomalies are a class of discontinuities that can be handled by

our simulation model. These results open new horizons for future work using this code to study the propagation of solar wind discontinuities and their impact on the magnetosheath/magnetopause system. In the past, these studies were usually conducted using MHD modeling (Samsonov et al, 2006, and references within). In the future it would be useful to compare a PIC code simulation of the interaction of solar wind discontinuities of the kind considered here with the Earth's magnetosphere to previous MHD calculations. During our study of time propagation of the depressed ram pressure of the solar wind, we noticed some penetration of solar wind plasma into the magnetospheric cavity. Despite the fact that our code was run with a relatively large spatial scale (1Re) for the fields, many other dynamic processes were observed around the magnetopause boundary. These processes were the candidate processes responsible for the penetration of solar wind particles into the inner Earth magnetosphere, based on CLUSTER observations presented in the work of Phan et al., (2005). As an example, our simulation showed that one can track up to two x-points in the magnetotail neutral sheet as indicated by two arrows in Figure 4.4 (C). These results are remarkably consistent with Cluster report of multiple x-line structure in the Earth's magnetotail current sheet (Eastwood et al., 2005). Another intriguing result in chapter 4, the magnetopause response to the abrupt change in the solar wind dynamic pressure shows a nearly-fast linear expansion. Since the gap extension is large enough, the induced non-restricted force blows off the magnetopause structure and the magnetopause boundary breaks up, leaving the magnetopause with an open boundary. FTE study of CLUSTER space craft discussed discontinuities corresponding to open magnetopause (Robert, P. et al 2006). Within the generated disturbance in the solar wind flow during B_z=0, it was noticed that some plasma blobs reversed directions. Details of this reversal and the related analysis are discussed in section 4.6 and figure 4.8 in chapter 4.

8.1.4 Air Pocket Effect on the Dayside MP when B_z<0 [chapter 5]

Again the simulation of the depression of the solar wind pressure produced a planar volume of depletion in the plasma (figure 5.1), with sharp edges perpendicular to the x-direction propagating Earthward. In figure 5.4(C) we noticed that magnetic erosion takes place in which field lines are bent tailward rather than squeezed; as a result, they feed the tail with particles (confirmed by a movie of the field lines that spans 250 frames, each per Δt). This result is consistent with investigation made during the magnetopause crossings by the ISEE 1 and 2 spacecrafts, where the magnetopause erosion was observed during a southward IMF. It is shown that the magnetopause erosion may be explained by a depression of the magnetic field intensity in the dayside magnetosphere caused by the penetration of the magnetosheath magnetic field (component perpendicular to the reconnection line) into the magnetosphere, Pudovkin et al (1997). On contrary with the absence of IMF (discussed in chapter 4), it was noticed that during the southward IMF the magnetopause expansion/recovery phase as it responds to the depression of the solar wind dynamic pressure was nonlinear. Existence of B_z makes the expansion phase slower. Indeed, the IMF confines the plasma so that the magnetopause never breaks up. We believe that the fast recovery of the magnetopause is due to a magnetic force directed tailward (the slingshot effect) that adds to the magnetic force of the dipole when the dynamic pressure of the solar wind overpasses the magnetopause boundary. The X-points are observed located more closer to the planet position as the tail side boundary are seen reduced. Earth's bow shock was successfully simulated and was shown for both plasmas and fields.

8.1.5 Air pocket Effect on the Dayside MP when B_z>0[chapter 6]

We notices that accumulation of plasma density is seen maximized around the magnetopause and along the upstream edge of the generated gap as shown in figure 6.1(A). In a recent study, Lin and Wang (2006) showed that, under a purely northward interplanetary magnetic field (IMF), magnetic reconnection in both northern and southern hemispheres leads to a continued formation of newly closed field lines on the dayside. Subsequently, the low latitude boundary layer (LLBL) form by capture of the magnetosheath ions on the original magnetosheath field lines, as the newly closed field lines shorten. The formation of the LLBL is associated with the tailward spreading of the transmitted ions along the magnetopause as the newly closed flux tubes convect tailward. Same confirmation for the formation of LLBL under B_z>0, is discussed in the work of Lavraud et al., (2006). Our Figure 6.1(A, and B) seems consistent with these findings. Moreover Chen et al., (1993) have shown through the analysis of the data obtained by observation by ISEE 1 and 2 spacecraft that the flare out at the night side ceased at 15 Re, and the fields lines are larger at the subsolar magnetopause when northern IMF is applied, a result that our work seem consistent as in Figure 6.1(D) and 6.4(D). The simulated depression of the solar wind for B_z>0 has a comparable size for the generated gap as for both B_z<0 and B_z=0. Inside the gap, we noticed that the density of clouds is much larger this time. For the magnetopause expansion rate, the MP expands along x-direction with a speed equal ~ 0.18 (velocity equivalent to 360 km.s^{-1}) and recovers at a speed rate equal ~0.16 (~320 km. s^{-1}). On the other hand, the rate of the MP expansion along y-direction is 0.177 (~354 km.s^{-1}) and the corresponding recovery speed is ~0.31 (~ 620 km.s^{-1}). Moreover, the expansion rate as seen in the z-direction shows a speed around 0.12 (~ 240 km. s^{-1}), whilst the corresponding recovery speed has the value ~0.45 (~900 km.s^{-1}). In conclusion, these statistics show that the recovery phase always takes place much faster that the expansion phase. In addition, the closer is the boundary to disturbance effect the faster it responds to the applied effect.

Moreover, denser plasma populates the cavity at the magnetotail which results in tail shift to south (figure 6.1(C)). This tail shift is in turn a sign of reconnections in that region. Particles entry in the dawn direction shown in figure 6.3(C) is believed to be caused by the reconnection at both southern and northern cusps. Orientation of the cusps is slightly affected by the depression in the solar wind flow and most often is nightward oriented.

The size of the MP in the y-direction is approximately ~13.3Re just before the onset of the magnetopause expansion along that direction. As the generated gap moves Earthward, the drop off in the solar wind dynamic pressure causes the magnetopause subsolar point to move sunward. The drop off in the solar dynamic pressure is not yet felt at the dawn-dusk direction. This makes the field lines elongate along x for 100Δt before the gap advances enough to impact the expansion in the dawn-dusk direction. During this period, the MP shrank from 13.3 down to 9.2 Re, before it started expanding. The situation resembles a U-shaped rubber band that pulled from the concave part while kept fixed at both ends for some time. Figure 6.8 shows this model representation, namely the elastic field lines model.

8.1.6 Code Application on October 2003 Event [chapter 7].

The application of our PIC EM code to simulate the ACE data revealed a new class of disturbances that are worthy to be considered in future work carefully. In chapters, 4, 5, and 6 an artificial disturbance was generated by an abrupt drop in the bulk velocity of the incident solar wind dynamic pressure, as a result gap (depression) in the solar wind was generated; a term we called it 'Air Pocket Effect'. When the code was first used to produce the macrostructure of the Earth's magnetosphere, we purposefully set IMF=-0.2, so that when the ACE data is applied, a high jump in the IMF value is applied to the system (see figure 7.2). Consequently, a surprisingly new air pocket

class was generated i.e. Figure 7.1(B). The air pocket so far produced by our simulation could be the equivalent of a flow anomaly (HFA) as reported by Sibeck et al., 1999.

To the best of our knowledge this is the first study to synthesize a macrostructure of the Earth magnetosphere, as it responds to a strong solar activity. It is only a first step, in more comprehensive future research in the field using our PIC EM relativistic code. This work sheds light to the importance of the development of the PIC codes to simulate natural processes.

8.2 Future work and plans.

a. Short term plans

b. Medium term plans

c. Long term plans

a. To go on further case studies using the code and target specific regions in the Earth's magnetosphere. In other words, the code output can be used to zoom-in the dawn, dusk or subsolar points of the magnetopause to track particle's entries and any potential reconnections. Also, as some of our results showed that the cusps orientation, thickness and position are affected by the depression in the bulk velocity of the solar wind; both regions are of interest to study. Finally, my thesis focused mainly on the dayside magnetosphere, but the nightside is a rich region for the geomagnetic activity that can be soon targeted for study.

b. In the medium term plans, I am thinking to be affiliated with an observation group to closely work with them to analyze data and to better understand some dynamical processes that take place in nature by re-producing them to trace their cause/effect and the other related physics. For that purpose, more parameters can be included in the code, such as the ionosphere, corotation currents, and the planet tilt.

c. In the long term plans, to establish a space research project in Gaza-Palestine and link it to international institutions to promote astronomy in my country, in a program I mean to call 'if peace can't be found temporary on Earth find it in the space". In fact, we have already started the establishing of a geomagnetic station by the help of the French Government. Dr

Ben Jaffel from the French side was the principal investigator of the project called “SWEP”, which stands for Space Weather in Palestine. For some reasons related to the current situation, the project is frozen. I am longing to revitalize it again. I hope things will be better and in the near future we could be able to make it happen.

Bibliography

Akasofu, S. I. (1980), The solar wind –magnetosphere energy coupling and magnetospheric disturbances, *Planetary Space Science, 28*, 495-509.

Aubrey, M. P., C. T. Russell and M. G. Kivelson (1970), Inward motion of the magnetopause before a substorm, *J. Geophys. Res., 75*, 1673

Balogh, A., Carr, C. M., Acuna, M. H., et al (2001), The Cluster magnetic field investigation: Overview of in-flight performance and initial results, *Annal. Geophysicae, 19*, 1207

Baraka, S., and L. Ben Jaffel (2007), Sensitivity of The Earth's Magnetosphere To solar wind Activity:3D Macroparticle Model, J. *Geophys. Res., accepted*

Bauer, T. M., Dunlop, M. W., Sonnerup, B. U. O¨ ., Sckopke, N.,Fazakerley, A. N., and Khrabrov, A. V.(2000): Dual spacecraft determinations of magnetopause motion, *Geophys. Res. Lett., 27,* 1835

Baumjohann, W., G. Paschmann, and C. A. Cattel,(1989), Average plasma properties in the central plasma sheet. *J. Geophys. Res.94*, p6597

Birn, J. (2005), Three dimensional magnetotail equilibria with prescribed boundary shapes, *J. Geophys. Res., 110,* A07203, doi: 10.1029/2004JA010869

Boris, J. P., Relativistic plasma simulation optimization of a hybrid code, Proc. Fourth Conf. Num. Sim. Plasmas, Naval Res. Lab., Washington, 3-67, 2-3 November (1970)

Boudouridis, A., E. Zesta, L. R. Lyons, P. C. Anderson, and D. Lummerzheim (2003), Effect of solar wind pressure pulses on the size and strength of the auroral oval, *J. Geophys. Res. , 108 (A4)*, 8012, doi : 10.1029/2002JA009373.

Buneman, O. (1993), TRISTAN, *in Computer Space Plasma Physics: Simulation Techniques and*

Software, Edited by H. Matsumo and Y. Omura, pp, pp. 67-84, Terra Sci. Tokyo

Buneman, O., K.-I. Nishikawa, and T. Neubert (1995), Solar wind-magnetosphere interaction as simulated by a 3D EM particle code, in space Plasmas: Coupling Between Small and Medium Scale Processis, *Geophys. Monogr. Ser. , Vol. 86,* edited by M. Ashour-Abdullah, T. Chang, and P. Duenburg, pp. 347-352, AGU, Washington, D.C.

Burch, J. L. (2005), Magnetospheric imaging: Promise to reality, *Reviews of geophysics, 43*, RG3001, doi: 10.1029/2004RG000160

Cai, D., X. Y. Yan, K.-I. Nishikawa, and B. Lambege (2006), Particle entry into inner magnetosphere during duskward IMF B_y: Global three-dimensional electromagnetic full particle simulations, *Geophys. Res. Lett., 33,* L121001, doi:10.1029/2005GL023520.

Cai, Dongsheng, Yaoting Li, Ken –Itchi Nishikawa, Chiji Xiao, Xiaoyang Yan, and Zuying Pu (2003), Parallel 3-D Electromagnetic Particle Code Using High Performance FORTRAN:Parallel TRISTAN, *Space Plasma Simulation. Edited by J. Büchner, C. Dum, and M. Scholer., Lecture Notes in Physics, vol. 615*, pp.25-53

Cahill, L. J., Jr., and P. G. Amazeen (1963), The boundary of the geomagnetic field, *J. Geophys. Res. , 68,* 1835.

Cahill, L. J. and V. L. Patel (1967), The boundary of the geomagnetic field, August to November 1961, *Planet. and Space Sci., 15*, 997-1033.

Chapman, S. and V. C. A. Ferraro (1930), A new theory of magnetic storms, *Nature*,126-129

Chapman, S. and V. C. A. Ferraro (1931), A new theory of magnetic storms, *Terr. Magn. Atmosph. Elec.36,*171-186

Chisham, G., S. J. Schwartz, D. Burgess, S. D. Bale, M. W. Dunlop and C. T. Russell (2000),

Multisatellite observations of large magnetic depressions in the solar wind, *J. Geophys. Res.,105,* Issue A2, p. 2325-2336

Chen, S-H., M. G. Kivelson, J. T. Gosling, R. J. Walker, A. J. Lazarous (1993), Anomalous aspects of magnetosheath flow and of the shape and oscillations of the magnetopause during an interval of strongly northward interplanetary magnetic field, *J. Geophys. Res, 98,*A4, pp. 5727-5742

Cowley, S. W. H. (1984), Magnetic reconnection in Space and Laboratory Plasmas, (ed. Hones, E. W.) American Geophysical Union, 375-378.

Cummings, W. D. and P. J. Coleman (1968), Magnetic fields in the magnetopause and vicinity at the synchronous altitude, *J. Geophys. Res. , 73*, 5699.

Eastman, T. E., and E. W. Hones Jr. (1979), Characteristic of the magnetospheric boundary layer and magnetopause layer as observed by IMP 6, *J. Geophys. Res. , 84*, 2019-2028.

Eastwood, J. P., D. G. Sibeck, J. A. Slavin, M. L. Goldstein, B. Lavraud, M. Sitnov, S. Imber, A. Balogh, E. A. Lucek, and I. Dandouras, (2005), Observation of multiple X-line structure in the Earth's magnetotail current sheet: A Cluster case study, *Geophys. Res. Lett., 32,* L11105, doi:10.1029/2005GL022509

Escoubet, C. P., R. Schmidt (2000), Cluster II: Plasma Measurements in Three Dimensions, Adv. In Space Res. 25,7-8,p. 1305-1314

Fairfield, D. H. (1971), Average and unusual locations of the Earth's magnetopause and bow shock, JGR, 76, 6700.

Fuselier, S. A., B. J. Anderson, and T. G. Onsager (1995), Particle signature of magnetic topology at the magnetopause: AMPTE/CCE observations, *J. Geophys. Res.*, 100, 11,805.

Fuselier, S. A., B. J. Anderson, and T. G. Onsager (1997), Electron and ion signature of field line topology at the low-shear magnetopause, *J. Geophys. Res.* , 102, 4847-4863.

Fuselier, S. A., D. M. Llumpar, and E. G. Shelley (1991), Ion rfleciton and transmission during reconnection at eh Earth's subsolar magnetopause, *Geophys. Res. Lett., 18*, 139.

Gonzales, W. D., J. A. Joselyn, Y. Kamide, H. W. Kroehl, G. Rostoker, B. T. Tsurutani, and V. M. Vasyliunas(1994), What is a geomagnetic storm?, *J. Geophys. Res., 99*, 5771-5792

Gopalswamy, N., L. Barbieri, E. W. Cliver, G. Lu, S. P. Plunkett, and R. M. Skoug (2005), Introduction to violent Sun-Earth connection events of the October-November 2003, *J. Geophys. Res. , 110,*A09S00, doi:10.1029/2005JA011268

Gosling, J. T., M. F. Thomsen, , S. J. Bame, R. C. Elphic, and C. T. Russell (1991), Observations of reconnection of interplanetary and lobe magnetic field lines at eh high-latitude magnetopause. *J. Geophys. Res. , 96, 14, 097-14*, 106.

Gosling, J. T.(1996), Corotating and Transient Solar Wind Flows in Three Dimensions., *Ann. Rev. of Astronomy and Astrophysics, 34*, 1996, pp. 35-74

Gosling, J. T., D. J. McComas, J. L. Phillips, and S. J. Bame(1991), Geomagnetic activity associated with Earth passage of interplanetary shock disturbances and coronal mass ejections, *J. Geophys. Res., 96*, 7831-7839

Guzdar, P. N., X. Shao, C. C. Goodrich, K. Papadopoulos, M. J. Wiltberger, and J. G. Lyon (2001), Three-dimensional MHD simulations of the steady state magnetosphere with northward interplanetary magnetic field, *J. Geophys. Res., 106,* Issue A1, pp. 275-288

Haaland, S. E. , B. U. ¨O. Sonnerup, M.W. Dunlop, A. Balogh, E. Georgescu, H. Hasegawa, B. Klecker, G. Paschmann, P. Puhl-Quinn, H. R`eme6, H. Vaith, and A. Vaivads(2004), Four-spacecraft determination of magnetopause orientation, motion and thickness: comparison with results from single-spacecraft methods, *Annales Geophysicae, 22*, p 1347–1365

Hall, D. S., C. P. Chaloner, D. A. Bryant, D. A. Lepine, and V. P. Tritakis (1991), Electrons in the

boundary layers near the dayside magnetopause, *J. Geophys. Res. , 96*, 7869-7891.

Hasegawa H., M. Fujimoto, K. Takagi, Y. Saito, T. Mukai, and H. Rème (2006), Single-spacecraft detection of rolled-up Kelvin-Helmholtz vortices at the flank magnetopause, *J. Geophys. Res., 111*, Issue A9, doi:10.1029/2006JA011728

Iyemori, T., and D. R. K. Rao (1996), Decay of the Dst field of geomagnetic disturbances after substorm onset and its implication to storm-substorm relation, *Ann. Geophysicae, 14*, 608-618.

Kaufmann, R. L., and A. Konradi (1969), Explorer 12 magnetopause observations: large-scale nonuniform motion, *J. Geophys. Res. , 74*, 3609.

Kessel, R. L., S. H. Chen, J. L. Green, S. F. Fung, S. A. Boardsend, L. C. Tan, T. E. Eastman, J. D. Craven, and L. A. Frank (1996), Evidence of high-latitude reconnection during northward IMF: Hawkeye observations. *Geophys. Res. Lett. , 23*, 583-586.

Kivelson, M. G., and C. T. Russell, (1997), *Introduction to Space Science*, chapt. 6, 9, and10, Cambridge University Press, USA.

Klimov S.I.; Grushin V.A.; Lissakov Y.V.; Nozdrachev M.N.; Petrukovich A.A.; Grachev E.A.; Grigoryan O.R.; Lysakov D.S.; Schwingenschuh K.; Auster H.U.; Fornacon K.-H.; Rustenbach J.; Korepanov V.E.; Juchniewicz J.; Afanasjev Y.V.; Kudela K (2002). Interball-1 and MIR orbital station coordinated magnetic field and energetic particles measurements,*Adv. S. Res.,30*, Number 7, 2002, pp. 1847-1853(7)

Lavraud, B.; Thomsen, M. F.; Lefebvre, B.; Schwartz, S. J.; Seki, K.; Phan, T. D.; Wang, Y. L.; Lin, Y., and X. Y. Wang (2006), Formation of dayside low-latitude boundary layer under northward

Le, G., C. T. Russell, J. T. Gosling, and M. F. Thomsen (1996), ISEE observations of low –latitude boundary layer for northward interplanetary magnetic field: implications for cusp reconnection, *J. Geophys. Res. , 101*, 27,239-27,249.

Lee, D. -Y., and L. R. Lyons (2004), Geosynchronous magnetic field response to solar wind dynamic pressure pulse. *J. Geophys. Res. , 109*, A04201, doi: 1029/2003JA010076.

Lezniak, T. W., and J. R. Winckler (1968), Structure of the magnetopause at 6.6 Re in terms of 50 to 150 –kev electrons, *J. Geophys. Res. , 73*, 5733.

Lindman, E. L. (1975), Free-space boundary conditions for the time dependent wave equation, *J. Comput. Phys., 18*, 66-78

Lucek, E. A., D. Constantinescu, M. L. Goldstein, J. Pickett, J. L. Pinçon, F. Sahraoui, et al (2005), The Magnetosheath, *Space Sc. Rev.,118,* Issue 1-4, pp. 95-152

McPherron, R. L.(1987), The role of substorms in the generation of magnetic storms, in Magnetic storms, edited by B. T. Tsurutani, W. D. Gonzales, Y. Kamide, and J. K. Arballo, *AGU Geophys. Monogr. 98*, 131-147.

Nishikawa, K., I. (1997), Particle entry into the magnetosphere with a southward interplanetary magnetic field studied by a three-dimensional electromagnetic particle code, *J. Geophys. Res. A8,* pp 17,631-17,641

Nishikawa, K. I. and S. Ohtani (2000), Evolution of thin current sheet with a southward interplanetary magnetic field studied by a three-dimensional electromagnetic particle code, *J. Geophys. Res., 105,* A6, 13017-13028.

Nishikawa, K. I., Neubert, T., Buneman, O. (1995) solar wind-Magnetosphere Interaction as Simulated by a 3-D EM Particle Code, *Astrophysics and Space Science, 227*, p. 265-276

Nishikawa, K. I. (1997), Particle entry into the magnetosphere with a southward interplanetary magnetic field studied by a three-dimensional electromagnetic particle code, *J. Geophys. Res., A8,* 17,631-17,641.

Nishikawa, K. I. (1998), Particle entry though reconnection grooves in the magnetopause with a

dawnward IMF as simulated by a 3-D EM Particle code, *Geophys. Res. Let. 25,* 10, 1609-1612.

Marklund, G. T., L. G. Blomberg, C.-G. Fälthammar, R. E. Erlandson, and T. A. Potemra (990), Signatures of the high-altitude polar cusp and dayside auroral regions as seen by the Viking electric field experiment, *J. Geophys. Res., 95*, 5767-5780

McPherron, R. L.(1987), The role of substorms in the generation of magnetic storms, in Magnetic storms, edited by B. T. Tsurutani, W. D. Gonzales, Y. Kamide, and J. K. Arballo, *AGU Geophys. Monogr. 98*, 131-147.

Mishin, V. V, (1993), Accelerated motions of the magnetopause as a trigger of the Kelvin-Helmholtz Instability, *J. Geophys. Res., 98,* pp. 21365-21371

Mitchell, D. G., F. Kutchko , D. J. Williams, T. E. Eastman, L. A. Frank, and C. T. Russell (1987), An extended study of the low-latitude boundary layer on the dawn and dusk flank of the magnetosphere, *J. Geophys. Res. , 92,* 7394-7404.

Murr, D. L. (2004), Scarf Award Presentation: Magnetosphere-Ionosphere Coupling Studies of Dayside High-Latitude Transients, *AGU, Fall Meeting 2004, abstract # SM41B-01.*

Ogilvie, K. W., R. J. Fitzenreiter, and J. D. Scudder (1984), Observations of the electron beams in the low-latitude boundary layer. *J. Geophys. Res. , 89*, 10,727-10,732.

Omidi, N. and D. Sibeck (2005), Stability of the Bow shock and Formation of the Hot Flow Anomalies, *AGU, Spring Meeting 2005, abstract #SM22A-01*

Omidi, N. and D. Sibeck (2007), Formation of hot flow anomalies and solitary shocks, *J. Geophys. Res.,112*, A01203, doi:10.1029/2006JA011663

Onsager, T. G., J. D., Scudder, M. Lockwood, and C. T. Russell (2001), Reconnection at the high latitude magnetopause during northward interplanetary magnetic field conditions, J. Geophys. Res. , 106, 25,467-25,488.

Phan, T. D., C. P. Escoubet, L. Rezeau, R. A. Treuman, A. Vaivads, G. Paschmann, S. A. Fuselier, D. Attié , B. Rogers, and B. U. Oe. Sonnerup (2005), Magnetopause Processes, *Space Science Reviews, 118*, pp367-424

Pritchett, P. L.(2005), Externally driven magnetic reconnection in the presence of a normal magnetic field, *J. Geophys. Res.110,*A05209, doi:10.1029/2004ja010948

Pudovkin M. I., S A Zaitseva, B. P. Besser (1997), The magnetopause erosion and the magnetosheath magnetic field penetration,Adav. S. Res., 19, Issue 12, pp. 1909-1912

Reiff, P. H., T. W. Hill, and J. L. Burch (1977), Solar wind plasma injection at the dayside magnetospheric cusp, *J. Geophys. Res., 82*, 479.

Samsonov, A. A.; Z. Němeček,; J. Šafránková (2006), Numerical MHD modeling of propagation of interplanetary shocks through the magnetosheat, J. Geophys. Res, 111, A8 **doi:** 10.1029/2005ja011537

Semenov, V. S. et al. (2002), a simple model of magnetopause erosion as a consequence of pile-up process and bursty reconnection, *International Journal of Geomagnetism and Aeronomy, 3, 2,* 109-116.

Shue, J. –H., Y. Kamide, (2001), Effects of solar wind on auroral electrojets, *Geophys. Res. Lett., 28*, 11, 2181-2184.

Sibeck, D. G.; N. L. Borodkova,; S. J. Schwartz, et al (1999), comprehensive study of the magnetospheric response to the hot flow anomaly, *J. Geophys. Res., 104*, pp. 4577-4594

Sibeck, D. G.(1994), Signatures of flux erosion from the dayside magnetosphere, *J. Geophys. Res.,99*, A5, p. 8513-8529

Siscoe, G. L., and H. E. Petschek (1997), On storm weakening during substorm expansion phase, *Ann. Geophysicae, 15*, 211-216

Skillman, T. L., and M. Sugiura (1971), Magnetopause crossing of the geostationary satellite ATS 5 at 6.6 RE, *J. Geophys. Res. , 76*, 44.

Smith, M. F., M. Lockwood (1996), Earth's magnetospheric cusps, *Reviews of Geophysics, 34,* 2, 233-260.

Song, P., C. T. Russell (1992), Model of the formation of the lsow latitude boundary layer for strongly northward interplanetary magnetic field. *J. Geophys. Res. , 97*, 1411-1420.

Sonnerup, B. U. Ö., G. Paschmann, I. Papamastorakis, N. Sekopke, G. Haerendel, S. J. Bame, J. R. Asbridge, J. T. Gosling, and C. T. Russell (1981), Evidence for magnetic field reconnection at the Earth's magnetopause, *J. Geophys. Res. , 86*, 10,049.

Sonnet, C. P., E. J. Smith, and A. R. Sims (1960), Surveys of the distant magnetic field: Pioneer I and Explorer II, *Space Res. 1*, 921.

Tanaka, T. (1999), Configuration of the magnetosphere-ionosphere convection system under northward IMF conditions with nonzero IMF, *J. Geophys. Res., A7*, pp. 14683-14690.

Tsyganenko, N. A. and D. J. Sibeck (1994), concerning flux erosion from the dayside magnetopause, *J. Geophys. Res. , 99*, 13, 425.

Villasenor, John and Oscar Buneman (1992), Rigorous charge conversation for local electromagnetic field solvers, *Computer Phys. Communications, 69*, issue 2-3, p. 306-316

Watanabe, M., G. J. Sofko, D. A. André, T. Tanaka, and M. R. Hairston (2004), Polar cap bifurcation during steady-state northward interplanetary magnetic field with $|B_\gamma| \sim B_z$, *J. Geophys. Res., 109*, A01215, doi: 10.1029/2003JA009944.

Winglee, R. M., Lewis, W., and Lu, Gang (2005), Mapping of the heavy ion outflows as seen by IMAGE and multifluid global modeling for the 17 April 2002 storm, *J. Geophys. Res., 110,* A12S24, doi: 10.1029/2004JA010909.

Wodnicka, E. B. (2001), Comparing two models of the Earth's magnetosphere, *Adv. Space Res., 28*, issue 12, p. 1727-1732.

Yamauchi, M., H. Nilsson, L. Eliasson, O. Norberg, M. Boehm, J. H. Clemmons, R. P. Lepping, L. Blomberg, S.-I. Ohtani, T. Yamamoto, T. Mukai, T. Terasawa, and S. Kokubun (1996), Dynamic response of the cusp morphology to the solar wind: A case study during passage of the solar wind plasma cloud on February 21, 1994, *J. Geophys. Res., 101,* 24675-24687

Zesta, E., H. J. Singer, D. Lummerzheim, C. Russell, L. Lyons, and M. J. Brittnacher (2000),The effect of the January 10, 1997 pressure pulse on the magnetosphere-ionosphere current system, *Geophysical Monograp*